Optical parametric devices in periodically poled $LiTaO_3$

MARTIN LEVENIUS

KTH Engineering Sciences

Doctoral Thesis
Department of Applied Physics
KTH – Royal Institute of Technology
Stockholm, Sweden 2013

Optical parametric devices in periodically poled $LiTaO_3$

Quantum Electronics and Quantum Optics
Department of Applied Physics
KTH – Royal Institute of Technology
106 91 Stockholm
Sweden

ISBN 978-91-7501-947-5
TRITA-FYS 2013:65
ISSN 0280-316X
ISRN KTH/FYS/--13:65—SE

Akademisk avhandling som med tillstånd av Kungliga Tekniska Högskolan framläggs till offentlig granskning för avläggande av teknologie doktorsexamen fredagen den 20 december 2013 kl. 10.00 i sal FA31, Albanova, Roslagstullsbacken 21, KTH, Stockholm. Avhandlingen kommer att försvaras på engelska.

Cover picture: Multi-beam parametric generation in the visible supported by 2D quasi-phase matching. Each green beam corresponds to a sum frequency generation process (SFG) driven by the pump beam and a signal beam involved in a simultaneous process of coupled optical parametric generation (OPG). Each blue beam corresponds to a second harmonic generation process driven by the pump beam, which also drives the OPG and the SFG processes.

Printed by Universitetsservice US AB, Stockholm 2013

Martin Levenius
Optical parametric devices in periodically poled $LiTaO_3$
Department of Applied Physics, KTH – Royal Institute of Technology
106 91 Stockholm, Sweden

ISBN 978-91-7501-947-5, TRITA-FYS 2013:65, ISSN 0280-316X, ISRN KTH/FYS/--13:65—SE

Abstract

Optical parametric frequency conversion based on quasi phase matching (QPM) in nonlinear optical crystals is a powerful technique for generating coherent radiation in wavelength ranges spanning from the mid-infrared (mid-IR) to the blue, displaying low thermal load and high efficiency.

This thesis shows how QPM in one- (1D) or two-dimensional (2D) lattices can be employed to engineer novel devices for parametric downconversion in the IR, affording freedom in designing both spectral and angular properties of the parametric output. Experimental demonstrations of parametric devices are supported by theoretical modelling of the nonlinear conversion processes.

In particular, broadband parametric downconversion has been investigated in 1D QPM lattices, through degenerate downconversion close to the point of zero group-velocity dispersion. Ultra-broadband optical parametric generation (OPG) of 185 THz bandwidth (at 10 dB), spanning more than one octave from 1.1 to 3.7 μm, has been achieved in periodically poled 1 mol% MgO-doped near-stoichiometric $LiTaO_3$ (MgSLT) of 25 μm QPM period, pumped at 860 nm. Such broadband gain is of high interest for ultrashort optical pulse amplification, with applications in high harmonic generation, ultrafast spectroscopy and laser ablation. Furthermore, the detrimental impact of parasitic upconversion, creating dips in the OPG spectrum, has been investigated. By altering the pump pulse duration, energy can be backconverted to create peaks at the involved OPG wavelengths, offering a possible tool to enhance broadband parametric gain spectra.

The engineering of the angular properties of a parametric output benefits greatly from 2D QPM, which is investigated in this thesis by the specific example of hexagonally poled MgSLT. It is demonstrated how two OPG processes, supported by a single 2D QPM device, can exhibit angularly and spectrally degenerate signals (idlers). This degeneracy results in a coherent coupling between the two OPG processes and a spectrally degenerate twin-beam output in the mid-IR (near IR). 2D QPM devices exhibiting such coherently coupled downconversion processes can find applications as compact sources of entangled photon-pairs. This thesis further illustrates the design freedom of 2D QPM through the demonstration of a device supporting multiple parametric processes, thus generating multiple beams from the mid-IR to the blue spectral regions.

Keywords: nonlinear optics, parametric processes, frequency downconversion, quasi-phase matching, $LiTaO_3$, broadband downconversion, quadratic cascading, nonlinear photonic crystals, twin-beam generation

Sammanfattning

Denna doktorsavhandling beskriver forskning rörande ickelinjära optiska kristaller som används för att skapa skräddarsydda koherenta infraröda ljuskällor med låg värmeutveckling, drivna av lasrar vid standardvåglängder. Ljuskällorna baseras på s.k. kvasifasmatchning (QPM), där man genom att periodiskt strukturera den andra ordningens ickelinjäritet i kristallen drastiskt kan öka konverteringsgraden till i stort sett vilken våglängd som helst där kristallen är transparent.

Avhandlingen visar hur dessa strukturer, i en eller i två dimensioner, kan användas till infraröda ljuskällor, baserade på s.k. optisk parametrisk frekvenskonvertering, för att ge frihet att designa det konverterade ljuset både spektralt och vinkelmässigt. Avhandlingen beskriver genomförda experiment inom parametrisk konvertering samt hur dessa experiment förklaras och styrks genom teoretisk modellering.

Specifikt beskriver avhandlingen hur endimensionella strukturer har använts till ultrabredbandig parametrisk nedkonvertering som genererade ett 185 Thz brett kontinuum, dvs. som sträcker sig från 1.1 till 3.7 μm våglängd; över mer än en optisk oktav. Detta genomfördes i endimensionellt strukturerade kristaller av stökiometrisk litiumtantalat dopade med 1 mol% magnesiumoxid (MgSLT), drivna av en laser vid 860 nm. Sådant bredbandigt koherent ljus är användbart t.ex. till att förstärka ultrakorta laserpulser, vilka kan användas inom attosekundsfysik, till spektroskopi av ultrasnabba (kemiska) förlopp eller för industriell bearbetning av material. Vidare presenteras en studie i hur ogynnsamma intrinsiska uppkonverteringsprocesser påverkar spektrumet för detta kontinuum. Genom att ändra drivlaserns pulslängd kan deras inverkan förändras, vilket potentiellt erbjuder ett verktyg att förbättra den spektrala profilen hos bredbandiga parametriska ljuskällor.

Tvådimensionella (2D) QPM-strukturer erbjuder särskilda möjligheter till att designa de vinkelmässiga aspekterna hos parametriskt genererat ljus. Detta behandlas specifikt i avhandlingen med en studie av hexagonala QPM-strukturer i MgSLT. Studien demonstrerar hur två simultana nedkonverteringsprocesser, upprätthållna av en och samma QPM-struktur, kan sammankopplas koherent. Detta medför att två separata – men spektralt identiska – strålar av koherent ljus genereras, med tillämpningar inom exempelvis kvantoptik som kompakta ljuskällor av sammanflätade fotoner. Avhandlingen diskuterar vidare hur 2D QPM erbjuder utökade friheter att designa parametriska ljuskällor, t.ex. genom att upprätthålla flera simultana parametriska konverteringsprocesser i en enda ickelinjär kristall. Specifikt presenteras en strålkälla där ett flertal upp- och nedkonverteringsprocesser, i samma 2D QPM-struktur, genererar åtskilliga strålar av koherent ljus med våglängder ända från infrarött till blått.

List of publications

This thesis is based on the following peer-reviewed journal articles:

I. Levenius, M., V. Pasiskevicius, F. Laurell, and K. Gallo, *Ultra-broadband optical parametric generation in periodically poled stoichiometric $LiTaO_3$*, Optics Express **19** (5) 4121-4128 (2011).

II. Gallo, K., M. Levenius, F. Laurell, and V. Pasiskevicius, *Twin-beam optical parametric generation in $\chi^{(2)}$ nonlinear photonic crystals*, Applied Physics Letters **98** (16) 161113-3 (2011).

III. Levenius, M., M. Conforti, F. Baronio, V. Pasiskevicius, F. Laurell, C. De Angelis, and K. Gallo, *Multistep quadratic cascading in broadband optical parametric generation*, Optics Letters **37** (10) 1727-1729 (2012).

IV. Levenius, M., V. Pasiskevicius, and K. Gallo, *Angular degrees of freedom in twin-beam parametric down-conversion*, Applied Physics Letters **101** (12) 121114 (2012).

Description of author's contributions

My contribution to the original articles was the following:

I. I performed the experiments under supervision of Valdas Pasiskevicius and Katia Gallo and I performed the data evaluation accompanied by discussions with Katia Gallo and Valdas Pasiskevicius. I wrote the article with assistance from the co-authors.

II. I took part in the experiments, conducted by Katia Gallo and Valdas Pasiskevicius, and assisted Katia Gallo in the data evaluation. I assisted in writing the article.

III. I performed the experimental work and the data evaluation, accompanied by discussions with Katia Gallo. I performed the comparison of experimental and numerical results, including discussions with Matteo Conforti and Fabio Baronio (of University of Brescia) and Katia Gallo. I wrote the article with assistance from the co-authors, with particular contributions (numerical aspects) from the international collaboration.

IV. I performed the experimental work and the data evaluation, accompanied by discussions with Katia Gallo. I built a numerical model verifying the experimental results (described in section 5.2.2). I wrote the article with assistance from the co-authors.

Further publications

A. M. Levenius, V. Pasiskevicius, F. Laurell and K. Gallo, "Broadband Optical Parametric Generation in Periodically Poled Stoichiometric $LiTaO_3$", Conference on Lasers and Electro-Optics (CLEO), San José, California, USA, oral presentation CFN2, (2010)

B. K. Gallo, M. Levenius, B. Vermersch, V. Pasiskievicius and F. Laurell, "Parametric frequency downconversion devices in periodically poled Mg-doped stoichiometric lithium tantalate" (Invited), International Conference on Transparent Optical Networks (ICTON), Munich, Germany, oral presentation WeC2.2, (2010)

C. K. Gallo, M. Levenius, F. Laurell, V. Pasiskevicius, "Parametric generation in 2D nonlinear photonic crystals", Europhoton, Hamburg, Germany, oral presentation WeD2, (2010)

D. M. Levenius, V. Pasiskevicius, F. Laurell, K. Gallo, "70 THz signal bandwidths through optical parametric processes in periodically poled stoichiometric lithium tantalate", Europhoton, Hamburg, Germany, oral presentation WeD4, (2010)

E. K. Gallo, M. Levenius, F. Laurell, V. Pasiskevicius, "Twin-beam optical parametric generation in nonlinear photonic crystals", Advanced Solid State Photonics (ASSP), Istanbul, Turkey, oral presentation AMA2, (2011)

F. M. Levenius, V. Pasiskevicius, F. Laurell and K. Gallo, "Pump-dependence of spurious cascaded upconversion in broadband optical parametric generation", 2nd EOS Topical Meeting on Lasers (ETML 11), Capri, Italy, oral presentation 4545, (2011)

G. M. Levenius, M. Conforti, F. Baronio, V. Pasiskevicius, F. Laurell, K. Gallo, "Quadratic Cascading Effects in Broadband Optical Parametric Generation", Advanced Solid State Photonics (ASSP), San Diego, California, United States, oral presentation AT2A.3, (2012)

H. M. Levenius, V. Pasiskevicius, F. Laurell and K. Gallo, "Spectral and Angular Mapping of Parametric Generation in Purely Nonlinear Lattices", Conference on Lasers and Electro-Optics (CLEO), San José, California, USA, oral presentation CTh3B.5, (2012)

I. F. Baronio, M. Conforti, M. Levenius, K. Gallo, V. Pasiskevicius, F. Laurell, and C. De Anglelis, "Broadband optical parametric generation in $LiTaO_3$", Italian Meeting on Electromagnetics, Rome, Italy, oral presentation I.16, (2012)

J. M. Levenius, V. Pasiskevicius and K. Gallo, "Cascaded Up-Conversion Of Twin-Beam OPG In Nonlinear Photonic Crystals" Conference on Lasers and Electro-Optics (CLEO) Europe, Munich, Germany, oral presentation CD-7.3, (2013)

K. M. Levenius, V. Pasiskevicius, G. Björk and K. Gallo, "Twin-beam parametric generators based on nonlinear photonic crystals", 20th Central European Workshop on Quantum Optics (CEWQO), Stockholm, Sweden, poster presentation, (2013)

Acknowledgements

First of all I would like to thank my main supervisor, Katia Gallo. I cannot express enough my gratitude for all the hours you invest in your supervision. Without your offer of always being there for discussions about my research, this work would never have reached the quality it has today. I always come out feeling very motivated after meetings with you. You also think one step further and care about your students' well-being beyond just the work, which is a valuable quality of a leader.

I thank my co-supervisor Valdas Pasiskevicius, for many valuable discussions about physics, for important feedback on my publications and for dinner and beer at conferences. I am happy with how you put up with me learning, bit by bit, to handle the necessary equipment in the lab.

I also wish to thank my co-supervisor Fredrik Laurell, for helping me structure all parts of my PhD training and providing insights for my research. You have also given me a perspective on what it is like to handle interpersonal relations within a group, which is most valuable. Last, but not least, thank you for accepting me as a PhD student in your group, making this whole journey possible in the first place, and for making your employees happy through offering innebandy, barbeques, etc.

Thank you, Gunnar Björk, for letting me into your group, and for interesting discussions over lunch and fika.

I want to thank all my colleagues of the Laser physics and Quantum Electronics and Quantum Optics groups for good company at the office, in the lab and on conference trips. I would also like to direct a special thank you to the following: Niels Meiser, for the everyday discussions in our office and hanging out inside and outside of work. Kai Seger, for gaming nights and especially those Magic lunches – which worked as an excellent stress relief. Anna Chiara Brunetti, for company, support and pep talk throughout my thesis writing and for talking about life, the universe and everything. Michele Manzo, for good office company and random jokes to get us through the more monotonous parts of a PhD training.

Thank you to Matteo Conforti for interesting discussions and giving me a broader perspective, both on my research and on life in general.

I am grateful untoward Christophe Codemard, for helpful discussions regarding, and for supplying parts to, my construction of the erbium amplifier for the group's lab.

Lastly, I want to thank my parents, for all your extensive support throughout these years, and being a sounding board for me reflecting upon all my decisions.

Contents

Chapter 1

Introduction

Coherent light sources find applications in numerous areas such as material processing, telecommunication, spectroscopy, display technologies, optical storage, medical treatments, microscopy and imaging. The coherent light can be generated in lasers [1], but in this case one is limited spectrally to the emission bands defined by the energy-level structure of the laser gain medium.

By exploiting *optical parametric frequency conversion* in nonlinear crystals [2] the gaps between the different laser emission bands can be bridged. Parametric processes offer great flexibility for choosing the wavelengths to be generated. In contrast to light generation in laser gain media, the desired wavelength can be selected from an often broad continuous interval.

1.1 Quasi-phase matched frequency conversion

Optical parametric frequency conversion based on second and third order nonlinearities is achieved by mixing coherent waves, e.g. light beams from lasers, in a nonlinear material. The strongest parametric processes, and consequently the first to be discovered, are those generated in nonlinear materials possessing a non-zero second order nonlinearity. These processes are often referred to as quadratic frequency conversion processes.

Quadratic processes are divided into frequency upconversion, generating light at shorter wavelengths, and downconversion, at longer wavelengths. Frequency upconversion can be achieved using a single wave incident on the nonlinear material, generating light at twice the incident frequency, through *second harmonic generation* (SHG) [3]. Alternatively, two incident waves can generate light through *sum frequency generation* (SFG) [4]. In this way a desired frequency, i.e. the sum, is obtained by choosing carefully the frequencies of the incident waves.

Frequency downconversion can be achieved by mixing two incident waves in *difference frequency generation* (DFG) [5], where the generated frequency is defined by the difference of the incident frequencies. Downconversion can also be achieved with a single incident wave (pump) through spontaneous downconversion (annihilation) of its photons, triggered by vacuum fluctuations, and generation of photon pairs (signal and idler) at frequencies which add up to the frequency of the pump. This process is referred to as *optical parametric generation* (OPG) [6]. The OPG process exhibits increased spectral flexibility in that it is capable of generating numerous signal-idler pairs at different frequencies. Furthermore, the process permits a simple experimental geometry in that it requires only a single incident wave, although at the expense of device efficiency.

Using parametric interactions in nonlinear crystals to provide gain for a particular spectral interval also results in much lower thermal load than employing laser gain media. This is due to the fact that there is no energy storage in nonlinear crystals, since parametric interactions do not involve excitation of atoms and consequently no relaxations by emission of phonons.

Various methods to increase the conversion efficiency of parametric interactions were suggested shortly after the first experimental demonstration of SHG [7]. Nowadays, the most commonly used is *quasi-phase matching* (QPM) since it allows for efficient conversion and at the same time is suitable for large scale fabrication [8, 9]. In contrast to birefringent phase matching [10, 11], dominant in the early years of parametric conversion, QPM does not impose constraints on the polarisations of the involved waves. This allows the exploitation of the strongest component the material's nonlinearity, resulting in higher conversion efficiencies. Furthermore, by using QPM the wavelengths to be generated can be selected from broader spectral intervals, encompassing larger portions of the transparency range of the nonlinear material.

The central topic of the work presented in this thesis is investigations of OPG processes supported by QPM. In particular, I have examined two different configuration of the process. The first configuration is broadband OPG in the near infrared (IR) to the mid-IR spectral regions supported by one-dimensional QPM structures. The second configuration consists of the combination of two OPG processes, supported by the same two-dimensional QPM structure, which experience a coherent exchange explained below. Adding to this I have, in both configurations, investigated SFG following the OPG, with both interactions being supported by the same QPM device.

1.2 Broadband engineering using QPM

Parametric downconversion can be configured in such a way that the generated waves exhibit very broad spectral bandwidths, and the two downconverted waves can even overlap in bandwidth. In the frame of this thesis I have investigated such a configuration that provides ultrabroad parametric gain bands spanning from the near IR to the mid-IR regime.

Broad parametric gain bands have attracted increasing interest in the field of ultrashort pulse amplification over the last decade [12], with applications in femto-

second spectroscopy [13], high harmonic generation [14] and laser machining [15]. Broad gain bands are also appealing for tunable sources. In the mid-IR spectral region, in particular, where many molecules have vibrational absorption bands, such sources are important for spectroscopy [16]. Parametric broadband devices can be employed in frequency comb generation [17] and manipulation of wavelength division multiplexing channels in optical telecommunications [18]. Broadband parametric generators have applications in quantum optics, e.g. for multichannel quantum communication [19].

With, particularly, the application of ultrashort pulse amplification in mind, I demonstrate, in this thesis, ultrabroad parametric gain bands, accessible for pulse generation or amplification, through broadband OPG. The experiments were chosen to be performed in 1 mol% MgO-doped near-stoichiometric lithium tantalate (MgSLT) crystals [20], engineered for QPM through periodic poling [8], since the dispersion of MgSLT predicts extremely broad bandwidths that are accessible through QPM [21]. The broadness relied on working close to the point of zero group velocity dispersion of MgSLT and yielded OPG bandwidths exceeding one octave, from 1.1 to 3.7 μm (185 THz). With a coherent seed, the downconversion spectrum could theoretically support amplification of pulses down to 2.4 fs duration.

I also investigated cascaded upconversion (SFG) processes following the ultra-broadband OPG, demonstrating that their normally detrimental impact on the OPG gain spectra could be controlled by adjusting the pump pulse duration. This optical control can thus be used to achieve more uniform spectral gain profiles in broadband parametric devices.

1.3 Spectral-angular engineering using 2D QPM

Conventional QPM devices rely on a periodic modulation of the second order nonlinear electric susceptibility in one dimension. Around fifteen years ago Berger proposed to introduce the QPM modulation in two dimensions, to form two-dimensional (2D) nonlinear photonic crystals (NPCs) [22]. The second dimensionality grants additional degrees of freedom for engineering the output of frequency conversion devices. In upconversion, this has allowed for achieving e.g. multi-beam SHG [23], beam shaping [24] and multi-beam second, third and fourth harmonic generation [25].

Frequency downconversion in NPCs, on the other hand, had been very sparsely investigated prior to this thesis. The work, presented in this thesis, that I have performed on the topic of downconversion in 2D QPM structures constitutes the first experimental investigations of the coherent interplay of two simultaneous downconversion processes associated to two distinct QPM resonances, of comparable strength, in a NPC. This phenomenon is demonstrated in a proof of principle device of hexagonally poled [26] MgSLT, supporting two OPG processes. The device generates dual-beam signal output, i.e. spectrally but not spatially degenerate, in addition to a spectrally and spatially degenerate idler beam, shared by the two OPG processes. I also analysed the tuning of the coherently locked output as a function of pump incidence angle and wavelength.

Furthermore, in the work presented herein I have investigated cascaded multi-beam SFG in the same NPC device sustaining the two coupled OPG processes. The spectral and angular characteristics of the multi-wavelength, multi-beam optical output can be controlled by spectral or angular tuning of the optical pump. The study reveals how coherent sources with complex spectral-angular output can be engineered using the many degrees of freedom offered by NPCs.

The results presented in this thesis could find application in several fields, in particular in quantum optics, where they could provide novel compact sources of entangled photons, and in optical manipulation of signals in telecommunication. Moreover, many applications remain to be discovered as the additional degrees of freedom offered by the, relatively young, field of 2D QPM continue to be explored.

1.4 Outline of thesis

This thesis is based on the original peer-reviewed publications labelled I to IV, reproduced at the end of the printed version of this thesis. These are preceded by six chapters introducing and discussing the key results of my work.

Chapters 2 and 3 provide an introduction to the concepts, mostly theoretical, relevant for the work presented in this thesis. In particular, chapter 2 treats second order nonlinear optical parametric interactions employed in the thesis work. Chapter 3 discusses the concept of QPM and the properties of the nonlinear material used for the experiments, i.e. MgSLT.

Chapters 4 and 5 describe the work performed in the frame of this thesis. The first section of chapter 4 is based on article I and treats broadband OPG in periodically poled MgSLT. The second section is based on article III and describes the investigations of quadratic cascading of SFG in conjunction with a simultaneous broadband OPG in a pulsed temporal regime. Chapter 5 is based on articles II and IV, as well as (so far) unpublished work. It discusses coherently coupled OPG in 2D NPCs, as well as cascaded SFG processes sustained by the same NPC device. Finally, conclusions and outlook for the work described in the thesis are given in Chapter 6.

Chapter 2

Basic principles of nonlinear optics

In a classical picture, light interacts with matter in that the electric field of the light accelerates bound charges within the material, which will then act as oscillating dipoles. The dipoles radiate light at their oscillation frequencies, which in linear regimes will correspond to the frequencies of the incident light. In nonlinear regimes the induced dipoles will not only oscillate at the incident frequencies, but at other frequencies as well, and thus generates light at these new frequencies. Interactions that generate these new frequencies, or amplify existing ones, are often referred to as parametric processes.

2.1 Coupled wave equations

Assuming no free charges and no free currents within the material, it is possible to describe the light-matter interactions by starting from Maxwell's equations. The involved fields are assumed to be monochromatic and are represented by their complex field components. As an example, the real electric field is obtained from the complex field by including the rapidly oscillating part of the field and the complex conjugate, $\tilde{\mathbf{E}}(\mathbf{r},t) = [\mathbf{E}(t)\exp(-i\omega t) + \text{c.c.}]/2$. Thus, in the frequency domain the equations can be written

$$\begin{aligned} \nabla \cdot \mathbf{D} &= 0 \\ \nabla \cdot \mathbf{B} &= 0 \\ \nabla \times \mathbf{E} &= -i\omega\mathbf{B} \\ \nabla \times \mathbf{H} &= i\omega\mathbf{D}. \end{aligned} \tag{2.1}$$

Bold text denotes a vector or tensor quantity. The vector-valued quantities involved are electric and magnetic fields, **E** and **H**, respectively, as well as the corresponding electric displacement field and magnetic flux density, **D** and **B**, respectively.

The displacement field is given by $\mathbf{D} = i\omega(\varepsilon_0\mathbf{E} + \mathbf{P})$, where $\mathbf{P}$ is the polarisation induced by the incident electric field, with frequency ω. With no magnetisation $\mathbf{M}$ in the material $\mathbf{H} = \mathbf{B}/\mu_0$. Inserting the expressions for $\mathbf{D}$ and $\mathbf{H}$ into the fourth of the Eqs. (2.1) and using the relation from the third equation one obtains

$$\nabla \times (\nabla \times \mathbf{E}) = \omega^2\mu_0\varepsilon_0\mathbf{E} + \omega^2\mu_0\mathbf{P}. \tag{2.2}$$

For frequencies away from absorption resonances, the polarisation can be expanded in a Taylor series of the incident electric field. In the expansion, the magnitude of each term decreases rapidly with increasing order.

$$\mathbf{P} = \varepsilon_0\boldsymbol{\chi}^{(1)}\mathbf{E} + \mathbf{P}^{\mathrm{NL}} = \varepsilon_0\left[\boldsymbol{\chi}^{(1)}\mathbf{E} + \boldsymbol{\chi}^{(2)}\mathbf{E}\mathbf{E} + \boldsymbol{\chi}^{(3)}\mathbf{E}\mathbf{E}\mathbf{E} + O(\mathbf{E})^4\right] \tag{2.3}$$

The rank 2 tensor, i.e. matrix, $\boldsymbol{\chi}^{(1)}$ is the linear part of the (electric) susceptibility $\boldsymbol{\chi}$; thus the first term describes interactions in the linear regime. The susceptibility can be viewed as the extent to which an external electric field can displace the charges within the material, giving rise to the induced polarisation. If the higher order terms of the expansion are non-negligible they cause distortions to the otherwise sinusoidal induced polarisation and the response is said to be in the nonlinear regime. The nonlinear part of the susceptibility is described by tensors of rank $N + 1$, $\boldsymbol{\chi}^{(N)}$ $\forall N \in \{2, 3, \dots\}$, and the nonlinear induced polarisation is often denoted $\mathbf{P}^{\mathrm{NL}}$.

In the case of negligible higher order terms, Eq. (2.2) becomes

$$\begin{aligned}\nabla \times (\nabla \times \mathbf{E}) &= \omega^2\mu_0\varepsilon_0\mathbf{E} + \omega^2\mu_0\varepsilon_0\boldsymbol{\chi}^{(1)}\mathbf{E} \\ &= \omega^2\mu_0\varepsilon_0\varepsilon_r\mathbf{E}.\end{aligned} \tag{2.4}$$

Assuming plane waves,

$$\mathbf{E} = \mathbf{A}(\omega)\exp(i\mathbf{k}_0 \cdot \mathbf{r}), \tag{2.5}$$

and using identities from vector calculus Eq. (2.4) is reformulated into the linear Helmholtz equation.

$$(\nabla^2 + k^2)\mathbf{E} = 0 \tag{2.6}$$

We assume wave solutions to this equation that are of the form of Eq. (2.5). The parameter $k^2 = \omega^2\mu_0\varepsilon_0\varepsilon_r = k_0^2\varepsilon_r$ is the absolute value squared of the wave vector within the material, where k_0 is the absolute value of the wave vector in vacuum from the Eq. (2.5) ansatz. It is also possible to use the refractive index of the material, n, to express $k = k_0 n$, since there is no magnetisation (i.e. $\mu_r = 1$).

In the case of a non-negligible nonlinear induced polarisation, $\mathbf{P}^{\mathrm{NL}}$, Eq. (2.2) instead becomes

$$\begin{aligned}\nabla \times (\nabla \times \mathbf{E}) &= \omega^2\mu_0\varepsilon_0\mathbf{E} + \omega^2\mu_0\varepsilon_0\boldsymbol{\chi}^{(1)}\mathbf{E} + \omega^2\mu_0\mathbf{P}^{\mathrm{NL}} \\ &= \omega^2\mu_0\varepsilon_0\varepsilon_r\mathbf{E} + \omega^2\mu_0\mathbf{P}^{\mathrm{NL}}\end{aligned} \tag{2.7}$$

and the nonlinear Helmholtz equation is obtained.

$$(\nabla^2 + k^2)\mathbf{E} = -\frac{k_0^2}{\varepsilon_0}\mathbf{P}^{\mathrm{NL}} \tag{2.8}$$

In Eq. (2.8) the nonlinear part of the interaction is isolated to the right hand side of the equation and $\mathbf{P}^{\mathrm{NL}}$ can be viewed as a source term for different frequencies. These frequencies, as mentioned above, do not necessarily need to be present in the incident electric field.

Since this thesis discusses nonlinear interactions in crystals exclusively, it is convenient to introduce a coordinate system that is the same as the principle dielectric axes of a crystal. The incident field is assumed to travel along x within the material. The vectorial nature of the electric fields, i.e. the polarisation of the light, is expressed by a unit vector $\mathbf{e}$, letting the envelope $\mathbf{A}$ be scalar valued: A. The waves considered in the thesis are all linearly polarised, so this is assumed henceforth. The spatial dependence of the envelope, driven by the nonlinear perturbation of the Helmholtz equation (the right hand side of Eq. (2.8)), is accounted for only along the propagation direction since the plane wave approximation is applied, cf. Eq. (2.5).

$$\mathbf{E} = E\mathbf{e} = A(\omega, x)\mathbf{e}\exp(ikx) \tag{2.9}$$

The field of Eq. (2.9) is inserted into the nonlinear Helmholtz equation (2.8), followed by the application of the slowly varying envelope approximation (SVEA). Owing to the SVEA the second derivative term $d^2A(\omega,x)/dx^2$, created by the Laplace operator, can be neglected, as long as $|d^2A(\omega,x)/dx^2| \ll |k\, dA(\omega,x)/dx|$ i.e. the envelope $A(\omega,x)$ changes slowly in space. Eq. (2.8) thus becomes

$$\frac{dA(\omega,x)}{dx} = i\frac{\omega}{2\varepsilon_0 nc}\exp(-ikx)\,\mathbf{P}^{\mathrm{NL}}\cdot\mathbf{e}. \tag{2.10}$$

The continuation of the derivation will treat the case of *second order* (also called *quadratic* or $\chi^{(2)}$) parametric interactions in non-centrosymmetric materials, i.e. materials with non-zero $\boldsymbol{\chi}^{(2)}$, since that is the focus of this thesis. These materials may have non-zero $\boldsymbol{\chi}^{(3)}$ and higher order terms, but since the expansion of Eq. (2.3) goes to zero so rapidly with increasing order the $\boldsymbol{\chi}^{(2)}$ term is the dominating nonlinear term. Thus the higher order terms can be neglected and the nonlinear polarisation $\mathbf{P}^{\mathrm{NL}}$ will henceforward be described by $\mathbf{P}^{(2)} = \boldsymbol{\chi}^{(2)}\mathbf{E}\mathbf{E}$.

Each of the three Cartesian vector components of the nonlinear polarisation is treated separately. Eq. (2.11) depicts an example where the two incident electric field components $E_k(\omega_2)$ and $E_l(\omega_3)$ induce, through the susceptibility component $\chi^{(2)}_{jkl}(\omega_1 = \omega_2 + \omega_3;\ \omega_2, \omega_3)$, a non-zero polarisation at the sum frequency ω_1, not present in the incident field:

$$P_j^{(2)}(\omega_1) = \sum_{k,l}\sum_{\omega_2,\omega_3} \varepsilon_0\chi^{(2)}_{jkl}(\omega_1 = \omega_2 + \omega_3;\ \omega_2, \omega_3)E_k(\omega_2)E_l(\omega_3) \quad \text{with } j,k,l \in \{x,y,z\} \tag{2.11}$$

To obtain the total polarisation component j at frequency ω_1, the multiple summations of Eq. (2.11) must be performed. The first summation lets the Cartesian indices k and l vary over all possible vectorial components, i.e. possible directions for the polarisation of the incident light. The second summation lets ω_2 and ω_3 assume all values that add up to ω_1.

Regardless of which frequency that is being generated, it is a general condition that the frequencies of the three waves in a quadratic interaction are fixed by energy conservation.

$$\omega_1 = \omega_2 + \omega_3 \tag{2.12}$$

When the involved frequencies are far from absorption resonances the nonlinear susceptibility is real and its dispersion is negligible, thus full permutation symmetry applies. As a result the same value for $\chi^{(2)}_{jkl}$ can be used for all involved frequencies and the frequency arguments can be omitted. It is then convenient to use a different coefficient to denote the nonlinear susceptibility.

$$d_{jkl} = \frac{1}{2}\chi^{(2)}_{jkl} \tag{2.13}$$

The nonlinear coefficient d can also be written in a more compact way, which for interactions where all involved polarisations and electric field components have polarisations aligned along z becomes $d_{33} \equiv d_{zzz}$. (See Ref. [27] for more details on this notation.) In all experimental and numerical investigations presented in this thesis the polarisations of the involved fields lie along z. For simplicity, it is assumed for the rest of the derivation that all induced polarisations also are polarised along z. The Cartesian indices in Eq. (2.11) are then dropped and Eq. (2.10) can be written in scalar form.

$$\frac{dA}{dx} = i\frac{\omega}{2\varepsilon_0 nc}\exp(-ikx)\,P^{\mathrm{NL}} \tag{2.14}$$

Since the Cartesian indices have been omitted a new notation $A_m \equiv A(\omega_m, x)\ \ \forall m \in \{1,2,3\}$ can be introduced.

For $\omega = \omega_1$ the induced polarisation described in Eq. (2.11) generates a field amplitude A_1. Inserting Eq. (2.11) into Eq. (2.14) and using the fact that $E = A(\omega, x)\exp(ikx)$, the differential equation for the evolution of A_1 when propagating through the material is obtained.

$$\frac{dA_1}{dx} = i\frac{\omega_1}{n_1 c}\exp(-ik_1 x)\,d_{33}A_2A_3\exp(ix[k_2 + k_3]) \tag{2.15}$$

Letting $\omega = \omega_2$, Eq. (2.14) can be applied also to the field amplitude A_2. In the same way that the electric field oscillations at ω_2 and ω_3 can induce an oscillation at ω_1, the oscillations at ω_1 and ω_3 can modify the amplitude of the oscillation at ω_2. With all involved polarisations along z, the induced nonlinear polarisation at the difference frequency ω_2, is

$$P^{(2)}(\omega_2) = \sum_{k,l} \sum_{\omega_1,\omega_3} \varepsilon_0 \chi^{(2)}(\omega_2 = \omega_1 - \omega_3;\ \omega_1, -\omega_3) E(\omega_1)[E(\omega_3)]^* . \quad (2.16)$$

Note that the first summation, over all Cartesian indices, now becomes trivial since all involved polarisations lie along z. The complex conjugate in the expression originates from the fact that the negative frequency component (of the complex field representation) of the oscillation at ω_3 is required to create the difference frequency. Inserting Eq. (2.16) into Eq. (2.14), written for ω_2, one obtains the influence that the two oscillations at ω_1 and ω_3 exert on the field amplitude A_2. Using the compact notation the differential equation describing the evolution of A_2 is

$$\frac{dA_2}{dx} = i\frac{\omega_2}{n_2 c} \exp(-ik_2 x)\, d_{33} A_1 A_3^* \exp(ix[k_1 - k_3]) . \quad (2.17)$$

Letting $\omega = \omega_3$, Eq. (2.14) can be applied also to the field amplitude A_3. The induced nonlinear polarisation at the difference frequency ω_3 is

$$P^{(2)}(\omega_3) = \sum_{k,l} \sum_{\omega_1,\omega_2} \varepsilon_0 \chi^{(2)}(\omega_3 = \omega_1 - \omega_2;\ \omega_1, -\omega_2) E(\omega_1)[E(\omega_2)]^* \quad (2.18)$$

and the evolution of A_3, influenced by the oscillations at ω_1 and ω_2, is given by

$$\frac{dA_3}{dx} = i\frac{\omega_3}{n_3 c} \exp(-ik_3 x)\, d_{33} A_1 A_2^* \exp(ix[k_1 - k_2]) . \quad (2.19)$$

The three differential equations (2.15), (2.17) and (2.19), constitute the coupled wave equations. This system describes the evolution of the amplitudes of the three interacting electric field oscillations involved in the quadratic interaction, as the light propagates along x within the nonlinear material.

$$\begin{aligned} \frac{dA_1}{dx} &= i\frac{\omega_1}{n_1 c} d_{33} A_2 A_3 \exp(-i\Delta k x) \\ \frac{dA_2}{dx} &= i\frac{\omega_2}{n_2 c} d_{33} A_1 A_3^* \exp(i\Delta k x) \\ \frac{dA_3}{dx} &= i\frac{\omega_3}{n_3 c} d_{33} A_1 A_2^* \exp(i\Delta k x) \end{aligned} \quad (2.20)$$

The parameter

$$\Delta k = k_1 - k_2 - k_3, \quad k_m = \omega_m n_m \ \forall m \in \{1, 2, 3\}, \quad (2.21)$$

is known as the wave vector mismatch or the *phase mismatch*. It depends on the frequencies of the involved field oscillations and the refractive index of the material. Δk determines the sign of the complex exponential function and thus decides which field amplitudes that increase and which that decrease. In this sense, the phase mismatch is a parameter critically affecting the light generation at the desired frequency. Its role will be discussed more in depth in section 2.3.1.

The electric field oscillations can be seen as three distinct light waves, at different frequencies and thus of different colour. The oscillations influence each other's strengths, in a process mediated by the nonlinear polarisation, which can be seen as energy exchange between the light waves. Since the process takes place far from any absorption resonances, it can be deduced that the generation or destruction of one photon at frequency ω_1 necessitates the destruction or generation of one photon at ω_2 and one photon at ω_3. In other words, the total energy in the system is constant and a change in the intensity of any of the three light waves, $I_m = \frac{1}{2}\varepsilon_0 n_m c|E_m|^2 \ \forall m \in \{1,2,3\}$, is directly related to the others. These connections are described by the *Manley-Rowe relations*.

$$\frac{1}{\omega_1}\frac{dI_1}{dx} = -\frac{1}{\omega_2}\frac{dI_2}{dx} = -\frac{1}{\omega_3}\frac{dI_3}{dx} \tag{2.22}$$

2.2 Parametric frequency upconversion

The solution of the coupled wave equations (2.20) will give the evolution of all the waves interacting in the parametric process as they propagate through the quadratic material. However, in order to solve the system of equations one needs input conditions, or, in other words, decide what waves are input into the crystal and what is the desired output.

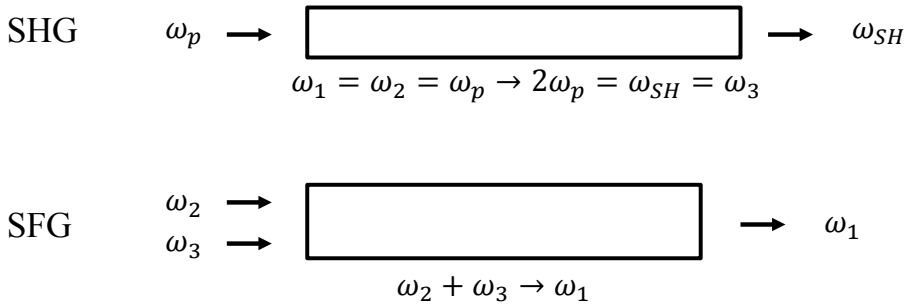

Fig. 2.1 Possible upconversion processes for quadratic parametric interactions. SHG = second harmonic generation, SFG = sum frequency generation

An instructive example to start with is a special case of frequency upconversion which represents the simplest kind of parametric interactions: *second harmonic generation* (SHG). A single wave, referred to as *pump*, is input into the material, often with the purpose of reaching a higher frequency regime. The wave, however, is treated as two input waves that are degenerate, which generate light at twice the input frequency. From a particle point of view, two pump photons are converted into one photon at double frequency (second harmonic (SH)), $\omega_{SH} = \omega_p + \omega_p$. The interaction is depicted in the upper part of Fig. 2.1.

The coupled wave equations (2.20) reduce to a system of two differential equations.

$$\begin{aligned}\frac{dA_{SH}}{dx} &= i\frac{\omega_{SH}}{n_{SH}c}d_{33}\frac{A_p^2}{2}\exp(-i\Delta kx)\\ \frac{dA_p}{dx} &= i\frac{\omega_p}{n_pc}d_{33}A_{SH}A_p^*\exp(i\Delta kx)\end{aligned} \tag{2.23}$$

The factor $1/2$ for the equation of the second harmonic wave reflects that the input is degenerate. In other words, there is only one field in the expression of the induced nonlinear polarisation, Eq. (2.11), thus after summation the polarisation has a factor 2 less than in non-degenerate cases.

If the conversion efficiency of the interactions is low, which is the case in several applications, only a fraction of the pump intensity is transferred to the second harmonic. The decrease in intensity of the pump can then be disregarded, which is referred to as the non-depleted pump approximation. In this case Eq. (2.23) is reduced further in that the differential equation for A_p vanishes and the evolution of the second harmonic intensity as a function of propagation coordinate is straightforward to find.

$$I_{SH}(x) = \frac{\omega_{SH}^2}{2\varepsilon_0 n_p^2 n_{SH} c^3} d_{33}^2 I_p^2\, x^2 \mathrm{sinc}^2\left(\frac{\Delta kx}{2}\right) \tag{2.24}$$

The result emphasises two key parameters of single-input parametric interactions, namely the *pump intensity* and the *phase mismatch*. Both will be further covered in the next section.

The input waves of the upconversion can also be non-degenerate, as is depicted in the lower part of Fig. 2.1. This is the example first used in the derivation of the previous section, where two distinct input waves generate light at the sum frequency (SF) $\omega_1 = \omega_2 + \omega_3$. The process is called *sum frequency generation* (SFG) and often serves the purpose of producing a specific frequency or reaching further towards the blue-UV side of the spectrum.

Solving the full coupled wave equations (2.20) in the non-depleted pump approximation gives the evolution of the generated SF wave.

$$I_1(x) = \frac{2\omega_1^2}{\varepsilon_0 n_1 n_2 n_3 c^3} d_{33}^2 I_2 I_3 x^2\, \mathrm{sinc}^2\left(\frac{\Delta kx}{2}\right) \tag{2.25}$$

2.3 Parametric frequency downconversion

This thesis focuses on parametric downconversion, where the parametric interactions generate frequencies lower than, at least one of, the input frequencies. Out of convention the indices for the waves, 1, 2 and 3, are often replaced by the terms *pump* (*p*), *signal* (*s*) and *idler* (*i*), sorted by descending frequency. The pump is almost always of significantly higher intensity than the two other waves.

Depending on the characteristics of the incident waves and the desired output, downconversion is divided into three differently named processes. The first example,

shown by the top part of Fig. 2.2, is *difference frequency generation* (DFG). The purpose of DFG is most frequently to reach a lower frequency spectral region. Two incident light waves, i.e. electric fields of different frequency, generate a third wave at the difference frequency. The pump is one of the input waves and the other is often the signal, as shown in Fig. 2.2, but can sometimes be the idler depending on the desired output.

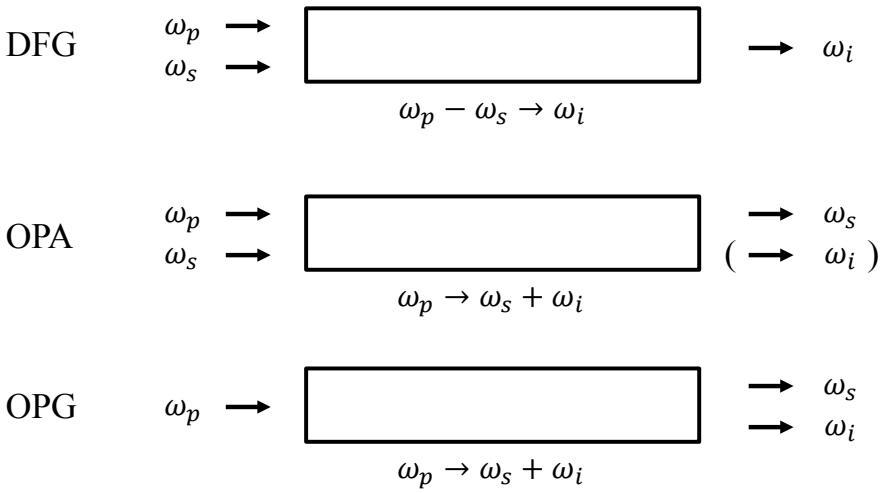

Fig. 2.2 Possible downconversion processes for quadratic parametric interactions. DFG = difference frequency generation, OPA = optical parametric amplification, OPG = optical parametric generation

If one instead is interested is interested in amplifying the a wave at lower frequency one discusses *optical parametric amplification* (OPA), shown by the middle part of Fig. 2.2. Again, the example shown here is the more frequent one using pump and signal input, although it is possible to use pump and idler as input. Energy is removed from the pump and converted to amplify the signal input wave, and, as a side effect, an idler wave is also generated and amplified. Most downconversion experiments with two input waves operate at intensity levels where the result is OPA, i.e. net amplification for both signal and idler waves.

It is also possible to input only the pump wave into the material, for a third version of downconversion: *optical parametric generation* (OPG) or *spontaneous parametric downconversion* (SPDC). In this case the conversion process is seeded by photons originating from quantum vacuum fluctuations. Both the signal and the idler waves are generated in OPG. The aspects of downconversion that are described throughout the rest of this chapter apply to OPA, DFG and OPG alike.

As described in the previous section by Eq. (2.12), the involved frequencies obey energy conservation, which is often written $\omega_p = \omega_s + \omega_i$ for downconversion. For the rest of this thesis, the indices 1, 2 and 3 are replaced by p, s and i whenever downconversion is treated.

The characteristics of parametric interactions, and frequency downconversion in particular, are developed further by an example using the non-depleted pump approximation. The decrease of intensity of the pump is thus disregarded, which allows

for easier calculations. A more general description was given early on by Armstrong et al. [7].

By assuming that the pump is undepleted, $dA_p/dx = 0$, the coupled wave equations (2.20) reduce to a system of two coupled equations. Following the derivations of [28] the solution to the system is found to be

$$\begin{aligned} A_s(z) &= \left[A_s(0)\left(\cosh bx - i\frac{\Delta k}{2b}\sinh bx\right) + \frac{\kappa_i A_p}{b}A_i^*(0)\sinh bx\right]\exp\left(i\frac{\Delta k x}{2}\right) \\ A_i(z) &= \left[A_i(0)\left(\cosh bx - i\frac{\Delta k}{2b}\sinh bx\right) + \frac{\kappa_s A_p}{b}A_s^*(0)\sinh bx\right]\exp\left(i\frac{\Delta k x}{2}\right) \end{aligned} \tag{2.26}$$

with the following parameters.

$$\begin{aligned} \kappa_m &= i\frac{\omega_m d_{33}}{n_m c} \quad m \in \{s, i\} \\ b &= \sqrt{\Gamma^2 - \left(\frac{\Delta k}{2}\right)^2} \\ \Gamma^2 &= \frac{2\omega_s\omega_i}{\varepsilon_0 n_p n_s n_i c^3} d_{33}^2 I_p \end{aligned} \tag{2.27}$$

The gain experienced by an incident signal (in the case of pump and signal wave input, with no incident idler wave; $A_i(0) = 0$) after propagating through a material of length L is

$$\begin{aligned} g_s(L) &= \frac{|A_s(L)|^2}{|A_s(0)|^2} - 1 \\ &= \Gamma^2 \frac{\sinh^2\left(L\sqrt{\Gamma^2 - \left(\frac{\Delta k}{2}\right)^2}\right)}{\Gamma^2 - \left(\frac{\Delta k}{2}\right)^2}. \end{aligned} \tag{2.28}$$

In the limit of a weak pump wave, where $\Gamma \ll \Delta k/2$, Eq. (2.28) reduces to

$$g_s(L)|_{\Gamma\,\text{small}} = \Gamma^2 L^2\,\text{sinc}^2\left(\frac{\Delta k L}{2}\right). \tag{2.29}$$

If the phase mismatch, Δk, is small the signal intensity grows with approximately the square of the length of the nonlinear material.

On the other hand, in the case of a very strong pump in relation to the phase mismatch, $\Gamma \gg \Delta k/2$, Δk is neglected and the signal grows approximately exponentially with the length.

$$g_s(L)|_{\Gamma\,\text{large}} = \frac{1}{4}\exp(2\Gamma L) \tag{2.30}$$

In order to achieve an efficient conversion to the signal frequency (the conversion to the idler behaves similarly, owing to the Manley-Rowe relations (2.22)) in an experiment it is rewarding to be in the regime of Eq. (2.30). The gain grows rapidly

both with increasing *length L* of the nonlinear material and with increasing *pump intensity*. The latter influences the gain through Γ, as is seen in the third expression of (2.27). Since Eq. (2.30) requires Δk to be small in order to be valid, the *phase mismatch* is almost always the most important parameter in the experimental conditions when striving for an efficient conversion. To this end, the phase mismatch is discussed in detail below.

2.3.1 Phase matching

In light of Eqs. (2.24), (2.25) and (2.29) it is clear that for a non-zero Δk the intensity generated through the conversion will oscillate between zero and a finite number as the waves propagates through the material. This can be easily seen in the example of SHG, by rewriting again the expression for the second harmonic intensity at a given coordinate in the material, Eq. (2.24).

$$I_{SH}(x) = \frac{\omega_{SH}^2}{2\varepsilon_0 n_p^2 n_{SH} c^3} d_{eff}^2 I_p^2 \frac{4}{(\Delta k)^2} \sin^2\left(\frac{\Delta k x}{2}\right) \tag{2.31}$$

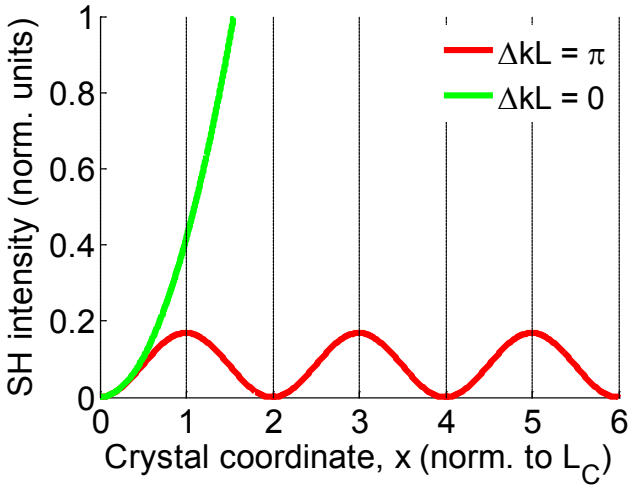

Fig. 2.3 Phase matched (green) and non-phase matched (red) second harmonic generation as function of position in the quadratic material, modelled by Eq. (2.31). Position expressed in coherence lengths L_C of the non-phase matched interaction.

The evolution of the second harmonic intensity is plotted in Fig. 2.3. For the case of non-zero Δk (red curve), the sine squared expression first increases monotonically with x, then starts to decrease when $|\Delta k x/2| = \pi/2$. The distance travelled when the direction of the energy flow changes, L_C, is the *coherence length* of the nonlinear process.

$$L_C = \frac{\pi}{|\Delta k|} \tag{2.32}$$

When reaching one coherence length, the light generated earlier at ω_{SH} will no longer be in phase with the polarisation wave at ω_{SH}, since the light at ω_p, which induced the polarisation, is travelling with a different phase velocity than the light at ω_{SH}. The light generated at ω_{SH} after one coherence length will thus interfere destructively, resulting in a downconversion, back to ω_p, of the previously generated light. One coherence further into the material the light wave at ω_{SH} is completely depleted and, subsequently, the induced polarisation at ω_{SH} can once more generate light at ω_{SH}. In this way, a portion of the intensity supplied by the pump wave will flow back and forth between the second harmonic and the pump during propagation throughout the material. To obtain instead a monotonic upconversion (green curve in Fig. 2.3) one must ensure that $L_C \gg L$ which is done by letting $\Delta k \cong 0$, i.e. achieve *phase matching*.

A first possible method to accomplish phase matching is to use birefringence to compensate for the material's dispersion, i.e. the refractive index as function of frequency, which is responsible for the phase difference acquired through propagation. The method is referred to as *birefringent phase matching*, first demonstrated in 1962 [10, 11]. By choosing different (linear) polarisations for the fields of the interacting waves they experience different refractive indices within the crystal. The different indices can thus balance the phase mismatch so that the wave vectors add up to zero and Δk vanishes.

Another method consists of introducing a periodic phase flip of π, e.g. after every coherence length, for either the generated light wave or the polarisation generating it. In this way one could avoid the destructive interference that would otherwise arise after every coherence length. The concept is referred to as *quasi-phase matching* (QPM), since the phase velocities of the interacting waves are not matched even though the destructive interference is minimised and the generated intensity grows monotonically.

Armstrong et al. suggested [7] that QPM could be achieved by letting the interacting waves propagate at an angle within a plane-parallel slab of nonlinear material, such as a nonlinear crystal, in such a way that they would undergo total internal reflection after having propagated a distance corresponding to an odd multiple of the coherence length. This phase matching scheme is referred to as *Fresnel QPM* and was first demonstrated in 1966 [29].

In the same report by Armstrong et al., another implementation of the phase flip is presented. If the orientation of the induced second order polarisation were to change by 180° this would effectively change its sign, which corresponds to a phase flip of π for the wave being generated. This can be achieved by changing the geometry of the nonlinear material periodically, so that after the distance of one (or an odd number of) coherence length(s) the material is repositioned upside down. The sign of the coefficient of the second order term of the nonlinear polarisation expansion (Eq. (2.3)), i.e. the second order susceptibility $\chi^{(2)}$, will change periodically throughout the material, as will the sign of the second order polarisation. The magnitude of $\chi^{(2)}$, however, remains unaltered, as do all the linear properties of the material. In the first experimental demonstrations of this version of QPM the interacting waves passed through several nonlinear crystals, thin in the x-dimension, where each crystal orient-

ed upside down with respect to the previous. The thickness of the thin plates were one [30] or an odd number of [31] coherence length(s), to avoid the destructive interference after every or after some propagated coherence lengths, thus achieving QPM. Nowadays, however, there are more efficient ways to achieve the change in geometry that permits QPM (in a single nonlinear crystal), as will be discussed in chapter 3.

So far, for the sake of simplicity, all waves have been assumed to propagate collinearly, as illustrated by the wave vector diagram of a downconversion example in Fig. 2.4a. However, in the more general case it is possible for the waves to travel in non-collinear directions, as sketched for downconversion in Fig. 2.4b. In that case the phase mismatch is given by a vectorial relation,

$$\Delta\mathbf{k} = \mathbf{k}_1 - \mathbf{k}_2 - \mathbf{k}_3. \tag{2.33}$$

It should be noted that since the polarisation of the waves lies along z they propagate in the x-y-plane, i.e. the wave vectors have the form $\mathbf{k}_m = k_{m,x}\hat{\boldsymbol{x}} + k_{m,y}\hat{\boldsymbol{y}}$. Large propagation angles may limit the interaction length due to *spatial walkoff*, i.e. the waves move away from each other laterally along y. Consequently the overlap in space is diminished, reducing the conversion efficiency, until the waves no longer occupy the same space and the interaction stops.

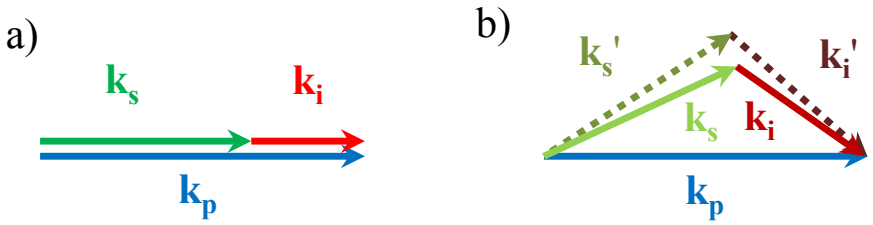

Fig. 2.4 a) Collinear and b) non-collinear interactions geometries exemplified for parametric downconversion. The non-collinear geometry displays two cases of slightly different signal and idler frequencies and propagation angles.

In summary, the conditions that determine which frequencies that partake in a conversion process are momentum conservation, given by $\Delta\mathbf{k} = 0$ in Eq. (2.33), and energy conservation, through Eq. (2.12). By solving a system of these two equations one obtains the working points of most efficient conversion; the *phase matched* working points.

For SHG, SFG, DFG and OPA the frequencies of the two input waves (being degenerate in the case of SHG) define a single solution for the system of Eqs. (2.12) and (2.33) with $\Delta\mathbf{k} = 0$. For OPG the situation is different: the system is underdetermined, owing to the single input, and the frequencies and propagation directions of the signal and idler are not unique. A slight change in the propagation directions of the signal and idler waves changes somewhat the interaction geometry, see Fig. 2.4b, and thus permits slightly different wave vector lengths, i.e. different frequencies. For this reason, in OPG, frequencies close to the intended working point are always generated, though usually with lower efficiency, at neighbouring output angles.

For parametric interactions, since Eq. (2.33) depends on the refractive index, the dispersion of the employed nonlinear material decides which frequencies that can

be generated from the incident frequencies, in a particular experimental configuration. In downconversion, the relation between incident and generated frequencies can be visualised by plotting the wavelengths of the signal and idler versus the wavelength of the pump. An example is shown in Fig. 2.5a, calculated for QPM in 1 mol% magnesium-doped near-stoichiometric $LiTaO_3$ (MgSLT) using Eqs. (2.12) and (2.21), along with the Sellmeier equations of Ref. [21]. The wavelengths indicated in Fig. 2.5a are calculated for $\Delta k = 0$, however, neighbouring wavelengths can also be generated, albeit with a lower conversion efficiency. To then see the relative intensities of all wavelengths that are to be expected from a particular pump wavelength (and pump intensity) a plot such as Fig. 2.5b can be used. Fig. 2.5b depicts how the variation of Δk as function of the generated wavelengths is reflected in the gain (Eq. (2.28)), which in turn is proportional to the generated intensities. In such a figure it is also easier to gauge the bandwidth of the conversion process, which will be of interest in the next section.

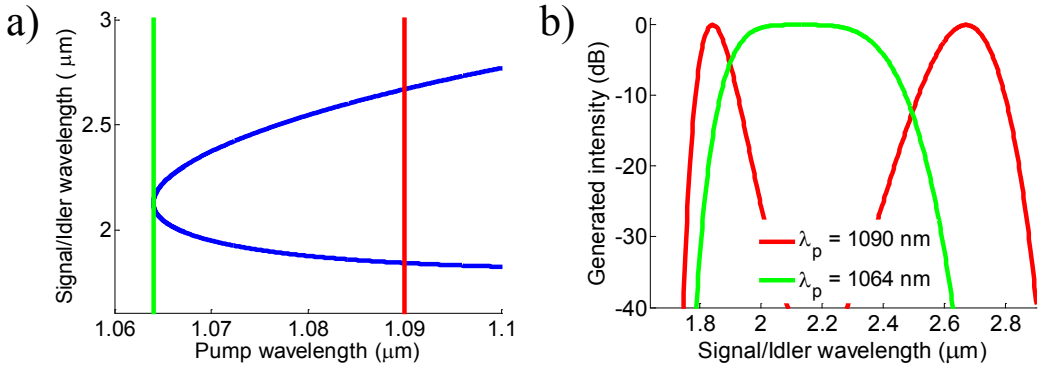

Fig. 2.5 a) Phase matched wavelengths for frequency downconversion in MgSLT as function of pump wavelength (blue curve). QPM was assumed, with a period of 32.48 μm. The red and green lines specify two example pump wavelengths. b) Relative intensities, in normalised logarithmic scale, of the wavelengths generated by the two pump wavelengths indicated in a).

2.4 Broadband downconversion

One field where parametric interactions prove remarkably useful is generating extremely broad continua of coherent light. The first challenge that arises when trying to achieve phase matching for a broad band of frequencies in downconversion is to overcome the group velocity mismatch between signal and idler waves. This section is devoted to explaining this challenge and suggesting how it can be handled.

To be able to describe how the frequencies in the vicinity of a phase matched working point in downconversion behave, the phase mismatch

$$\Delta k = k_p - k_s - k_i \tag{2.34}$$

is expanded in a Taylor series with respect to the signal frequency, following [32]. Mathematically, ω_{s0} is then fixed at the working point $(\omega_{s0}, \omega_{i0})$ and the signal

frequency to be investigated is given by the variable $\omega_s = \omega_{s0} + \Delta\omega$, where $\Delta\omega$ is the deviation from the working point.

$$\Delta k(\omega_0 + \Delta\omega) = k_p - k_s - k_i + \frac{\partial \Delta k}{\partial \omega_s}\Delta\omega + \frac{1}{2}\frac{\partial^2 \Delta k}{\partial \omega_s^2}(\Delta\omega)^2 + O(\Delta\omega)^3 \tag{2.35}$$

The coefficient of the first order term of the expansion is the derivative of the phase mismatch with respect to the signal frequency and is given by

$$\frac{\partial \Delta k}{\partial \omega_s} = -\frac{\partial k_s}{\partial \omega_s} - \frac{\partial k_i}{\partial \omega_s}. \tag{2.36}$$

The pump frequency is fixed, thus varying the signal frequency also alters the idler frequency. The relation between the two can be derived from $\omega_i = \omega_p - \omega_s$:

$$\frac{\partial}{\partial \omega_s} = \frac{\partial}{\partial \omega_i}\frac{\partial \omega_i}{\partial \omega_s} = -\frac{\partial}{\partial \omega_i} \tag{2.37}$$

Inserting (2.37) into (2.36) the derivative $\partial\Delta k/\partial\omega_s$ becomes

$$\frac{\partial \Delta k}{\partial \omega_s} = -\frac{\partial k_s}{\partial \omega_s} + \frac{\partial k_i}{\partial \omega_i}, \tag{2.38}$$

where one identifies the group velocities, $v_g = \partial\omega/\partial k$, of signal and idler. The group velocities depend on the nonlinear material and the involved frequencies.

The coefficient of the second order term, i.e. the second derivative of the phase mismatch is calculated analogously.

$$\frac{\partial^2 \Delta k}{\partial \omega_s^2} = -\frac{\partial^2 k_s}{\partial \omega_s^2} + \frac{\partial}{\partial \omega_s}\frac{\partial k_i}{\partial \omega_i} = -\frac{\partial^2 k_s}{\partial \omega_s^2} - \frac{\partial^2 k_i}{\partial \omega_i^2} \tag{2.39}$$

The two terms found in the expression above are the group velocity dispersion (GVD), $\beta_2 = \partial^2 k/\partial\omega^2$, of signal and idler and depend on the nonlinear material and involved frequencies. Assuming that phase matching is achieved at the working point, the Taylor expansion can be written as follows.

$$\Delta k(\omega_0 + \Delta\omega) = \left(\frac{1}{v_{gi}} - \frac{1}{v_{gs}}\right)\Delta\omega - \frac{1}{2}(\beta_{2s} + \beta_{2i})(\Delta\omega)^2 + O(\Delta\omega)^3 \tag{2.40}$$

Even though continuous-wave broadband downconversion has been reported [33], broad bands are most often exploited for (ultra-)short pulse interactions. There can be various motivations behind this, but one prominent is the desire to obtain high peak powers. High peak powers can be achieved by shortening the pulse duration while keeping the pulse energy constant. However, short pulses can in some cases pose a problem for broadband phase matching.

In the pulsed case *temporal walkoff* can arise, which is the loss of spatial overlap due to the differences in propagation speed, i.e. group velocity v_g, of the signal, idler and pump pulse. In particular, the group velocity mismatch between the pump

and the downconverted pulses dominates, to a first order, the temporal walkoff. It is thus useful to define a pulse-splitting length between the two:

$$l_{mp} = \frac{\tau}{\delta_{mp}}, \tag{2.41}$$

where τ is the pump pulse duration and

$$\delta_{mp} = \frac{1}{\frac{1}{v_{gm}} - \frac{1}{v_{gp}}}, \qquad m \in \{s, i\}. \tag{2.42}$$

The challenge of temporal walkoff is more easily pictured in a time frame moving with the pump pulse. If the signal and idler pulses walk off in the same direction from the pump pulse, $\delta_{sp}\delta_{ip} > 0$, the pulse-splitting lengths limit the interaction length within the nonlinear material. However, if signal and idler pulses walk off in different directions from the pump pulse, $\delta_{sp}\delta_{ip} < 0$, the signal and idler group velocities work in favour of concentrating newly generated photons close to the pump pulse. Thus spatial overlap with the pump can be sustained for lengths substantially exceeding the pulse-splitting lengths [12].

2.4.1 Experimental methods for broadband downconversion

The Taylor expansion of the phase mismatch around the phase matching point, $\Delta k(\omega_0 + \Delta\omega)$ Eq. (2.40), indicates that to achieve broadband phase matching one must cause the terms in the expansion to approach zero. The first instance is to realise group-velocity matching (GVM) for the signal and idler pulses, i.e. bring the first term in Eq. (2.40), $\left(v_{gi}^{-1} - v_{gs}^{-1}\right)\Delta\omega$, to zero.

One method, extensively used for phase matching broad bands in downconversion, exploits non-collinear geometry. The method was first realised in β-BaB_2O_4 (BBO) in 1994 [34, 35] and since then bands up to ~190 THz have been realised [36]. Fig. 2.6a depicts the phase matching geometry. Even though Eq. (2.40) has been derived for a scalar, i.e. collinear, case, it can still applicable for this method by separating the vectorial phase mismatch $\Delta\mathbf{k}$ in scalar components parallel to and perpendicular to the signal wave vector. The two components of the phase mismatch are differentiated with respect to signal (and thus idler) frequency and rearranging the result one finds the condition for GVM [12]:

$$v_{gs} = v_{gi}\cos(\Omega), \tag{2.43}$$

Ω is the angle between the signal and idler propagation directions as defined in Fig. 2.6. GVM is thus achieved by exploiting the in-plane degrees of freedom, so that the projection of the idler group velocity on the signal wave vector becomes equal to the signal group velocity, illustrated in Fig. 2.6b. Without ensuring the appropriate value for Ω the different group velocities of signal and idler cause temporal walkoff, as is exemplified by Fig. 2.6c ($\Omega = 0$). Further details can be found in [37].

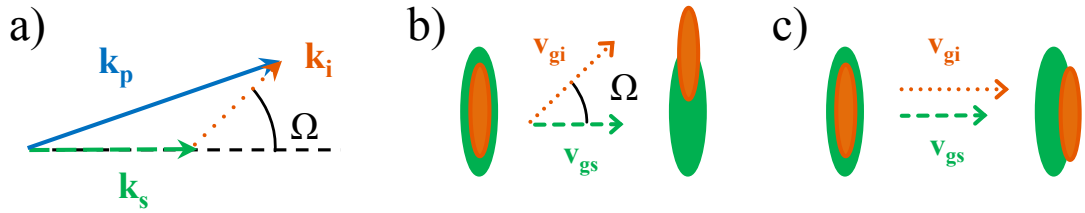

Fig. 2.6 Group-velocity matching (GVM) by non-collinear interaction geometries to achieve broadband phase matching in frequency downconversion. a) The phase matching geometry. b) The elimination of temporal walkoff by exploiting the geometry illustrated in a). Green ellipse represents signal pulse and orange ellipse idler. c) The same interaction suffering temporal walkoff, i.e. due to group velocity mismatch, when utilising collinear interaction geometry.

The method is often used for broadband generation in the shorter wavelength regime and BBO is the most often selected nonlinear material. This is because of BBO's exceptional capability of achieving GVM using birefringence and of its high damage threshold in the visible. However, one limitation of the non-collinear GVM method is spatial walkoff, which ultimately limits the interaction length. The pulses are also generated with a pulse front tilt [38], which complicates their use in applications.

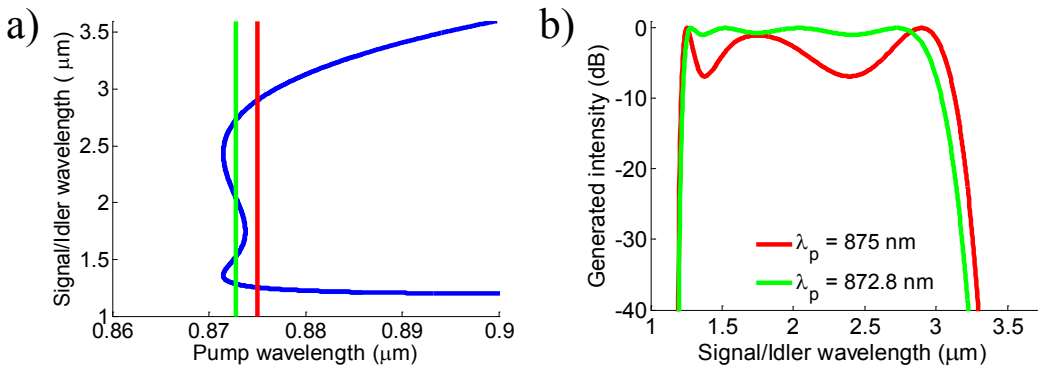

Fig. 2.7 a) Phase matched wavelengths for frequency downconversion in MgSLT as function of pump wavelength (blue curve). QPM was assumed, with a period of 26 μm. The red and green lines show two example pump wavelengths. b) Relative intensities, in normalised logarithmic scale, of the wavelengths generated by the two pump wavelengths indicated in a). The curves are calculated in the same way as for Fig. 2.5. Note the difference in the scale for the signal/idler wavelengths, compared to Fig. 2.5.

An alternative method, employed in this thesis, is to find a spectral working point where the dispersion of the material in itself evolves to satisfy the GVM for the signal and idler, in collinear geometries. The principle of the method is to select and phase match a working point close to the spectral point of zero GVD, as will be explained further on. In Fig. 2.7 an example of the bands of signal and idler wavelengths that can be phase matched in a QPM interaction in MgSLT with a Ti:sapphire pump is shown.

Employing QPM permits working points to be chosen from a greater part of the transparency region of the nonlinear material than when birefringent phase matching is used, as is mentioned in chapter 3. Since the second method is collinear it also offers better spatial overlap permitting longer interaction lengths, ultimately increasing the conversion efficiency.

The OPG signal bandwidth can be derived from Eq. (2.40) and the gain expression of the downconversion, Eq. (2.28). As the signal frequency deviates from the phase matched working point, eventually the phase mismatch Δk will grow large and, as is easily seen e.g. in Eq. (2.29), the gain will decrease. A first approximation of the signal bandwidth, $\Delta\upsilon$ full width at half maximum (FWHM), is given by its dependence on the mismatch between the signal and idler group velocities, defined analogously to Eq. (2.42). It was first derived in Ref. [39].

$$\Delta\upsilon \cong \frac{2\sqrt{\ln 2}}{\pi}\sqrt{\frac{\Gamma}{L}}\frac{1}{|\delta_{si}|} \tag{2.44}$$

When GVM is achieved one instead needs to take into account the second order term of the Taylor expansion Eq. (2.40) to express the FWHM bandwidth [39].

$$\Delta\upsilon \cong \frac{2\sqrt[4]{\ln 2}}{\pi}\sqrt[4]{\frac{\Gamma}{L}}\frac{1}{\sqrt{|\beta_{2s}+\beta_{2i}|}} \tag{2.45}$$

The most important parameter determining the bandwidth in Eq. (2.45) is the GVD at the signal and idler frequencies. Note that the bandwidth is given by the inverse of the sum of signal and idler GVDs, not the difference. In other words, the evolution of the GVDs when moving further away from the phase-matched point must cancel each other. Thus, the way to achieve extremely broad bands is to choose a spectral working point of degenerate downconversion, i.e. $\omega_s = \omega_i$, close to the point of zero GVD of the nonlinear material. In this way, owing to the dispersion of the material, the signal and idler GVDs cancel each other over a very wide range of frequencies.

Owing to the spectral flexibility of QPM, a working point close to the point of zero GVD can be readily achieved in collinear geometry (second broadband phase matching method mentioned above), thus increasing the signal bandwidth beyond what is possible with only GVM. Although a working close to the point of zero GVD restricts the choice of spectral region for the broadband downconversion, the method allows for extremely broad bands in combination with simple phase matching geometries. In recent years the method has started to be investigated experimentally and bandwidths up to 150 THz have been demonstrated so far [40-43].

There exists a third method to achieve phase matching for broadband downconversion. However, it doesn't rely on matching the group velocities, but consists of exploiting QPM with a QPM chirped period, i.e. the spatial period of the sign alterations of $\chi^{(2)}$ changes monotonously (often linearly) along the propagation direc-

tion of the waves.[1] This grants the possibility to engineer the group delay spectrum, through different spectral components being generated at different points along the length of the QPM structure [44-46]. Choosing carefully the group delay as function of frequency, one can compensate for the non-matched group velocities and obtain broadband conversion. Nevertheless, the method reduces the efficiency of the conversion, since for each spectral component only a part of the full length of the nonlinear material is used.

2.5 Quadratic cascading

As described in section 2.3.1, in the case of non-zero phase mismatch, Δk, energy supplied by the incident wave(s) will flow back and forth between the generated and the incident frequencies, as the waves propagate through the nonlinear material. It was noted already in 1967 that periodic energy exchange in a $\chi^{(2)}$ conversion process leads to nonlinear phase shifts for the incident wave [47]. The nonlinear phase shifts are intensity dependent, thus similar to the ones induced by $\chi^{(3)}$ interactions. Despite being treated theoretically early on, experimental limitations hindered any practical interest until the first measurements of the nonlinear phase shifts in 1989 and 1992 [48, 49]. The process that induces these nonlinear phase shifts is called *quadratic cascading* or $\chi^{(2)}$ *cascading*.

The mechanism responsible for the nonlinear phase shifts can be illustrated using the simple case of SHG, in type I phase matching[2]. The interplay between the second harmonic and the fundamental is shown in Fig. 2.8, where Fig. 2.8a describes schematically the principle during one oscillation period. The functions describing the propagation of the second harmonic (SH) and the fundamental waves are found by solving numerically the coupled wave equations (2.23), with a non-zero Δk. The solutions, i.e. the intensity evolution of the SH and fundamental waves and the phase evolution of the fundamental wave, are shown Fig. 2.8b.

As the SH wave grows the pump wave loses an equal amount of energy. After one coherence length, when the SH wave is subject to destructive interference, that energy is converted back to the pump frequency. However, since the SH wave has travelled with a phase velocity different than the one of the pump, $v_{\varphi,SH} \neq v_{\varphi,p}$ in Fig. 2.8a, when the wave is backconverted to the pump frequency it has accumulated a phase shift, $\Delta\varphi$, with respect to the wave at the pump frequency. The result after the backconversion is that the initial wave has acquired a phase shift. In this sense the quadratic cascading is similar to self-phase modulation based on $\chi^{(3)}$ (SPM), but the process exploits the second order susceptibility $\chi^{(2)}$ instead of the third order $\chi^{(3)}$. Quadratic cascading can be expected to be more efficient than SPM since the values of the $\chi^{(2)}$ components are higher than those of the $\chi^{(3)}$ components.

---

[1] The concept of QPM period is further explained in chapter 3.
[2] Type I (birefringent) phase matching: the two incident waves at fundamental frequency have the same polarisation, thus being fully degenerate and indistinguishable.

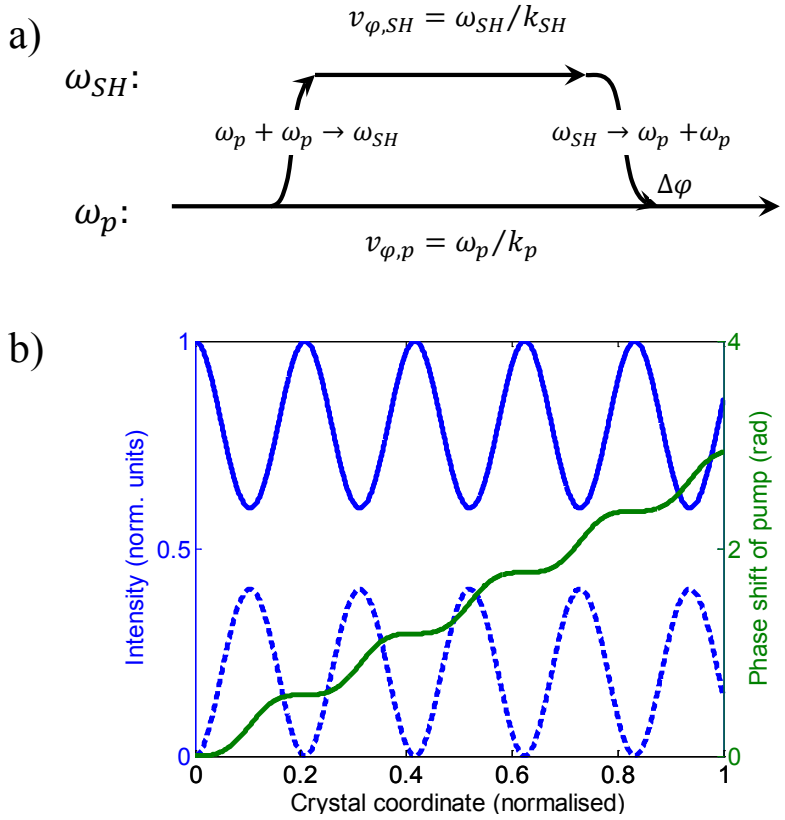

Fig. 2.8 a) Schematic figure of a single cycle of the energy transfer in quadratic cascading of non-phase matched SHG. b) Generated SH intensity (dashed blue curve), fundamental intensity (solid blue curve) and nonlinear phase acquired by the fundamental wave as function of propagated distance. The curves are found by solving numerically the coupled wave equations for SHG (2.23), with $\Delta k \neq 0$.

The magnitude of the $\chi^{(2)}$ cascading phase shift is dependent on the distance that the wave has travelled at the SH frequency. Consequently, it is dependent on the phase mismatch, since e.g. a smaller Δk lets the light propagate longer at ω_{SH} before being backconverted. Moreover, for a smaller Δk more light has time to be upconverted and backconverted. As a result, the total phase shift of the fundamental wave, corresponding to the accumulation of all the phase-shifted photons, increases with increasing pump intensity since for higher pump intensities the conversion efficiency is higher, see e.g. Eq. (2.28), and more photons are converted to ω_{SH}.

Quadratic cascading can arise also at perfect phase matching, when two non-degenerate, incident waves interact, e.g. type II SHG[3] or SFG, and the incident intensities (or more precisely the photon fluxes) are non-equal. Belostotsky et al. showed theoretically, by solving numerically the coupled wave equations for type II SHG (2.20), that the induced nonlinear phase shifts of the involved waves lead to periodic changes in intensity of all the waves for imbalanced inputs [50].

[3] Type II (birefringent) phase matching: the two incident waves at fundamental frequency have different polarisation, thus being non-degenerate and distinguishable.

The reason for the periodic changes in intensity, shown in Fig. 2.9a, can be explained using the coupled wave equations (2.20) and Fig. 2.9. For convenience, Eqs. (2.20) are repeated here as Eqs. (2.46).

$$\begin{aligned}\frac{dA_1}{dx} &= i\frac{\omega_1}{n_1 c} d_{33} A_2 A_3 \exp(-i\Delta k x)\\ \frac{dA_2}{dx} &= i\frac{\omega_2}{n_2 c} d_{33} A_1 A_3^* \exp(i\Delta k x)\\ \frac{dA_3}{dx} &= i\frac{\omega_3}{n_3 c} d_{33} A_1 A_2^* \exp(i\Delta k x)\end{aligned} \tag{2.46}$$

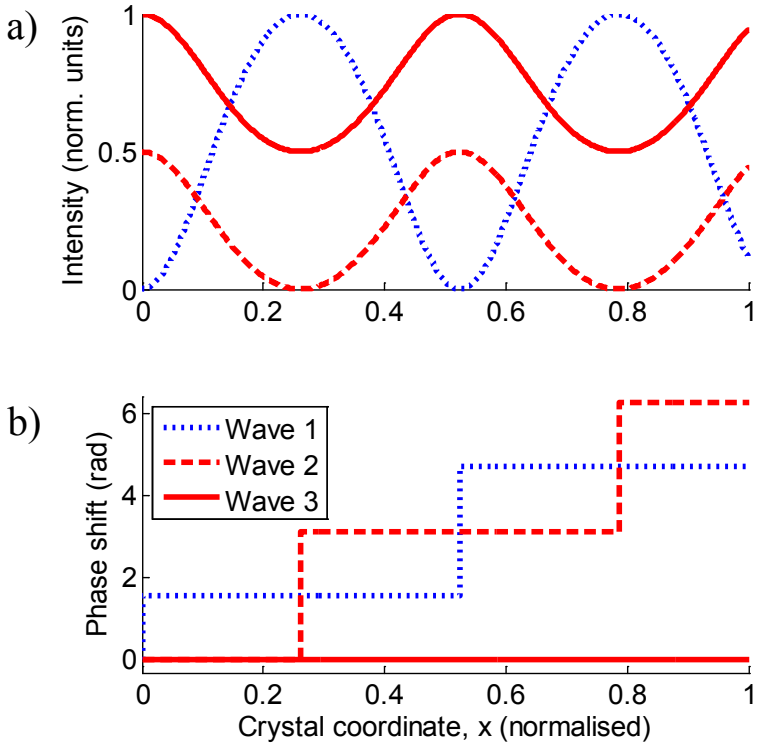

Fig. 2.9 a) Intensities of waves involved in type II, i.e. non-degenerate, SHG cascading due to non-equal input intensities, as function of propagated distance. b) Evolution of phases of the involved waves. The curves have been created by solving numerically the coupled wave equations (2.46), with $\Delta k = 0$, $I_1(0) = 0$ and $I_3(0) = I_2(0)/2$. The numbering of the waves refers to Eqs. (2.46).

Waves 2 and 3 are incident on the nonlinear material, with non-equal intensities $I_3 > I_2$. The intensities of the two waves are reduced and the intensity of wave 1 is increased, until the intensity of wave 2 is zero. Now the driving terms for waves 1 and 3, i.e. the right hand side for the first and third equations of (2.46) are also zero. The only non-zero driving term is that of wave 2 and a wave at frequency ω_2 is thus generated, though with its phase shifted by π radians compared to the initial wave 2. The result is a destructive interference for wave 1, i.e. downconversion to waves 2 and 3. This downconversion continues until wave 1 has zero intensity and the two driving terms of waves 2 and 3, second and third equations of (2.46), become zero. The non-

zero driving term for the first equation of (2.46) generates a wave at frequency ω_1, but with a phase shift of π with respect to wave 1 before its disappearance. As a result, the flow of energy in the conversion process changes back to upconversion. In this manner the entire course of events is repeated periodically. In conclusion, the imbalance of the input intensities is crucial for obtaining $\chi^{(2)}$ cascading at perfect phase matching, $\Delta k = 0$. If this imbalance is not present, when wave 2 reaches zero intensity so does wave 3 and the conversion process terminates itself, with the result of full conversion to ω_1. A review of $\chi^{(2)}$ cascading is given by [51].

In the work presented in this thesis, quadratic cascading has been investigated for SFG cascading with $\Delta k = 0$, in connection with broadband downconversion. It is shown in chapter 4 that in the pulsed regime, SFG cascading can be initiated by temporal walkoff.

Chapter 3

Engineered quadratic materials

As discussed in section 2.3.1, efficient parametric conversion, i.e. eliminating Δk, was first achieved using birefringent phase matching [10, 11]. Today's maturity in growth processes and optical power handling capacity of certain birefringent nonlinear materials, such as β-BaB_2O_4, KDP and LiB_3O_5, render them a favoured alternative in high power applications. However, a limitation of birefringent phase matching lies in that the difference between the refractive indices of the nonlinear material must be large enough to accommodate for the index differences of the involved frequencies. This restricts the spectral range where phase matching can occur. Additionally, when exploiting birefringent crystals it is not uncommon that the phase matching geometry causes Poynting vector walkoff, which can lead to degradation of the spatial profile of a beam and limited effective interaction lengths.

In contrast, since quasi-phase matching (QPM) does not directly rely on a material property, the spectral working point can be chosen freely (as long as the periodicity is achievable with present technology) within the transparency range of the nonlinear material. QPM can also be used for non-birefringent materials, such as GaAs, GaP and GaN, where birefringent phase matching is impossible. No restrictions are imposed on the polarisations the waves when using QPM, so the conversion can exploit the largest component of the nonlinear susceptibility tensor. For the material of concern of this thesis, $LiTaO_3$, this largest component corresponds to d_{33}.

3.1 Quasi-phase matching (QPM)

As already mentioned, the first demonstration of quasi-phase matching employed Fresnel QPM [29] (cf. section 2.3.1) which had been suggested by Armstrong et al. [7]. However, this version of QPM suffers from difficulties in fabricating slabs of

very uniform thickness and low roughness, as well as ensuring the required input angle.

Instead the second approach suggested in the same report by Armstrong et al., i.e. to alternate the orientation of the material, and thus the sign of the second order susceptibility $\chi^{(2)}$ (cf. Eq. (2.3)), every coherence length, attracted interest. One first approach of placing consecutive thin crystal plates of alternating orientation [30, 31] carries the disadvantages of the air gaps, which in almost all situations induce Fresnel losses, and of problems with producing plates with thicknesses equal to a single coherence length. Diffusion-bonding the plates helps to reduce the propagation losses and can allow large apertures [52, 53], but ensuring a constant periodicity across the aperture of the bonded crystal and along the propagation direction remains challenging.

An alternative way to achieve QPM and avoid the inherent Fresnel losses is to implement the structure with domains of alternating sign of the second order susceptibility $\chi^{(2)}$ in a single nonlinear crystal. In this case the created structure is often referred to as a *QPM grating* or *QPM lattice*. One way to manufacture such a single-crystal QPM lattice is to invert the sign of the second order susceptibility during growth of the material. Changing the conditions periodically during the growth can affect the growth so that one obtains crystals with alternating orientation [54]. However, the method is susceptible to fluctuations in the periodicity and accumulated errors in the period along the QPM propagation direction.

For materials that can be grown epitaxially, such as GaAs or GaP, the periodicity of the QPM lattice created during growth can be much more reliable because it can be defined by a photolithographically patterned template. The domains of alternating sign of the susceptibility are grown laterally, i.e. along the aperture of the crystal, and, hence, in parallel rather than sequentially in time. The growth method consists of first fabricating a thin layer of opposite orientation on top of the nonlinear crystal. Photoresist is deposited and patterned using photolithography, which defines the period, and according to this pattern selected parts of the layer of opposite orientation is removed by chemical etching. As a result the top surface of the crystal displays domains of alternating orientation and is used as template for molecular beam epitaxy, which conserves the pre-defined domains during growth. The method is called orientation patterned (OP) crystal growth [55, 56]. To create larger crystal apertures, thicker crystals can be grown by adding a step of hydride vapour phase epitaxy (HVPE) [9].

Single-crystal QPM lattices can also be created in as grown materials, thus making it possible to completely separate the process of creating the QPM lattice from the crystal growth process. This is the case for ferroelectric materials, such as $LiNbO_3$, $LiTaO_3$ or $KTiOPO_4$ (KTP), where the polarity of a ferroelectric domain determines the sign of the second order susceptibility. By applying an electric field the polarity of a domain can be switched (the crystal orientation is flipped) and the sign of the susceptibility is changed. Periodic electrodes can be created on the top surface of the ferroelectric crystal, by patterning a deposited layer of photoresist using photolithography and subsequently evaporating metal on the top of the crystal. Applying the field through the electrodes creates periodic domains where the polarity, and

thus the sign of the susceptibility, is changed. Since the electrodes are lithographically defined, the method ensures good control of the periodicity of the QPM lattice. This method to switch or invert the domains ferroelectric materials is called electric-field poling and was first successfully demonstrated by Yamada et al. [8], quickly followed by several other groups [57, 58].

This thesis focuses on parametric interactions achieved with QPM relying on periodically (electric-field) poled ferroelectric crystals. All QPM lattices used in the experiments of this thesis have been created using electric-field poling. Periodic poling will be described in detail in section 3.3, though first the implications of using QPM to phase match $\chi^{(2)}$ interactions will be discussed.

3.1.1 The QPM principle

In nonlinear material with an implemented QPM lattice the nonlinear coefficient d_{33} is a spatially varying function $d(x)$, periodic in x. The coupled wave equations (2.20) are still valid for QPM, if d_{33} is replaced by $d(x)$ [59].

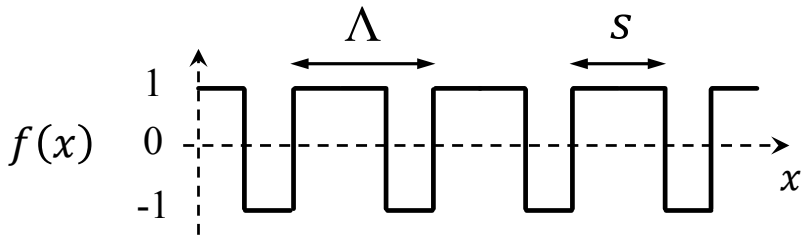

Fig. 3.1 The definitions of the duty cycle $D = s/\Lambda$, the period Λ and the periodic function $f(x)$ of the QPM lattice.

The spatially varying function is written $d(x) = d_{33} f(x)$, where $f(x)$ is a dimensionless function changing from -1 to 1 with periodicity Λ (outlined in Fig. 3.1). $d(x)$ can be expanded in a Fourier series, yielding

$$d(x) = d_{33} \sum_{l=-\infty}^{\infty} F_l \exp(iG_l x)\,. \tag{3.1}$$

The QPM lattice period, Λ, defines the spatial frequencies G_l of the expansion

$$G_l = \frac{2\pi l}{\Lambda} \tag{3.2}$$

and the Fourier coefficients are given by

$$F_l = \frac{1}{\Lambda} \int_0^{\Lambda} f(x) \exp(-iG_l x)\, dx\,. \tag{3.3}$$

The modification of Δk that needs to be performed can be found by inserting Eq. (3.1) into the coupled wave equations (2.20). For instance, the first equation becomes

$$\frac{dA_1}{dx} = i\frac{\omega_1}{n_1 c} A_2 A_3 d_{33} \sum_{l=-\infty}^{\infty} F_l \exp(-i[\Delta k - G_l]x)\,. \tag{3.4}$$

For almost all values of l, the terms in the sum will be fast oscillating so that the integration along the propagation length throughout the crystal, averages out to zero. Only the term $l = l'$, for which $\Delta k - G_{l'} \cong 0$, will quickly dominate over the oscillating terms of the sum. In other words, the sum can be approximated with the l' term. This case occurs when the lattice adds a spatial phase shift that matches the phase mismatch caused by the index differences of the frequencies involved in the parametric conversion. Since only one term dominates the sum, only its contribution needs to be taken into account in Δk, which then can be replaced as

$$\Delta k \rightarrow \Delta k = k_1 - k_2 - k_3 - G_{l'} \tag{3.5}$$

and the nonlinear coefficient d_{33} needs to be replaced by a scalar d

$$d_{33} \rightarrow d = d_{33} F_{l'}. \tag{3.6}$$

$G_{l'}$ is the magnitude of the *reciprocal lattice vector* (RLV) for l'^{th} order QPM and the full description of the RLV is the vector valued parameter $\mathbf{G}_{l'}$. In discussions where only one QPM vector is relevant, the index of the RLV is dropped and the RLV is denoted $\mathbf{G}$.

The most critical parameter for achieving phase matching is the period Λ, see Eqs (3.2) and (3.5), but the *duty cycle* $D = s/\Lambda$, defined in Fig. 3.1, also affects the parametric interaction. It affects the magnitude of the nonlinear coefficient, and thus the conversion efficiency, which is seen by combining Eq. (3.6) and the following, explicit expression of the Fourier coefficients:

$$F_l = \frac{2}{\pi l} \sin(\pi l D) \exp(-i\pi l D) \tag{3.7}$$

In order to maximise the conversion efficiency it is preferable to use low order QPM, since $F_l \propto 1/l$. For first-order QPM, the duty cycle that maximises the conversion efficiency is $D = 1/2$, corresponding to a Fourier coefficient equal to $2/\pi$. Despite this reduction of the nonlinear coefficient (cf. Eq. (3.6)) the resulting effective nonlinear coefficient d may still be much larger than in the case of birefringent phase matching, since the largest component of the susceptibility tensor can be chosen for QPM.

3.1.2 Phase matching calculations

For collinear QPM interactions the period Λ required to achieve phase matching is calculated using the scalar form of the phase mismatch, i.e. taking the magnitude of

the RLV into account. For perfect phase matching of a quadratic parametric process, i.e. $\Delta k = 0$, the lattice vector must obey

$$G = k_1 - k_2 - k_3. \tag{3.8}$$

Assuming first order interactions and combining Eqs. (2.32), (3.2) and (3.8) one obtains

$$\Lambda = 2L_C = \frac{2\pi}{k_1 - k_2 - k_3}. \tag{3.9}$$

For non-collinear interactions the vectorial aspects of the phase mismatch must be taken into account and $\mathbf{\Delta k}$, from Eq. (2.33), is replaced as

$$\mathbf{\Delta k} \rightarrow \mathbf{\Delta k} = \mathbf{k}_1 - \mathbf{k}_2 - \mathbf{k}_3 - \mathbf{G}. \tag{3.10}$$

Thus the phase mismatch must vanish along the two dimensions of $\mathbf{\Delta k}$, i.e. one needs to solve a system of two equations in the x-y-plane. This corresponds to closing a QPM vector diagram, such as the one in Fig. 3.2a. In practical terms, this means finding a suitable QPM period whose RLV $\mathbf{G}$ can phase match the wavelengths and propagation directions of the involved waves.

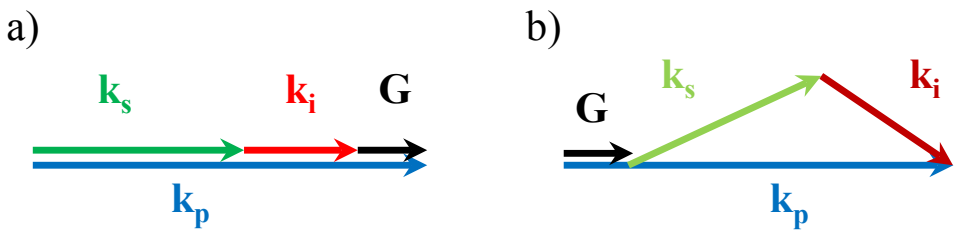

Fig. 3.2 Examples of a) collinear and b) non-collinear interactions geometries for parametric downconversion, phase matched by a QPM vector, also referred to as reciprocal lattice vector (RLV), $\mathbf{G}$. The parallel vectors have been slightly displaced for reasons of visibility.

For the design of QPM structures, in view of a specific conversion process, one is often interested in how the generated frequencies vary as functions of pump frequency, for a chosen QPM period. To illustrate this one can solve the system of equations given by the requirement of energy conservation

$$\omega_1 = \omega_2 + \omega_3 \tag{3.11}$$

and phase matching, also referred to as momentum conservation,

$$\mathbf{G} = \mathbf{k}_1 - \mathbf{k}_2 - \mathbf{k}_3, \tag{3.12}$$

for a given QPM period, in other words a chosen RLV $\mathbf{G}$. An example of this, in the context of downconversion was given in Fig. 2.5a. The pump dependence is displayed by a plot of the generated signal and idler wavelengths versus the pump wavelength. Analogously, one can compose a graph showing the influence of the QPM period by keeping the pump wavelength fixed. The prediction of the generated

wavelengths can be further refined by fixing both the QPM period and the pump wavelength and calculating how the variation of the magnitude of $\Delta\mathbf{k}$, as given by Eq. (3.10), influences the generated intensities, described e.g. by Eq. (2.28), as a function of wavelength, as shown in Fig. 2.5b.

3.2 Two-dimensional QPM

The idea of using QPM with 2D lattices was first presented in 1998 by Berger [22]. 2D QPM lattices are also called (2D) *nonlinear photonic crystals* (NPCs) due to the periodicity in the $\chi^{(2)}$ part of the susceptibility but lack of modulation in the $\chi^{(1)}$ (linear) part. The added second dimensionality grants new degrees of freedom in customising the response of nonlinear devices, albeit with the disadvantage of a reduced effective nonlinear coefficient d, as will be shown later in this section. Berger suggested the first examples of applications that are possible with the new degrees of freedom of NPCs: the possibility to phase match conversion processes in multiple directions, which could find application in ring cavities, and multiple wavelength SHG using a broadband source [22].

Multi-beam generation with different propagation directions (using a narrowband source) was demonstrated in the first experimental realisation, in periodically poled $LiNbO_3$ [23]. Two SHG beams ware generated symmetrically to the pump, each supported by a RLV, so called *twin-beam* SHG. At larger output angles signatures of third and fourth harmonics were noted. Upon changing the input angle of the pump a much richer response, in comparison to one-dimensional (1D) lattices, was observed owing to the many possible phase matching resonances (RLVs).

Third and fourth harmonic generation through multistep SHG and SFG were further investigated, mapping both wavelength and temperature tuning bands [25]. The authors also reported broader acceptance bandwidths using 2D rather than 1D lattices, due to the non-collinear nature of the interactions.

The possibility of efficient conversion at low pump intensities by combining 2D lattices with planar waveguides was demonstrated with twin-beam SHG [60]. The angular tunability of the device was investigated, showing how the two SH beams were spectrally degenerate at zero degree pump angle and split symmetrically in the spectral domain when increasing the pump angle.

The new degrees of freedom of 2D QPM also permit simultaneous conversion and beam shaping of various kinds. This has been experimentally demonstrated by creating e.g. flat-top [61], Bessel [62] and Airy beams [24].

Especially interesting are the possibilities, granted by 2D QPM lattices, of making multiple $\chi^{(2)}$ parametric processes to interact with each other. Such interplays of multiple nonlinear resonances unfold the prospects of spectral-angular responses lacking counterpart in 1D QPM geometries, with examples reported for SHG [60, 63].

3.2.1 2D QPM lattices

For 2D QPM lattices the nonlinear coefficient d_{33} is replaced by a function varying periodically in two spatial dimensions, $d(x,y) = d_{33}f(x,y)$, where, as in section 3.1.1, $f(x,y)$ is a dimensionless spatially varying function. To build the mathematical representation of the lattice one can follow Ref. [64] and define a base of two spatial vectors, of which linear combinations can span all the lattice points.

The base of the two non-parallel vectors $\mathbf{a}_1 = (x_1, y_1)$ and $\mathbf{a}_2 = (x_2, y_2)$ can describe the coordinate vector to each point of a 2D QPM lattice by the vector

$$\mathbf{r}_{lm} = l\mathbf{a}_1 + m\mathbf{a}_2, \qquad l,m \in \mathbb{Z}^2. \tag{3.13}$$

All lattice points are then described by a sum of Dirac delta functions.

$$q(\mathbf{r}) = \sum_{l,m} \delta(\mathbf{r} - \mathbf{r}_{lm}) = \sum_{l,m} \delta(\mathbf{r} - l\mathbf{a}_1 - m\mathbf{a}_2) \tag{3.14}$$

There are thus two periods in a 2D QPM lattice, which are the distances between two lattice points along either of the base vectors, i.e. the lengths of the two base vectors. The sum is to be convolved with a *motif* function, describing the shape of the region, situated at each lattice point, with opposite sign of the nonlinear coefficient. This region can be referred to as the motif of the lattice, hence motif function.

For a circular motif of radius R the motif function becomes

$$s(\mathbf{r}) = \operatorname{circ}\left(\frac{r}{R}\right) \equiv \begin{cases} 1 & r < R \\ -1 & r > R \end{cases}, \qquad r = |\mathbf{r}| = \sqrt{x^2 + y^2}. \tag{3.15}$$

The QPM lattice is bounded by its physical size, represented by an area function. In many situations the lattice is rectangular, with length L and width W, which gives the area function

$$a(\mathbf{r}) = \operatorname{rect}\left(\frac{x}{L}\right) \cdot \operatorname{rect}\left(\frac{y}{W}\right), \tag{3.16}$$

where the rect function is defined by

$$\operatorname{rect}(x) \equiv \begin{cases} 1 & |x| < 1/2 \\ 0 & |x| > 1/2 \end{cases}. \tag{3.17}$$

The complete mathematical expression for the spatially varying nonlinear coefficient becomes

$$d(x,y) = d_{33} \cdot f(x,y) = d_{33} \cdot a(\mathbf{r}) \cdot [q(\mathbf{r}) \otimes s(\mathbf{r})]. \tag{3.18}$$

where $\otimes$ is the convolution operator.

In analogy with 1D QPM lattices (cf. section 3.1.1), using Fourier analysis one can find a representation for the 2D QPM lattice of a parametric interaction, in the reciprocal space: the reciprocal lattice.

Similar to the real space lattice, two base RLVs are needed to span all lattice points in the reciprocal lattice, given by

$$\mathbf{G}_{lm} = l\mathbf{b}_1 + m\mathbf{b}_2, \quad l,m \in \mathbb{Z}^2. \tag{3.19}$$

The two base vectors are related to the real lattice base vectors by

$$\mathbf{a}_j \cdot \mathbf{b}_k = 2\pi\delta_{jk}, \qquad j,k \in \{1,2\}, \tag{3.20}$$

where δ_{jk} is the Kronecker delta.

The function that describes the lattice points in the reciprocal space is the 2D Fourier transform of $q(\mathbf{r})$.

$$Q(\mathbf{G}) = \frac{(2\pi)^2}{A_{UC}} \sum_{l,m} \delta(\mathbf{G} - \mathbf{G}_{lm}) = \frac{(2\pi)^2}{A_{UC}} \sum_{l,m} \delta(\mathbf{G} - l\mathbf{b}_1 - m\mathbf{b}_2) \tag{3.21}$$

$A_{UC} = |x_1 y_2 - y_1 x_2|$ represents the area of the unit cell [65].

Similarly, the motif and the area functions in reciprocal space are given by the Fourier transforms of $s(\mathbf{r})$ and $a(\mathbf{r})$, respectively. For some specific functions the transforms can be written analytically, for example for the circular motif function of Eq. (3.15) the transform is

$$S(\mathbf{G}) = \frac{4\pi R}{G} J_1(RG), \qquad \mathrm{G} = |\mathbf{G}| = \sqrt{G_x^2 + G_y^2}, \tag{3.22}$$

where J_1 is a Bessel function of the first kind. For the rectangular area function, Eq. (3.16), the transform is

$$A(\mathbf{G}) = LW \,\mathrm{sinc}\left(\frac{LG_x}{2}\right) \cdot \mathrm{sinc}\left(\frac{WG_y}{2}\right). \tag{3.23}$$

The general description of the spatial modulation of the reciprocal lattice is then given by $F(\mathbf{G})$, which is the Fourier transform of the spatially varying part of the nonlinear coefficient $f(x,y)$, cf. Eq. (3.18).

$$F(\mathbf{G}) = A(\mathbf{G}) \otimes Q(\mathbf{G}) \cdot S(\mathbf{G}) \tag{3.24}$$

In the case of the length and width of the real lattice being much larger than the dimensions of the unit cell ($x_1, x_2 \ll L$ and $y_1, y_2 \ll W$), the function describing the spatial modulation of the nonlinear coefficient becomes the following sum,

$$f(x,y) = \sum_{l,m} F_{lm} \exp(i\mathbf{G}_{lm} \cdot \mathbf{r}) \tag{3.25}$$

with the Fourier coefficients

$$F_{lm} = \frac{1}{A_{UC}} S\left(\frac{\mathbf{G}_{lm}}{2\pi}\right). \tag{3.26}$$

In analogy with the 1D QPM lattice, the spatial frequencies $\mathbf{G}_{lm}$ are given by the periods in the two dimensions, as defined by $\mathbf{a}_1$ and $\mathbf{a}_2$. Thus, the spatially varying nonlinear coefficient of this case is given by

$$d(x,y) = d_{33} \sum_{l,m} F_{lm} \exp(i\mathbf{G}_{lm} \cdot \mathbf{r}) \tag{3.27}$$

The magnitude of the nonlinear coefficient is affected by the Fourier coefficients, as seen in Eq. (3.27). As a consequence, the modified nonlinear coefficient, and thus the conversion efficiency, depends on the geometry of the lattice (through the unit cell area), the motif (through the Fourier transform of the motif function) and the QPM orders l, m.

As with the 1D QPM lattice, the results of the periodic nonlinear coefficient can be included in the coupled wave equations by modifying the (vectorial) phase mismatch $\Delta\mathbf{k}$ and the nonlinear coefficient d_{33}. It can be noted that the modified phase mismatch for 2D lattices is the same as that of 1D non-collinear interactions, Eq. (3.10), with the exception that also the RLVs can be (mutually) non-collinear. For interaction geometries with little variation in the transverse dimension, i.e. slightly non-collinear waves, the coupled wave equations derived in section 2.1 are sufficient to describe the parametric interaction.

To demonstrate the modifications of the coupled wave equations needed for 2D QPM, the modified version of the first of the coupled wave equations (2.20) is given below, as an example.

$$\frac{dA_1}{dx} = i\frac{\omega_1}{n_1 c} A_2 A_3 d_{33} \sum_{l=-\infty}^{\infty} F_{lm} \exp(-i[\Delta\mathbf{k} - \mathbf{G}_{lm}] \cdot \mathbf{r}) \,. \tag{3.28}$$

By the same argument as with the 1D lattice (cf. section 3.1.1), only the terms for which $\Delta\mathbf{k} - \mathbf{G}_{l'm'} \cong 0$ will dominate over the remaining, fast oscillating terms of the sum. The modifications to Eqs. (2.20) then result in the phase mismatch being replaced by

$$\Delta\mathbf{k} \rightarrow \Delta\mathbf{k} = \mathbf{k}_1 - \mathbf{k}_2 - \mathbf{k}_3 - \mathbf{G}_{l'm'} \tag{3.29}$$

and the nonlinear coefficient d_{33} by a scalar d

$$d_{33} \rightarrow d = d_{33} F_{l'm'}. \tag{3.30}$$

In discussions of 2D QPM a RLV is spoken of in general terms, the index of the RLV is dropped and the RLV is denoted $\mathbf{G}$. However, when referring to the two base RLVs of a 2D QPM lattices the notation $\mathbf{G}_1 \equiv \mathbf{G}_{10}$ and $\mathbf{G}_2 \equiv \mathbf{G}_{01}$ is used.

In conclusion, the ability of a lattice to sustain parametric interactions is crucially dependent on its RLVs (and thus on the lattice geometry and period), since their orientation and magnitude govern which interactions and which frequencies that are phase matched, by influencing $\Delta\mathbf{k}$ (cf. Eq. (3.29)). Using low-order RLVs (l and m small) increases conversion efficiencies, as seen from Eq. (3.26), Eq. (3.19) and e.g. Eq. (3.22). The motif of the lattice also affects the conversion efficiency, through the Fourier coefficients, as seen from Eq. (3.30) and Eq. (3.26).

To end this section, the example of hexagonal lattice geometry will be highlighted.

A microscope photograph of a hexagonal lattice and an illustration of its reciprocal lattice are shown in Fig. 3.3. The lattice geometry is defined by the following base vectors (in real space), whose periods in the two dimensions are chosen to be equal, Λ.

$$\begin{aligned}\mathbf{a}_1 &= \Lambda\left(\frac{1}{2}, \frac{\sqrt{3}}{2}\right)\\ \mathbf{a}_2 &= \Lambda\left(\frac{1}{2}, -\frac{\sqrt{3}}{2}\right)\end{aligned} \tag{3.31}$$

The unit cell area thus becomes $A_{UC} = \sqrt{3}\Lambda^2/2$. For the reciprocal lattice the base RLVs for the hexagonal geometry are

$$\begin{aligned}\mathbf{b}_1 &= \frac{4\pi}{\Lambda\sqrt{3}}\left(\frac{\sqrt{3}}{2}, \frac{1}{2}\right)\\ \mathbf{b}_2 &= \frac{4\pi}{\Lambda\sqrt{3}}\left(\frac{\sqrt{3}}{2}, -\frac{1}{2}\right).\end{aligned} \tag{3.32}$$

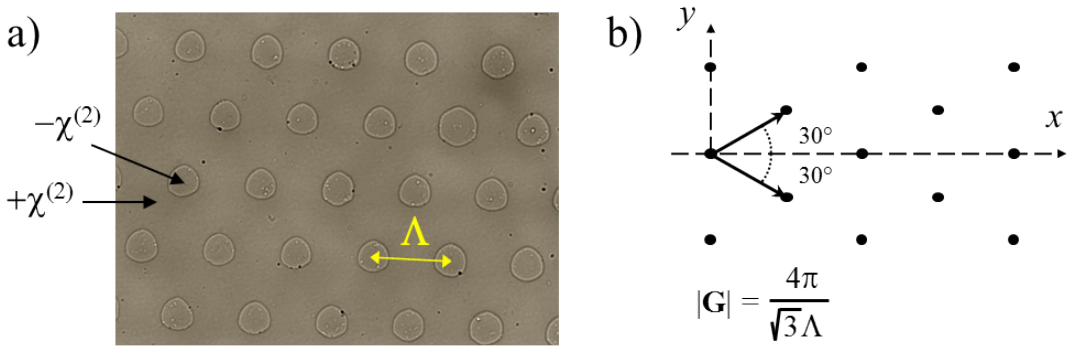

Fig. 3.3 a) A detail of a hexagonal QPM lattices of period Λ = 22.8 µm, fabricated in 0.5 mm thick MgSLT crystals, as revealed by a light etch in hydrofluoric acid. b) Reciprocal hexagonal lattice with the two base RLVs, situated symmetrically at an angle of 30° to the x axis.

A circular motif gives the following Fourier coefficients for the hexagonal lattice [64]. As above, the parameters l and m determine the QPM orders.

$$F_{lm} = \frac{2R}{\Lambda\sqrt{l^2 + m^2 + lm}} J_1\left(\frac{4\pi R}{\Lambda\sqrt{3}}\sqrt{l^2 + m^2 + lm}\right) \tag{3.33}$$

Choosing $R/\Lambda = 1/4$, which would correspond to a 50% duty cycle in a 1D lattice, the Fourier coefficient of a (0,1) order interaction becomes $F_{01} = 0.29$. This gives a modified nonlinear coefficient of $0.29d_{33}$, which can be compared with the modified nonlinear coefficient for a first order interaction in a 50% duty cycle 1D lattice, $\frac{2}{\pi}d_{33} = 0.64d_{33}$. Comparing with a 1D lattice QPM, this corresponds to an approximate reduction of the gain in 2D QPM lattices by a factor of $d_{2D}^2/d_{1D}^2 =$

$(0.29d_{33})^2/(0.64d_{33})^2 \approx 0.2$ (cf. Eqs. (2.27) and (2.28)). Despite this, conversion efficiencies of 60% have been demonstrated experimentally in 2D QPM lattices [23].

Analytical expressions of other lattice geometries and motifs, and comparisons thereof, can be found in Ref. [66].

3.2.2 Ewald sphere construction

To take into account the multitude of RLVs of a 2D QPM lattice when determining the QPM period Λ, required to phase match a particular parametric interaction, Berger suggested to use a nonlinear version of a method already developed for crystallography, Ewald construction [22].

To explain the method an example of SFG is considered, where two waves (labelled p and i) generate SF waves, phase matched by a hexagonal 2D QPM lattice is illustrated in Fig. 3.4. In the figure $\mathbf{k}_i$, $\mathbf{k}_p$, and $\mathbf{k}_{SF}$ designate the wave vectors of the waves involved in the SFG. The method is based on a QPM vector diagram, i.e. energy conservation (e.g. Eq. (3.11)) and momentum conservation (e.g. Eq. (3.12)) pictured in the reciprocal space. However, instead of using a single RLV, a grid representing the reciprocal lattice of Eq. (3.19) is employed. The grid is spanned by the base RLVs, $\mathbf{G}_1 = 1\boldsymbol{b}_1 + 0\boldsymbol{b}_2$ and $\mathbf{G}_2 = 0\boldsymbol{b}_1 + 1\boldsymbol{b}_2$, and thus represents all RLVs. The frequencies and propagation angles of the initial waves, p and i, are selected, which fixes the lengths and angles of their wave vectors. Energy conservation fixes the length of the SF wave vector, but its angle is unknown. The length of the SF wave vector then describes a circle, the *Ewald sphere*, and wherever it intersects any point of the RLV grid phase matching, i.e. momentum conservation, is achieved. Each intersection defines the output angle of a SF wave, i.e. a possible SFG resonance.

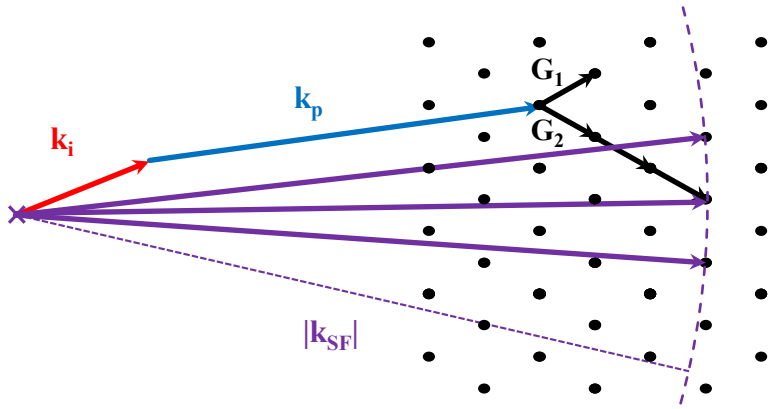

Fig. 3.4 Example of Ewald sphere construction, in a QPM vector diagram, to find phase matching for SFG, driven by the initial waves labelled p and i, in a 2D QPM lattice. $\mathbf{G}_1$ and $\mathbf{G}_2$ are the base RLVs spanning the grid representing the QPM lattice and $\mathbf{k}_i$, $\mathbf{k}_p$, and $\mathbf{k}_{SF}$ are the wave vectors of the waves involved in the SFG.

It is interesting to note that, for certain wavelengths and angles of the initial waves, several points of the grid can be located simultaneously on the Ewald sphere. In such a case of multiple resonances, several SF waves can be generated simultane-

ously in different directions in the plane. This degree of freedom of 2D NPCs is a very promising attribute, due to the phase relations it can bestow upon the multiple generated waves. It is also important to point out that this is a general result; the simultaneous generation of multiple waves is possible for any type of parametric frequency conversion process, not only SFG.

3.3 QPM lattice fabrication

As mentioned earlier, e.g. in section 3.1, QPM can be achieved by alternating the orientation of the nonlinear material, and thus the sign of the second order susceptibility $\chi^{(2)}$ (cf. Eq. (2.3)), every coherence length. This can be achieved using electric-field periodic poling [8, 57], and all QPM devices used in experiments described in this thesis were fabricated with this method. The method is applicable to ferroelectric crystals, such as KTP, $LiNbO_3$ and $LiTaO_3$. A partial volume of such a crystal, where the spontaneous polarisation is uniform is called a (ferroelectric) domain. The method is based on the fact that for ferroelectric crystals the spontaneous polarisation can be reversed locally by applying a local external electric field. A brief account of the method is given here.

An insulating photoresist layer is spin-coated onto a single-domain ferroelectric crystal. The photoresist is exposed by UV light through a photolithographic mask with a periodic pattern to match the coherence length of the intended parametric interaction (cf. sections 3.1.2 and 3.2.2). The exposed photoresist is removed and a layer of metal is evaporated onto the crystal, thus creating periodic contacts to the crystal surface where the photoresist was exposed. A high-voltage external electric field is applied, between the periodic electrodes and a uniform electrode on the crystal backside, in the form of millisecond long pulses. If the field is stronger than the *coercive field* E_C of the ferroelectric crystal, the crystal's spontaneous polarisation is reversed. In $LiTaO_3$ this corresponds to rotating the crystal structure by 180 degrees around the x axis. Since the crystal orientation is defined by the crystal structure, the second order susceptibility also changes sign. The effect is referred to as domain inversion and the ferroelectric domain is said to be switched or inverted.

The domain inversion starts beneath the (edges of the) periodic electrodes and continues through the crystal (along the direction of the applied field, z) but it also extends towards the sides. As a result, the reversed volume grows in depth and laterally for the duration of the application of the external field. The duration is chosen so that the pattern of the periodic electrodes is reproduced throughout the crystal with the desired duty cycle.

The growth speeds in different directions is not necessarily equal. Commonly, a larger growth speed in depth (along z) than laterally (along x or y) permits the high aspect ratios demonstrated for periodic poling [67, 68]. Differences in growth speeds along different directions in the x-y plane, i.e. lateral broadening of the volumes of reversed susceptibility, can also occur. These differences depend on the symmetries of the crystal structure, in other words on which nonlinear material that is being poled [69].

3.4 MgO-doped stoichiometric lithium tantalate

The quadratic nonlinear crystal used in the studies of parametric interactions that are presented in this thesis is 1 mol% magnesium-doped near-stoichiometric $LiTaO_3$ (MgSLT).

$LiTaO_3$ is a member of the crystal family of $LiNbO_3$, with the same perovskite crystal structure, and thus the two isomorphs have many similar qualities. The standard forms of these two crystals are congruent $LiNbO_3$ (CLN) and congruent $LiTaO_3$ (CLT).

The coercive fields for CLN and CLT are high, $E_C \sim 20$ kV/mm, requiring high voltages to periodically pole thick samples and thus hindering the realisation of large aperture crystals. The congruent crystals also suffer from optical damage at shorter (visible) wavelengths, which is of even more concern for optical applications. The optical damage is mostly due to photorefractive sensitivity that gives rise to a wavefront distortion of a laser beam propagating through the material [70] and to green-induced infrared absorption (GRIIRA) [71].

New crystal growth techniques have been developed to produce $LiNbO_3$ and $LiTaO_3$ crystals of modified compositions (nearly stoichiometric and MgO-doped), in order to overcome the limitations for optical applications associated with the relatively low optical damage thresholds and also the elevated poling fields of CLN and CLT. In particular, MgSLT has displayed an extraordinary resistance to photorefractive damage and GRIIRA [20]. There are also indications that MgSLT possesses a relatively high damage threshold to blue-induced infrared absorption (BLIIRA) [72], even though further modification to the composition might be required.

With the demonstrations of good power-handling capabilities even for room-temperature operation, made possible by its reduced photorefraction and high thermal conductivity [73], and high second order nonlinearity MgSLT is a most promising crystal for frequency conversion. The low coercive field of MgSLT, which is somewhat below that of KTP and one order of magnitude lower than that of $LiNbO_3$, also permits up-scaling of device apertures to millimetre sizes [74]. Still, this may require the growth process to mature further, to minimise compositional inhomogeneities that could disturb the periodic poling process.

An important material parameter governing the conversion efficiency of second order parametric interactions is the magnitude of the susceptibility. For QPM in periodically poled crystals it is the d_{33} nonlinear coefficient which is of particular interest, as seen e.g. in Eq. (2.28), since it has the largest magnitude of all the components of the second order susceptibility. There are slight discrepancies among the values of d coefficients reported in literature, because the obtained values depend also on the experimental conditions of the measurement. However, in the same experimental investigation d_{33} was measured for CLT, CLN, MgO-doped CLN and KTP using SHG pumped at 1064 nm [75]. The obtained values were 13.8 pm/V, 25.2 pm/V, 25.0 pm/V and 14.6 pm/V, respectively. The value of d_{33} in MgSLT has later been measured to be slightly higher, 16 pm/V for SHG at 1064 nm [76].

The heat handling capacities of MgSLT are very promising. It exhibits a thermal conductivity which is almost two times that of $LiNbO_3$, 8.8 W/m/K [73] versus

4.6 W/m/K [73, 77]. Also compared to KTP, 3 W/m/K [77], MgSLT possesses a high thermal conductivity.

The transparency range is particularly interesting for QPM crystals, since the choice of points phase matching can be much more freely chosen than for birefringent phase matching. For near-stoichiometric $LiTaO_3$ and MgO-doped CLT the range is 0.27 – 5.5 μm [78, 79], extending further than $LiNbO_3$ on the UV edge (0.3 – 5.5 μm) and further than KTP on both UV and IR edge (0.36 – 4.3 μm) [78].

Owing to the positive properties mentioned here, periodically poled MgSLT is the nonlinear medium that was chosen for the parametric interactions investigated in the frame of this thesis. The next chapter and chapter 5 present my work on the topic of parametric frequency conversion.

Chapter 4

Broadband optical parametric generation

Parametric interactions are highly suitable for optical frequency conversion applications that require high coherence of the generated light. In this chapter I discuss how parametric interactions can provide broad frequency bands available for downconversion. Section 4.1 is devoted to explain my work demonstrating ultrabroad parametric gain bands in the near to mid-IR. The section illustrates the details of broadband optical parametric generation (OPG) in (1D) periodically poled MgSLT (PPMgSLT), based on degenerate downconversion close to the point of zero group velocity dispersion, as discussed in section 2.4.1. An account of the sum frequency generation (SFG) processes, which create dips in the OPG gain spectrum, is also given. Section 4.2 describes an experimental and numerical investigation (numerical work performed by Matteo Conforti) of these SFG processes and how they can be involved in quadratic cascading. It is examined how the cascading can revert the flow of energy, from the SF wavelengths, and instead create peaks in the OPG spectrum. A method, based on pump pulse preshaping, is devised to control the cascading and thus whether dips or peaks appear, resulting in a possibility to obtain smoother gain spectra.

4.1 Broadband parametric downconversion

Broadband parametric gain in the near to mid-IR spectral regions is of interest to a number of applications such as frequency comb generation, spectroscopy and ultrashort optical pulse amplification. Gain bands that can accommodate femtosecond pulses have become a hot topic in recent years. Pulses of this duration are crucial for ultrafast spectroscopy such as femtochemistry [80] and in high harmonic generation (HHG), which produces pulses of attosecond duration. The latter is a field that is now

turning from merely attosecond pulse generation to attosecond spectroscopy [81]. To create the femtosecond pulses, which subsequently pump the HHG, by employing frequency bands in the near IR and at longer wavelengths appears to be favourable because the highest photon energy attainable in the HHG increases with the square of the femtosecond pump wavelength [82, 83]. Another field that can reap benefits from ultrashort pulse amplification is laser ablation, where the use of ultrashort pulses reduces damage to surrounding material and thus increases precision, compared to longer pulses [84, 85]. For ultrashort pulse amplification, parametric conversion processes offer large gain bands, which can yield extremely short pulse durations [37], while reducing the amount of excess heat deposited in the conversion medium compared to laser amplifier media [12, 37, 86]. Access to broadband downconversion regimes is also interesting for frequency comb generation and permits conversion to peripheral wavelength regimes through e.g. difference frequency generation (DFG) [17].

A first possible method to achieve broadband generation in the near to mid-IR spectral regions is to employ a broadband laser [87, 88]. Co^{2+}- and Cr^{2+}-doped gain media offer efficient alternatives where pulses of only several optical cycles can be directly obtained from the laser resonator. However, the maximum gain bandwidth is limited to approximately 1 μm, and is situated between 1.6 and 3.5 μm (depending on dopant species and host material) thus corresponding to approximately 80 THz.

A second method, with which extremely broad bands have been demonstrated, is supercontinuum generation based on a mix of $\chi^{(3)}$ (cubic) parametric interactions such as cascaded stimulated Raman scattering and self-phase modulation, often performed in fibre geometries [89]. Nevertheless, the method offers limited control over the spectral coherence.

In contrast, parametric frequency downconversion in quadratic nonlinear materials provides a high-coherence approach, suitable for the generation and amplification of extremely broad bandwidths of intense radiation. The reduced thermal load of parametric processes is also an advantage for upscaling to higher powers.

By employing non-collinear conversion geometries to realise group-velocity matching (GVM) for the signal and idler pulses, as discussed in section 2.4.1, extremely broad bands have been generated. The broadest bands in the visible and near IR spectral regions, 187 THz 10-dB bandwidth centred at 990 nm and 180 THz at 650 nm, were achieved in β-BaB_2O_4 (BBO) [36, 90]. However, since the method used in experiments employing BBO is based on non-collinear geometry to achieve GVM, it suffers limitations due to transverse walkoff, as described in the first part of section 2.4.1.

To access ultrabroad gain bands in the near IR to mid-IR one can instead exploit the point of zero GVD of the nonlinear material in a collinear conversion geometry to minimise the signal and idler GVDs and increase the bandwidth further, as discussed in section 2.4.1. The dispersion of BBO is such that it cannot offer as broad phase matching in the near IR to mid-IR regime as in the visible to near IR regions [37] and, in addition, BBO starts to absorb beyond 2.5 μm [39]. In a QPM material, one can also reap the benefit of exploiting the largest component of the susceptibility tensor.

The first demonstration of broadband downconversion close to the point of zero GVD in a QPM medium was achieved with orientation-patterned GaAs (OP-GaAs), which displayed a 20 dB OPG bandwidth of 39 THz around 6.6 μm when pumped with 3.1 – 3.3 μm [40]. Periodically poled $KTiOPO_4$ (KTP), $LiNbO_3$ and $LiTaO_3$ can offer alternative QPM solutions, enabling operation with pump wavelengths instead in the near infrared. 10 dB bandwidths of ~150 THz centred at 2.3 μm and ~100 THz at 2.0 μm have been demonstrated for OPG in periodically poled KTP (PPKTP) and periodically poled $LiNbO_3$ (PPLN), pumped at 830 and 930 nm, respectively [41, 43]. Nevertheless, the KTP conversion bandwidths are limited to around 3.5 μm on the long-wavelength side, due to the absorption edge of the material. Such a limitation does not apply to $LiNbO_3$ and $LiTaO_3$ substrates, given their broader transparency range, see section 3.4. On the other hand, these crystals can suffer from effects such as photorefraction and green-induced infrared absorption (GRIIRA) [71], which can compromise their performance at the high powers that are often desired in e.g. ultrashort pulse amplification.

4.1.1 Experimental study of broadband OPG in PPMgSLT

As discussed in section 3.4, MgO-doped near-stoichiometric $LiTaO_3$ has displayed strong resistance against photorefractive effects, GRIIRA and blue-induced infrared absorption (BLIIRA) [20, 72]. This, the material's heat-handling capacities [73] and the possibility for aperture scaling [74] make the material particularly promising for high power applications. Also, using the collinear method of broadband phase matching in vicinity of the point of zero GVD, the dispersion of MgSLT grants large bandwidths. A numerical comparison of nonlinear materials capable of collinear group velocity matching in downconversion to the vicinity of the point of zero GVD is found in Ref. [32]. In particular, when pumping downconversion processes in MgSLT in the wavelengths of Ti:sapphire sources, degenerate downconversion brings the working point close to the point of zero GVD, estimated to lie at $\lambda_{s,i} \sim 1820$ nm using Sellmeier equations of Ref. [21]. Ti:sapphire systems are also suitable as pump sources for the investigation owing to their broad wavelength tunability range, permitting a systematic mapping of the pump wavelength dependence, and their possibility to provide high peak intensity pulses.

The samples used in the experiments were in-house periodically poled (the poling was performed by Katia Gallo), starting from commercially available 0.5 mm thick *z*-cut crystals of MgSLT. Three 1-cm-long QPM lattice periods, $\Lambda = 25$, 26 and 27 μm, were implemented in order to systematically investigate the spectral location of the broadest OPG bands. The three different QPM structures were created side-by-side in each crystal sample, as 2 mm wide strips, to be able to investigate all the different periods in the very same crystal sample. The OPG process was pumped by an amplified tunable picosecond Ti:sapphire system, fixed at 1 kHz repetition rate. The pulse duration was adjustable by varying the group delay introduced in the compressor of the Ti:sapphire amplifier. As a result the pump pulse duration could be altered in the range of 1 – 70 ps. The pump wave was polarised along the *z* axis of the MgSLT crystal, ensured by the pump intensity attenuation system consisting of a half

wave plate and a polarising beam splitter cube. Using pump wavelengths from 820 to 900 nm the full spectral response of the three lattice structures was mapped. The optical output was focused into a fibre-coupled optical spectrum analyser (OSA, Ando AQ6315A), which was sensitive up to 1750 nm, to record the OPG signal contents. Owing to the fibre-coupling the OSA was the most flexible and thus most frequently used detector for spectra, though to extend the characterisation to the full OPG response, up to the mid-IR wavelengths, a second detector arm was set up. In this, a free-space coupled scanning Horiba Jobin Yvon (iHR550) monochromator equipped with a PbSe detector head which, used with a lock-in amplifier, was sensitive up to 4.8 μm. The collinear experimental configuration is shown in Fig. 4.1.

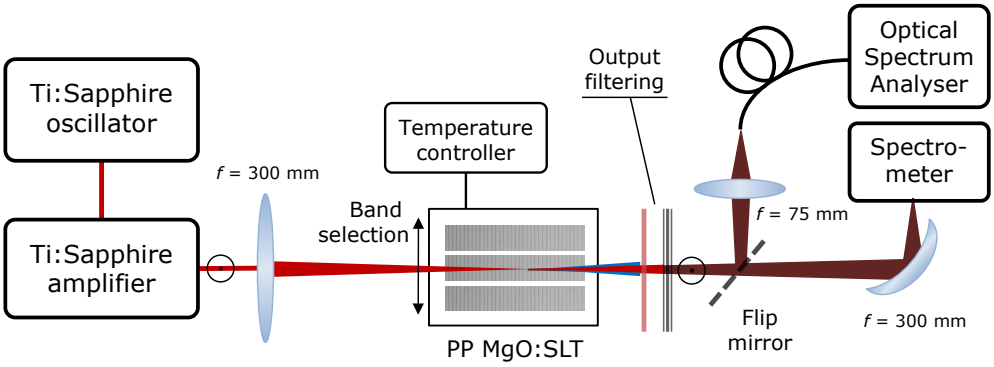

Fig. 4.1 Sketch of the setup used for the OPG experiments. The OPG pump was a Ti:sapphire amplified laser system delivering Gaussian μJ-pulses, with durations adjustable in the picosecond regime at 1 kHz. The input beam was loosely focused by a 300 mm lens into the PPMgSLT crystal, heated to 80°C. The OPG output was fibre-coupled to an optical spectrum analyser. Spectral measurements extending beyond 1.75 μm were performed with a free-space coupled spectrometer based on a Horiba Jobin Yvon (iHR550) scanning monochromator.

Out of the three lattice structures, investigated for the pump wavelengths stated above, the broadest generated OPG spectra were achieved using the 25 and the 26 μm lattice periods. The broadest spectrum measured 185 THz at 10 dB bandwidth, reaching from 1130 to 3730 nm, thus spanning more than one optical octave. The full spectral mapping of the OPG signal output, using the OSA, of 25 and 26 μm periods is presented in Fig. 4.2. In order make comparable measurements at the different pump wavelengths, the spectra were recorded with a pump intensity of 1.6 times the OPG threshold. The threshold was defined as the pump intensity for which the parametric generation could be observed on an IR detection card (Thorlabs VRC2, sensitivity range: 800 – 1700 nm), corresponding to around ~0.5 μJ per generated pulse. This corresponded to pump peak intensities in the interval of 6 – 18 GW/cm^2, depending on the pump wavelength. For the mapping of the OPG signal response across the full wavelength span of the pump, i.e. the data of Fig. 4.2, the pump pulses duration was kept constant at 1.5 ps and the beam radius at 230 μm (1/e^2).

A resolution for the mapping the pump spectral range of 5 nm was chosen, since a higher resolution would not bring much additional information on the whereabouts of the working point giving the broadest bands, due to the slowly varying dispersion in the proximity of the zero-GVD point. Indeed, the broadest bands for each

QPM period could not be determined with a lower uncertainty than 5 - 10 nm in the pump wavelength. The broadest bands are generated at pump wavelengths shorter than the predicted pump wavelength for zero-GVD in MgSLT ($\lambda_p = 910$ nm, using Sellmeier equations of Ref. [21]). The experimental shift towards shorter wavelengths is consistent with similar observations in other materials [41]. Furthermore, one also notes that the Sellmeier equations predict phase matching at slightly shorter pump wavelengths than recorded experimentally. This is plausibly due to the predictions being more sensitive to errors in the Sellmeier equations when the GVD is close to zero.

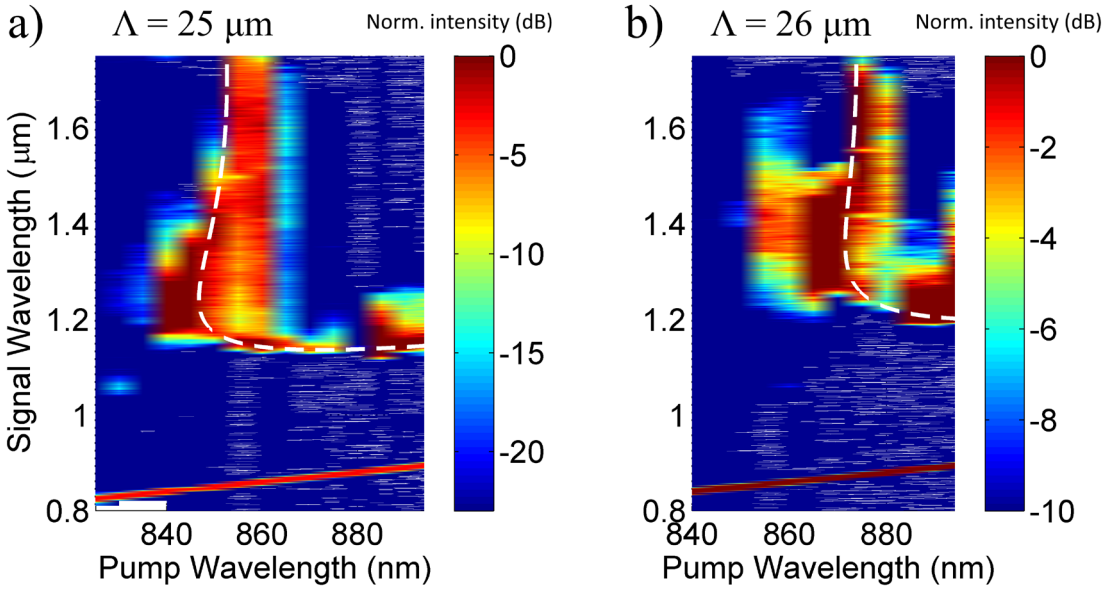

Fig. 4.2 Broadband optical parametric generation in 1D PPMgSLT pumped in the Ti:sapphire wavelength range (horizontal scale) using QPM of lattice periods a) 25 μm and b) 26 μm. The pump peak intensities were kept at 1.6 times above the OPG threshold (defined in the text), corresponding to an interval of 6 - 18 GW/cm^2. At the output of the crystal, the pump was attenuated by a dichroic mirror, but can still be distinguished as an oblique red line in the lower parts of the plots. The OPG signal wavelengths, recorded with an optical spectrum analyser, are denoted vertically, a logarithmic colour scale indicating the recorded intensities. Each OPG signal recording is normalised to the pump peak power. The dashed white curves are predictions for perfect phase matching, calculated using Ref. [21].

The full OPG band at the point of broadest phase matching for $\Lambda = 25$ μm, recorded with the scanning monochromator and its PbSe detector, is displayed in Fig. 4.3. A higher pump peak intensity (90 GW/cm^2) was chosen to ensure that the entire OPG band, i.e. all signal and idler wavelengths, could be detected with minimal background noise. The pump beam was also focused more tightly, to 100 μm radius. The other experimental parameters that were altered, as compared to the OPG signal mapping, are stated in the caption of Fig. 4.3. The recorded OPG intensities (blue solid curve) have been corrected for absorption in the optical elements between the PPMgSLT crystal and the detector, before being plotted.

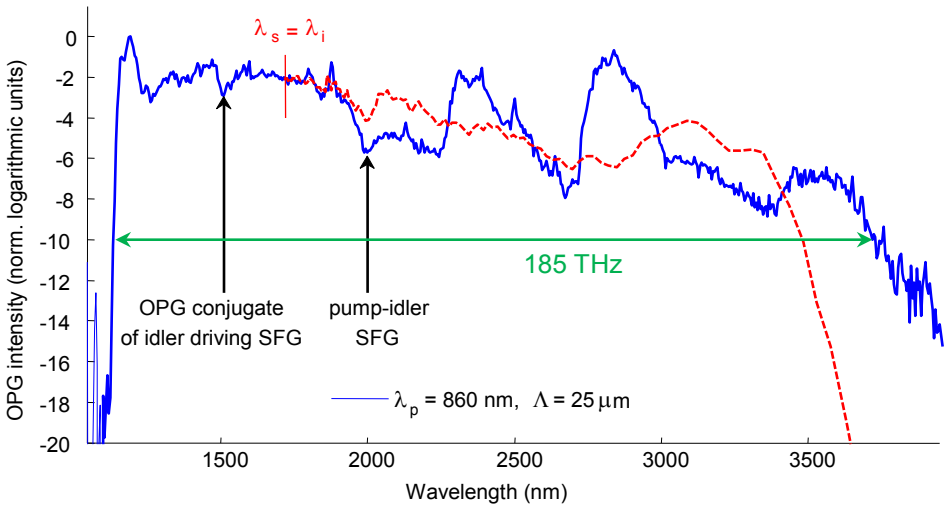

Fig. 4.3 OPG signal spectrum from 1D PPMgSLT, generated with 25 μm period using a pump wave of 860 nm, 90 GW/cm^2 peak intensity and 2.7 ps pulse duration focused to 100 μm beam radius. The dashed red curve represents a prediction of the idler intensities, calculated from the detected signal intensities using the Manley-Rowe relations, Eq. (2.22).

Fig. 4.3 also includes a prediction of the idler spectrum (red dashed curve), calculated from the signal intensities ($\lambda_s < 2\lambda_p$) by using the Manley-Rowe relations, Eq. (2.22). It is seen that the recorded OPG idler intensities deviate from this Manley-Rowe prediction. As a result of continued investigations of the broadband OPG in PPMgSLT, it is concluded that the bulges at 2.4 μm and 2.8 μm were measurement artifacts, not related to vibrational resonances as originally thought. The bulge at 2.4 μm was the second order (of the diffraction from the grating in the monochromator) of the signal peak at 1.2 μm. The bulge at 2.8 μm was associated with the second diffraction order of the small shoulder on the shorter wavelength side of the dip at 1.5 μm. (The dip is marked in Fig. 4.3 and discussed in detail below, its position in the OPG spectrum referred to as $\lambda_{2*} = 1.5$ μm.) The second diffraction order of this shoulder was amplified by the corrections that compensate for absorption of infrared wavelengths in the optical elements, thus creating the bulge at 2.8 μm.

The discrepancy, between the recorded idler intensities (blue solid curve) and the Manley-Rowe prediction (red dashed curve), at the long wavelength edge of the OPG gain band was due to the responsivity of the PbSe detector falling significantly already at 1150 nm. Comparing with an OSA measurement (recorded with an InGaAs detector) at the same pump wavelength, displayed in Fig. 4.4, the shorter wavelength edge of the OPG spectrum extended to 1130 nm. In the Manley-Rowe prediction an edge at 1150 nm translates into a decrease in predicted intensities at 3.4 μm, seen in Fig. 4.3. The true decrease of the predictions, i.e. based on the edge of 1130 nm of the more accurate OSA measurements, should occur first at 3.6 μm, which correlates better with the recorded intensities in Fig. 4.3. Accordingly, the broad and low bulge at 3.6 μm in Fig. 4.3, initially speculated to be the overtone of a vibrational resonance (cf. article I), is in fact part of the OPG. The spectral extent of the OPG is thus well described by the spectral extent of the recorded intensities. Accordingly, the correct

bandwidth at 10 dB is 185 THz, i.e. more than octave-spanning and the broadest band achieved so far in collinear parametric downconversion.

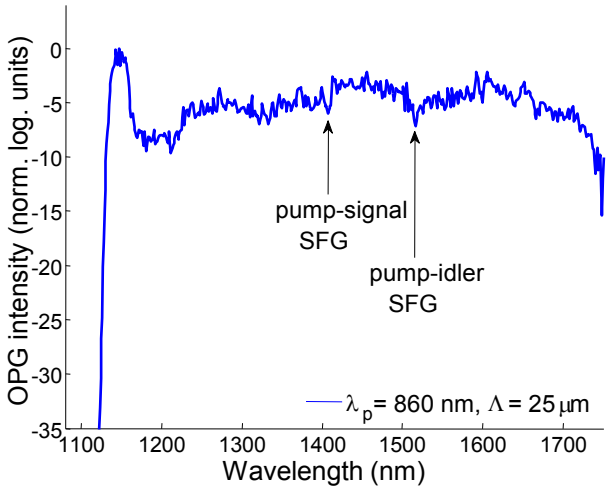

Fig. 4.4 OPG signals from 1D PPMgSLT, generated with 25 μm period using a pump at 860 nm, 6 GW/cm^2 peak intensity and 1.5 ps pulse duration focused to 230 μm beam radius. This spectrum corresponds to a vertical slice at 860 nm pump wavelength of the data in Fig. 4.2a.

Given the octave-spanning band, the likelihood of the QPM lattice supporting a higher order QPM resonance, that phase matches a wavelength within the band for parasitic upconversion, is quite high. Indeed, in the spectra reported for broadband OPG in PPKTP and PPLN higher QPM order SFG processes, between pump and OPG wavelengths, carve significant dips in the frequency spectra [41, 43]. Also in the case of broadband OPG in PPMgSLT presesnted here, the impact of higher order QPM SFG processes is apparent e.g. in Fig. 4.3.

The SFG occurs in cascade to the OPG. The OPG pump wave and a signal/idler wave at a particular wavelength $\lambda_{s,i}$ generate light at the SF wavelength $\lambda_{SF} = \lambda_{s,i}\lambda_p/(\lambda_{s,i} + \lambda_p)$. The effect on the OPG spectrum is a dip at $\lambda_{s,i}$. Additionally, a dip also appears at the OPG conjugate wavelength $\lambda_{(s,i)^*} = \lambda_{s,i}\lambda_p/(\lambda_{s,i} - \lambda_p)$, due to a reduced seeding of the OPG at the SFG resonance $\lambda_{s,i}$.

Specifically, in the PPMgSLT experiments, there were two SFG processes taking place subsequent to the OPG, marked by arrows in Fig. 4.3. The pump wave and a signal wave at $\lambda_1 = 1.4$ μm generated SF light at 533 nm through 3rd order QPM, while the pump wave and an idler wave at $\lambda_2 = 2.0$ μm generated SF light at 598 nm through 2nd order QPM. The latter SFG resonance can be seen in the OPG spectrum as a dip at the OPG conjugate $\lambda_{2*} = 1.5$ μm.

Included in the work presented in this thesis is also a study of the SFG features that arise in broadband OPG. The second part of this chapter is devoted to explaining the findings of this study. It is demonstrated that through the pump pulse duration one can control quadratic cascading effects of the SFG. Given that the broadband downconversion spectra are likely to be disturbed by one or several SFG processes, as seen above, it is desirable to reduce their impact. In the conclusion of the study pre-

sented in the next section, a method to minimise the impact of the SFG processes and bring upconverted light, from the SF wavelengths, back to the broadband OPG spectrum is suggested. To appreciate the study, however, one first needs to review some basic principles of quadratic cascading in the pulsed regime.

4.2 Quadratic cascading in the pulsed regime

In the pulsed regime quadratic cascading can be initiated in spite of the chosen working point being situated at perfect phase matching, i.e. $\Delta k = 0$. This can be explained by the fact that the optical pulses driving the parametric conversion process have non-zero spectral bandwidth $\Delta\omega$ (quasi-monochromatic approximation), given their finite pulse duration. In other words, even though the carrier frequency ω_0 is situated at perfect phase matching, the bandwidth of the pulse may extend outside of the acceptance bandwidth of the phase matched working point. The case is exemplified by the dashed vertical line of Fig. 4.5a, where the green curve describes the acceptance bandwidth for the second harmonic generation (SHG) process calculated with Eq. (2.24). It is then possible for $\chi^{(2)}$ cascading to be initiated owing to the frequencies at the edges of the pulse bandwidth, since they experience a non-zero phase mismatch, $\Delta k \neq 0$, cf. section 2.5.

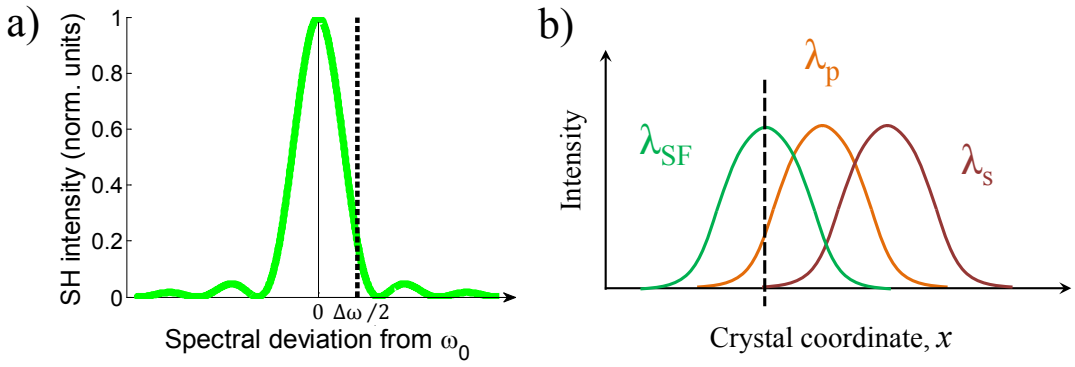

Fig. 4.5 a) Tuning curve of SHG: Normalised SH intensity as function of frequency deviation, calculated with Eq. (2.24). An example deviation of $\Delta\omega/2$ is marked, corresponding to the extreme frequency of a bandwidth of $\Delta\omega$. b) Sketch of the temporal walkoff between the initial pulses (pump at λ_p and signal at λ_s) and the SF pulse at λ_{SF}. Local depletion of the signal pulse is marked. The vertical dimension represents a normalised intensity scale.

To account for the bandwidth of the pulse the phase mismatch Δk is expanded in a Taylor series around the working point (in a similar manner to approach taken for broadband OPG in section 2.4). In a (non-degenerate) three-wave mixing process the bandwidths of both initial waves must be taken into account, i.e. the phase mismatch must be expanded with respect to the frequencies of both the waves. Taking the example of the signal-and-pump driven SFG following broadband OPG in PPMgSLT, discussed in section 4.1.1, the phase mismatch must be expanded with respect to the

pump frequency ω_p and the signal frequency ω_s. By letting the pump frequency vary and keeping the signal frequency fixed the following dependence is obtained.

$$\Delta k\left(\omega_{0,p}+\Delta\omega_p\right)=k_{SF}-k_p-k_s+\left(\frac{\partial k_{SF}}{\partial\omega_{SF}}-\frac{\partial k_p}{\partial\omega_p}\right)\Delta\omega_p+O\left(\Delta\omega_p\right)^2 \tag{4.1}$$

Analogously, the signal frequency is varied keeping the pump frequency fixed, giving:

$$\Delta k\left(\omega_{0,s}+\Delta\omega_s\right)=k_{SF}-k_p-k_s+\left(\frac{\partial k_{SF}}{\partial\omega_{SF}}-\frac{\partial k_s}{\partial\omega_s}\right)\Delta\omega_s+O(\Delta\omega_s)^2 \tag{4.2}$$

The second order terms are neglected, since they become important only once the sum of the first order terms approach zero or if the bandwidth of the pulses are very large (which can be the case for e.g. femtosecond pulses, but not for the OPG experiments described here). Assuming that the working point, around which the expansion is made, is phase matched the zeroth order terms cancel. The derivatives in the first order terms can be expressed using the group velocities, $v_g=\partial\omega/\partial k$, of the SF, pump and signal waves, giving

$$\Delta k\left(\omega_{0,p}+\Delta\omega_p\right)=\left(\frac{1}{v_{gSF}}-\frac{1}{v_{gp}}\right)\Delta\omega_p+O\left(\Delta\omega_p\right)^2 \tag{4.3}$$

for the pump frequency expansion and

$$\Delta k\left(\omega_{0,s}+\Delta\omega_s\right)=\left(\frac{1}{v_{gSF}}-\frac{1}{v_{gs}}\right)\Delta\omega_s+O(\Delta\omega_s)^2 \tag{4.4}$$

for the signal frequency expansion.

It is seen that if $\Delta\omega_p\neq 0$ or $\Delta\omega_s\neq 0$, which is the case for pulsed inputs, the effective phase mismatch can still be non-zero, provided that there is a group velocity mismatch between the SF and the pump or signal waves. If the group velocity mismatch of any of the waves is sufficiently large to extend beyond the acceptance bandwidth, there will be a part of the incident intensity that will drive a non-phase matched conversion. If the conversion is sustained long enough (cf. section 2.5), this will incur quadratic cascading.

The characteristics of quadratic cascading in the pulsed regime can also be viewed from a temporal domain perspective. As pointed out in section 2.5, in order for quadratic cascading at perfect phase matching, $\Delta k=0$, to start there must be an imbalance in intensity (or more precisely in photon fluxes) among the two initial waves. However, it is sufficient for the imbalance to arise locally as is explained below.

In the signal-and-pump driven SFG process taken as example, there is group velocity mismatch between the three pulses involved, the signal pulse propagating with the highest velocity and the SF pulse at the lowest. If the pulses propagate long enough in the nonlinear material the spatial overlap will be significantly reduced and locally the signal pulse will be depleted, as indicated in Fig. 4.5b by the vertical dashed black line. Locally, the situation is qualitatively similar to the point of the plot

in Fig. 2.9a where the dashed red curve reaches zero intensity. As explained in section 2.5, the only wave experiencing a non-zero driving term at this point is the wave which was just depleted. It is thus regenerated but with a phase shift of π radians compared to the light that had just been exhausted. The phase shift of π causes a change of direction of the energy flow, i.e. a part of the SF wave starts to be downconverted back to the two initial waves, thus completing a quadratic cascading up- and downconversion cycle.

As was seen in section 2.5, altering the initial intensities of the signal and pump waves can control whether quadratic cascading occurs. However, in practice the initial intensities are difficult to adjust, since the SFG is a cascaded process and the intensities of the signal and pump waves are directly dependent on the preceding OPG process. The cascading can also be initiated, as explained above, by changing the group velocities of the involved waves or the length of the nonlinear material to control whether the conversion process is sustained long enough for the pulses to walk off and loose spatial overlap. These parameters, though, are often fixed in an experiment. A more flexible approach to control the cascading would instead be through the pulse durations. If the involved pulses have a long duration the spatial overlap is maintained despite the group velocity mismatch, but if the pulses are short the spatial overlap is lost and $\chi^{(2)}$ cascading is initiated. This was investigated, both experimentally and numerically, by altering the pump pulse duration and studying the optical response of the broadband OPG and cascaded SFG processes, as described in the continuation of this section.

The "intuitive" models in both the frequency and the temporal domains, discussed above, only give a qualitative understanding of which interaction parameters that can trigger cascading. For a full description of cascading in the pulsed regime the situation becomes much more complicated and a numerical approach is needed, e.g. by solving the equations for the explicit local evolution of the amplitudes and the phases of the involved waves [91].

4.2.1 Experimental demonstration of temporally-initiated quadratic cascading

Returning to the experimental case of the two SFG processes, driven by the pump wave and by the aforementioned (cf. section 4.1.1) signal ($\lambda_1 = 1.4$ μm) and idler ($\lambda_2 = 2.0$ μm) waves in the OPG broadband spectrum. The measurements performed in the condition of e.g. Fig. 4.3 are in the regime where energy is upconverted from the OPG wavelengths, hence the dips. The intention of the study of the SFG processes, which is explained in this section, was to investigate the control of quadratic cascading through the pump pulse duration. The study was carried out by recording the full OPG spectrum for a range of pump pulse durations, while keeping the pump peak intensity constant in order to avoid any variation due to peak intensity changes of the pump (and signal) waves. Typical results, illustrating the conclusion of the study, are presented in Fig. 4.6. Besides my work, the investigations on SFG cascading subsequent to broadband OPG in PPMgSLT involved numerical simulations performed by

Matteo Conforti (Univ. of Brescia), used in a comparison/interpretation of the experimental findings. .

Fig. 4.6 shows the broadband OPG in PPMgSLT generated with moderate pump peak intensities, 6 GW/cm^2, 100 μm pump beam radius, at two different pump pulse durations. The other experimental conditions were as described in Fig. 4.1. The red curve in Fig. 4.6 is the OPG spectrum generated with 6.1 ps pump. The SFG resonance driven by the pump wave and the idler wave at $\lambda_2 = 2.0$ μm, marked in the figure as λ_2, is seen clearly as a dip in the recorded spectrum. It is accompanied by a dip at the signal wavelength $\lambda_{2*} = 1.5$ μm, marked in the figure as λ_{2*}, which is the OPG conjugate of the 2.0 μm idler wavelength ($\lambda_{2^*} = \lambda_2\lambda_p/(\lambda_2 - \lambda_p)$). The other SFG resonance is driven by the pump wave and the signal wave at $\lambda_1 = 1.4$ μm, affecting the OPG gain at $\lambda_1$and at its idler conjugate $\lambda_{1*} = 2.2$ μm, both exhibiting gain dips, marked λ_1 and λ_{1*}, respectively, in Fig. 4.6.

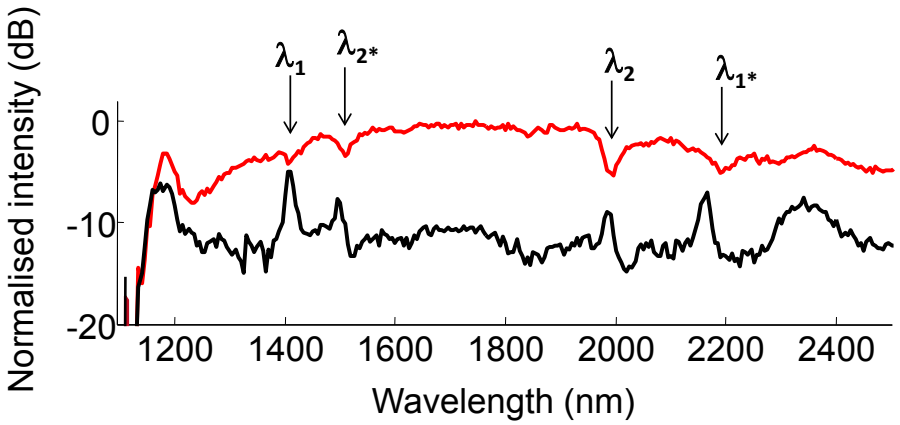

Fig. 4.6 Near IR part of broadband OPG bands generated in 1-cm-long 1D PPMgSLT of 25 μm QPM period using a pump beam of 860 nm, 6 GW/cm^2 peak intensity, focused to 100 μm radius. Each point of the spectra is an average of 900 pulses. The pump pulse durations were 6.1 ps (red curve) and 1.7 ps (black curve).

Pumping with significantly shorter pulses, 1.7 ps, (black curve in Fig. 4.6) changes completely the characteristics of the very same SFG resonances in the OPG spectrum. A gain enhancement now appears at the spectral locations of the SFG resonances. This is the signature of a change in the direction of energy flow in a first cycle of quadratic cascading, i.e. the sum frequency (SF) wave is backconverted to the OPG band. In other words, the process is now carried out in a pump regime initiating quadratic cascading.

To explain how the $\chi^{(2)}$ cascading arises, the SFG resonance involving the idler wave at $\lambda_2 = 2.0$ μm is chosen as example. The course of events is completely analogous for the SFG resonance involving the signal wave at $\lambda_1 = 1.4$ μm.

After the idler wave has been generated, the higher order phase matched conversion to the SF wavelength commences and the SF intensity grows. The SFG creates dips in the gain spectrum, as seen in the red curve of Fig. 4.6. The combination of

the broadband OPG and cascaded SFG is schematically illustrated in Fig. 4.7a, the red arrow indicating the SFG.

In a first approximation the triggering of SFG cascading can be explained by the temporal walkoff between the idler and the pump and SF pulses, as discussed in the previous section. If the pulses were allowed to continue propagating through the nonlinear material after the SF wave has been generated, the temporal walkoff of the idler pulse would cause it to speed ahead of the other two pulses. Eventually the idler pulse would lose spatial overlap so that at a local point in space only the SF and the pump waves would have non-zero intensities. The situation in sketched in Fig. 4.7b and the local point in space is marked by a vertical, dashed black line. As explained in the previous section, at this point in space a backconversion of energy from the SF to the OPG band and to the pump is initiated, constituting the first cycle of a quadratic cascading process, building a peak on top of the OPG spectrum. In Fig. 4.7a, the (cascading) backconversion is indicated by the black arrow.

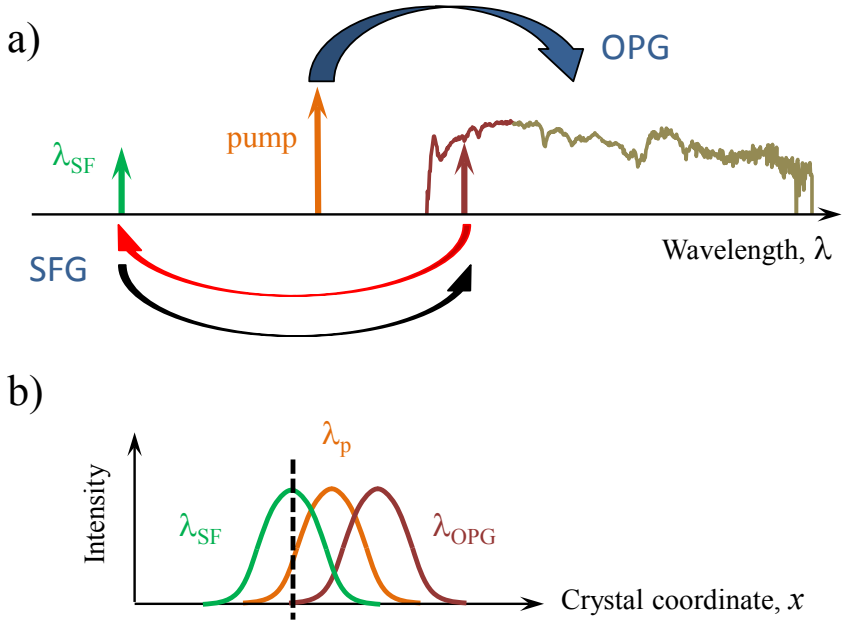

Fig. 4.7 a) Illustration of the SFG cascading subsequent to broadband OPG. The red arrow signifies upconversion through SFG and the black arrow the backconversion of the SF wave to the OPG band, which constitutes the first cycle of a quadratic cascading. b) Sketch of the temporal walkoff of the idler (or signal) pulse with respect to the SF and pump pulses. The vertical dimension represents a normalised intensity scale.

The temporal walkoff becomes more pronounced when shortening the pulse durations, since the pulses then more rapidly lose their spatial overlap. As a result, the backconversion of the SF wave can be seen in the spectrum recorded with the shorter pulse duration (black curve in Fig. 4.6), but not with the longer pulse duration (red curve). The spectrum recorded with longer pulse duration instead exhibits the SFG dips generally encountered in similar experiments, since the pulses are too long to lose overlap over the propagation length of the crystal.

In other words, it is shown that the pump pulse duration can determine whether quadratic cascading is initiated for the SFG processes. It also becomes evident that an intermediate pump pulse duration could be found, for which the impact of the SFG resonances, peak or dips, in the broadband OPG spectrum could be minimised, though plausibly not removed completely. Nevertheless, the pump pulse duration would present a flexible method to improve the flatness of the generated spectrum, which is important e.g. for applications where the QPM device is operated as an optical parametric amplifier (OPA).

Although the qualitative explanation of the triggering of quadratic cascading through e.g. local loss of spatial overlap, which is given above, is helpful to gain a physical insight in the phenomena, the description is a simplification. Quadratic cascading in the pulsed domain depends on an intricate combination of local amplitude variations (at each point in time throughout the propagation), group velocity mismatch and phase relationships between the involved waves. Quantitative simulations of the evolution of the pulses are required to take all parameters into account. The following section describes the systematic numerical analysis that has been performed to model theoretically both the broadband OPG and subsequent SFG.

4.2.2 Numerical simulations of OPG and cascading effects

A collaboration with researchers at the University of Brescia (Matteo Conforti and Fabio Baronio) who had developed a unique model capable of dealing with ultra-broadband OPG in $\chi^{(2)}$ media, was initiated. The following numerical simulations have been performed by Matteo Conforti.

When simulating second order parametric interactions the usual approach (used in chapter 2) is to write the coupled wave equations for spectrally separated waves at the wavelengths which are involved in the interactions, as in Eqs. (2.20) [7]. However, this approximation applies only to quasi-monochromatic waves. In the case of ultra-broadband interactions, e.g. when the spectral bands merge and overlap, the method is not well-suited to predict the full behaviour of the involved waves. Conforti et al. approached the issue and demonstrated in 2010 that ultra-broadband second order parametric interactions can be described by a single-wave envelope equation [92].

In contrast to applying the slowly varying envelope approximation (SVEA), care is taken when deriving the nonlinear propagation equation for the electric field, not to impose any requirement on the bandwidth of the pulses. This is handled both in the approximations applied to the nonlinear wave equation, explained further in Ref. [93], and in the definition of the complex envelope employed for the single wave [92]. In plane wave geometries, with no dependence in the transverse coordinates, the resulting single-wave envelope equation is the following.

$$\frac{dA}{dx} + iDA = -\frac{i\chi^{(2)}\omega_0^2}{4\beta_0\, c^2}\left(1 - \frac{i}{\omega_0}\frac{\partial}{\partial\tau}\right)\left[A^2 e^{i\phi} + 2|A|^2 e^{-i\phi}\right] \tag{4.5}$$

$A(x,\tau)$ is the broadband complex electric field envelope at a reference frequency ω_0, $\phi(x,\tau) = i\omega_0\tau - i\left(\beta_0 - \omega_0/v_g\right)x$ and $\beta_0 = \mathrm{Re}[k(\omega_0)]$, where $k(\omega) =$

$(\omega/c)\sqrt{1+\chi^{(1)}(\omega)}$ is the propagation constant and v_g is the group velocity at the reference frequency. The linear part of the susceptibility $\chi^{(1)}$ varies as a function of frequency, while the second order susceptibility $\chi^{(2)}$ is assumed to be constant, which is reasonable when working far from absorption as discussed in section 2.1. $D = \sum_{m=2}^{\infty} \frac{1}{m!} k_m \left(-i\frac{\partial}{\partial t}\right)^m$ is the dispersion operator, where $k_m = \frac{\partial^m k}{\partial \omega^m}(\omega_0)$, and $\tau = t - x/v_g$ is the coordinate system moving with the reference group velocity.

The single-wave envelope equation includes all possible second order parametric processes that could occur. Consequently, the method can capture the interplay during propagation of the broadband OPG and the cascaded SFG processes in the experiments described in this chapter, taking into account group velocity mismatch, phase relationships, etc.

Numerical simulations of the broadband OPG response in PPMgSLT were performed for 25 μm QPM period with a pump beam of 860 nm, investigating the range of 0.5-30 ps pump pulse durations and 1-10 GW/cm^2 peak intensities. The OPG response was statistically evaluated over an ensemble of multiple (typically 30) simulations, performed with different random noise seeds. The key results of the simulations are shown in Fig. 4.8, by displaying the OPG response at two different pulse durations. The upper plots of both a) and b) show the broadband OPG spectra for two different pump pulse durations at the output of the PPMgSLT crystal. The 2D colour maps illustrate the spectral evolution during the propagation along x through the crystal.

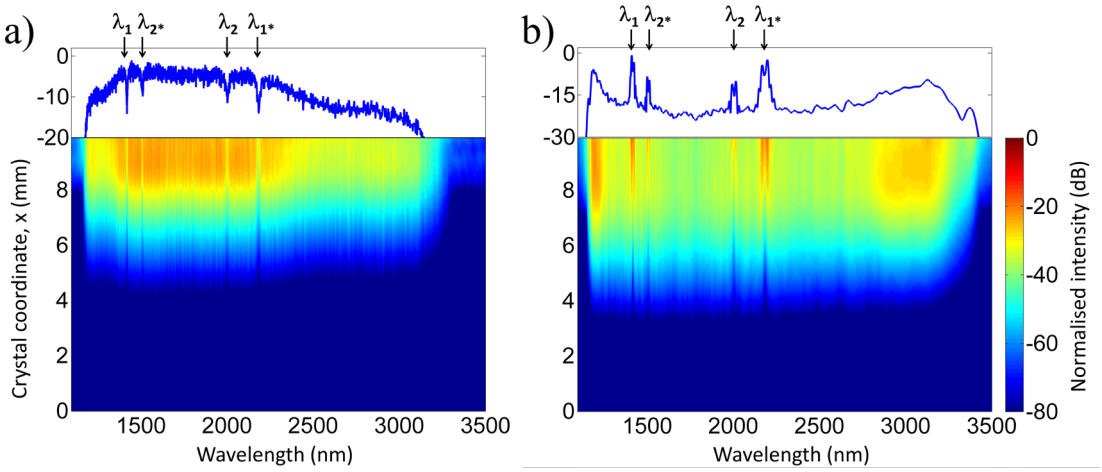

Fig. 4.8 Simulated broadband OPG response of a 1cm-long PPMgSLT crystal in the presence of cascaded processes, using a Gaussian pump at 860 nm. Output OPG spectra (1D plots) and evolution inside the crystal of the generated intensities (2D colour maps) are shown in logarithmic scale. Pump pulse durations: a) 10 ps and b) 0.7 ps. Pump peak intensities: a) 7 GW/cm^2 and b) 15 GW/cm^2. Numerical solutions of Eq. (4.5), averaged over 30 realizations.

The simulations confirm the experimental results and strengthen the intuitive explanation of walk-off-triggered quadratic cascading. The SFG resonances and their OPG conjugates at 1.4, 1.5, 2.0, and 2.2 μm, highlighted by arrows, manifest as dips in the gain spectrum in the case of the 10 ps pump, Fig. 4.8a. In contrast, when the pump pulse duration is decreased, the walk-off among the waves involved in the SFG

process (pump, signal/idler and SF) increases. Accordingly, as these components lose their overlap during propagation, the SF wave begins to backconvert to the pump and signal/idler waves, yielding a re-enhancement of the OPG output, seen as peaks in Fig. 4.8b. The backconversion is the signature of the onset of the SFG quadratic cascading as discussed above. Comparing the numerical simulations of Fig. 4.8 with the experimental results, presented in Fig. 4.6, the same qualitative behaviour of the SFG features, dips and peaks, is identified in the OPG spectra. The two regimes of the SFG features display the same dependence on the pump pulse duration for both experimental and numerical results, with the transition between the two regimes occurring at approximately the same values. Being able to predict the behaviour of the SFG resonances in the OPG spectrum by using a model based on $\chi^{(2)}$ parametric interactions strongly corroborates the intuitive explanation of $\chi^{(2)}$ SFG cascading given before.

Chapter 5

Coupled OPG in 2D QPM lattices

Systematic experimental and numerical investigations on coupled OPG in 2D QPM lattices are the topics of this chapter. In general, downconversion in 2D QPM lattices, also referred to as 2D nonlinear photonic crystals (NPCs), is a relatively unexplored field. The greater part of the experiments performed using 2D QPM lattices has been focusing on upconversion, as described in section 3.2. In section 3.2, it was also presented how 2D NPCs, compared to 1D QPM structures, grant new degrees of freedom for engineering spectrally and spatially the response of a conversion process. In this chapter those degrees of freedom are investigated in downconversion.

The first part of this chapter describes the work I performed, in the frame of the thesis, to demonstrate and investigate experimentally the behaviour of coupled OPG in hexagonal QPM lattices, complemented by numerical predictions of the ensemble of QPM working points for coupled OPG in the NPC lattices. Both the spectral and angular characteristics of the coupled OPG output have been documented, together with their dependence on the wavelength (section 5.1) and propagation angle (section 5.2) of the pump wave.

The second part of this chapter (section 5.3) treats my investigation of *cascaded* sum frequency generation (SFG) subsequent to the coupled OPG, and concerns both experiments and numerical modelling. The initial waves driving the SFG were the pump wave and either a signal or an idler wave, which is conceptually similar to the OPG and SFG processes in 1D periodically poled MgSLT described in chapter 4.

5.1 Coupled optical parametric generation

Coupled OPG, as defined in this thesis, necessitates two simultaneous OPG processes, phase matched by the same 2D QPM lattice but different RLVs (reciprocal lattice vectors), whose signal (or idler, but this will be discussed somewhat later) waves are

spectrally and spatially degenerate. In other words, the signal waves are indistinguishable and thus become one wave, shared by both the two OPG processes. Consequently, the parametric processes experience a coherent exchange owing to this *shared signal* beam, which also gives rise to *twin-beam* idler waves that are spectrally degenerate but propagate at different angles. The twin-beam OPG output has no counterpart in 1D QPM, since the two twin-beams preserve their spectral degeneracy throughout a tuning of the pump input angle. The coherent coupling between the parametric processes results in well-defined phase relations between the generated waves of two the processes and, in particular, entanglement of the twin-beam photons.

The theoretical description of coupled OPG can be derived by starting from the general case of two separate OPG processes, each supported by one of the two base RLVs of a 2D QPM lattice, denoted by the indices 1 and 2. The conditions of momentum conservation (based on the non-collinear phase mismatch relation (3.29))

$$\begin{aligned} \mathbf{k}_p - \mathbf{G}_1 &= \mathbf{k}_{s,1} + \mathbf{k}_{i,1} \\ \mathbf{k}_p - \mathbf{G}_2 &= \mathbf{k}_{s,2} + \mathbf{k}_{i,2} \end{aligned} \tag{5.1}$$

and of energy conservation

$$\begin{aligned} {\lambda_p}^{-1} &= {\lambda_{s,1}}^{-1} + {\lambda_{i,1}}^{-1} \\ {\lambda_p}^{-1} &= {\lambda_{s,2}}^{-1} + {\lambda_{i,2}}^{-1}, \end{aligned} \tag{5.2}$$

allow an infinite set of OPG solutions, for a given pump wavelength and input angle. For instance, if the wavelengths of the generated waves are slightly altered, the conversion can still be phase matched by adjusting the propagation angles of the waves. Fig. 5.1a illustrates a QPM vector diagram of two arbitrary OPG processes, describing the wave vectors involved in the conversion processes and the hexagonal lattice supporting the processes. The base RLVs that phase match the interaction are $\mathbf{G}_1$ and $\mathbf{G}_2$. Further details of the lattice geometry were presented in section 3.2.1.

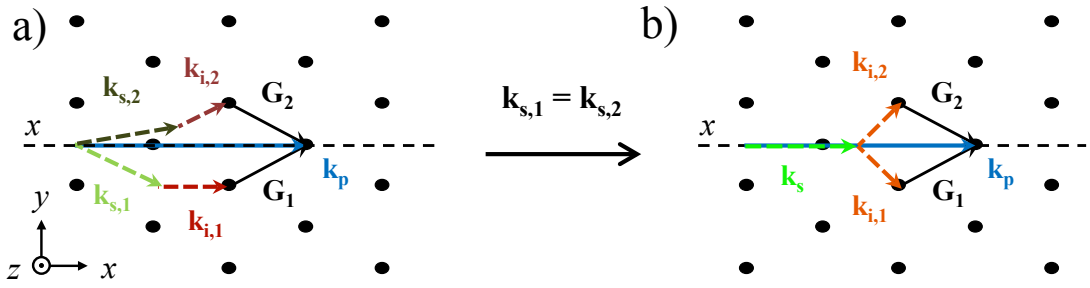

Fig. 5.1 QPM vector diagram of OPG processes with pump wave collinear to the symmetry axis x of a hexagonal lattice, i.e. $\theta_p = 0°$. $\mathbf{k}_p$, $\mathbf{k}_s$, and $\mathbf{k}_i$ are the wave vectors of the pump wave, signal waves and idler waves, with added indices according to the RLVs used for QPM, $\mathbf{G}_1$ and $\mathbf{G}_2$. a) Two arbitrary OPG processes. b) When the constraint of shared signal $\mathbf{k}_{s,1} = \mathbf{k}_{s,2}$ is applied coupled OPG is obtained. $\mathbf{k}_{i,1}$ and $\mathbf{k}_{i,2}$ are the wave vectors of twin-beam idler waves.

The coupled OPG arises in the special case where the solutions of Eqs. (5.1) and (5.2) satisfy the constraint of a shared signal wave $\mathbf{k}_{s,1} = \mathbf{k}_{s,2}$. The case is re-

ferred to as shared signal coupled OPG (SS-OPG). A direct consequence of the shared signal beam is the appearance of the twin-beam OPG conjugates, i.e. the twin-beam idler waves. These waves are spectrally degenerate, $\lambda_i = \lambda_s\lambda_p/(\lambda_s - \lambda_p)$, but propagate at different output angles.

In a similar way, coupled OPG can also occur through a *shared idler*, accompanied by twin-beam signal waves. The constraint for the shared wave then becomes $\mathbf{k}_{i,1} = \mathbf{k}_{i,2}$ and the case is denoted shared idler coupled OPG (SI-OPG).

An illustration of the SI-OPG special case of solutions of Eqs. (5.1) and (5.2) is given in Fig. 5.2. The figure shows the phase matching geometry of coupled OPG in a hexagonal QPM lattice in the form of a QPM vector diagram. The involved wave vectors and the base RLVs that phase match the interaction are included, as well as the pump input angle θ_p and the twin-beam signal angles $\theta_{s,1}$ and $\theta_{s,2}$. The QPM diagram is given for an arbitrary pump angle $\theta_p \neq 0°$, to illustrate that coupled OPG can occur for a full interval of pump angles, as will be shown in section 5.2.

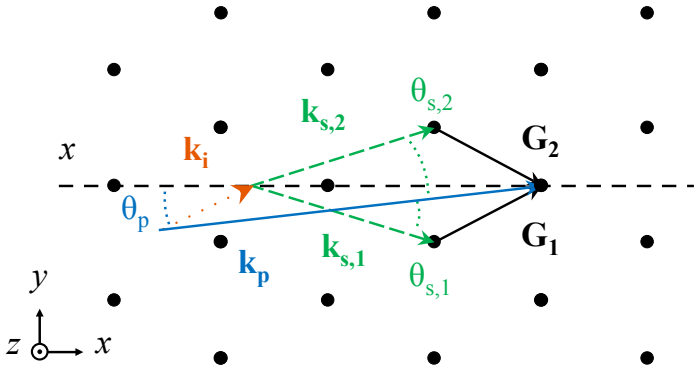

Fig. 5.2 QPM vector diagram of coupled OPG. θ_p is the pump angle to the NPC symmetry axis x. $\mathbf{k}_p$, $\mathbf{k}_i$, $\mathbf{k}_{s,1}$, and $\mathbf{k}_{s,2}$ are the wave vectors of the pump beam, the shared idler beam, and the twin-beam signals, the two latter propagating at angles $\theta_{s,1}$ and $\theta_{s,2}$ to the pump. $\mathbf{G}_1$ and $\mathbf{G}_2$ are the RLVs used for QPM.

The added dimensionality of 2D QPM lattices can also be exploited for sustaining simultaneous parametric processes. This has already been demonstrated in frequency upconversion, e.g. twin-beam second harmonic generation (SHG) [60]. In the symmetric case of twin-beam SHG, i.e. pump input angle $\theta_p = 0°$, the generated SH beams are spectrally – but not spatially – degenerate. Coupled OPG behaves somewhat differently. The coupled OPG twin-beams are similarly, spectrally – but not spatially – degenerate, however, the shared beam, which coherently couples the two OPG processes, is fully degenerate. Accordingly, the SHG processes are not coupled in the sense defined in this thesis. In the non-symmetric pump case, i.e. pump input angle $\theta_p \neq 0°$, the spectral degeneracy of twin-beam SHG is lost and the two SH wavelengths deviate symmetrically from the degenerate wavelength at $\theta_p = 0°$.

In 1D QPM, there has been one reported experiment which supported an interplay between two simultaneous optical parametric oscillation (OPO) processes, where a second dimensionality was introduced by a twin-beam pumping, i.e. using two non-collinear pump waves [94]. In the general case of the experiment, the generated signal waves were spatially degenerate, as a consequence of the OPO cavity, but

spectrally distinct. Only in the special case of symmetric pumping, the signal waves were spectrally and spatially degenerate, forcing the conversion processes to be coupled. However, the coupling relies critically on the presence of a cavity to enforce the required geometry and, in addition, necessitates a complex double pump configuration. In the investigations of coupled downconversion that are described in this thesis no cavity and only one pump beam are required to couple the two parametric processes, greatly facilitating the experimental arrangements.

There has been one experimental report of downconversion in 2D QPM lattices, prior to the work presented in this thesis. However, only a single RLV was used for the primary frequency conversion process and hence the lattice response was not substantially different from that of a 1D parametric interaction [95]. The experiments did not address coupled downconversion at all, as the 2D functionality consisted solely of higher order RLVs phase matching cascaded upconversion processes.

5.1.1 Experimental demonstration of coupled OPG

The configuration that has been investigated to demonstrate coupled OPG corresponded to the case of shared idler at a non-zero pump input angle (treated in article II). The expected non-collinear twin-beam signal waves would offered a means to distinguish a coupled OPG process from conventional non-coupled OPG. The coupled OPG response was further investigated by mapping the signal wavelengths and output angles, as function of the pump wavelength.

The NPCs used in the experiments were fabricated through 2D electric field poling [26] in 0.5 mm thick z-cut 1 mol% MgO-doped nearly stoichiometric $LiTaO_3$ (MgSLT) substrates by Katia Gallo. The material was chosen for its resilience to photorefraction and GRIIRA/BLIIRA (details given in section 3.4). The 1-cm-long lattice was 4-mm-wide to accommodate non-collinear interactions. A QPM period of 22.8 μm was chosen for the hexagonal lattice (see section 3.2.1 for further details) to permit coupled OPG by pumping in the Ti:sapphire spectral range. The choice of pump system was, as for the broadband OPG experiments, based on its spectral flexibility and possibility to deliver high peak intensity pulses. Experimental investigations explored the pump wavelength dependence of the OPG.

The coupled OPG response of the NPCs was investigated using 1.5 ps pulses at 1 kHz, tunable in the vicinity of 800 nm, generated by the amplified Ti:sapphire system described in chapter 4. The peak intensities of the pulses used in the experiment were in the range of $2 - 20$ GW/cm^2 and polarised along the z axis of the MgSLT crystal.

The pump was loosely focused in the crystal to an elliptical cross-section, with $1/e^2$-radii of 810 μm and 220 μm in the lateral (y) and vertical (z) directions, respectively. The pump was input at an angle of $\theta_p \sim 0.6°$. At the output of the crystal the pump was attenuated by a dichroic mirror, blocking radiation from 770 to 1050 nm (3 dB thresholds), and the signal OPG output was recorded by using a fibre-coupled optical spectrum analyser (OSA, Ando AQ6315A, sensitive from 350 to 1750 nm).

The signal OPG output, i.e. the signal twin-beams, could be located and clearly distinguished using an IR detection card (Thorlabs VRC2, sensitivity range: 800 –

1700 nm). Each twin-beam could then be selectively coupled into the OSA by setting up a spatial stop for the other output angles and focusing the remaining parametric output with a 50 mm spherical lens.

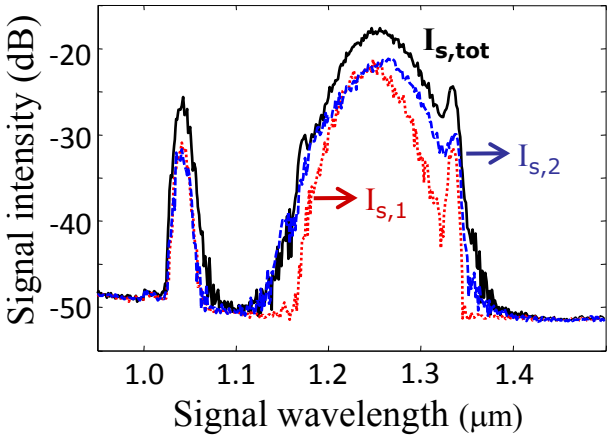

Fig. 5.3 Spectral measurements of the twin-beam signal waves of coupled OPG, emitted at $\theta_{s,1} = 2.9°$ and $\theta_{s,2} = -0.5°$ (with respect to the pump beam), made for $\theta_p \sim 0.6°$, $\lambda_p = 805$ nm and $I_p = 4.6$ GW/cm^2 (twice the OPG threshold). Dotted red curve: spectrum for the signal at $\theta_{s,1}$. Dashed blue curve: spectrum at $\theta_{s,2}$. Solid black curve: spectrum measured by coupling both signal beams into the optical spectrum analyser.

The interaction geometry of the investigated SI-OPG configuration at off-axis pumping is given in Fig. 5.2. Typical spectral measurements of the signal twin-beams for $\lambda_p \sim 795 - 810$ nm are shown in Fig. 5.3. The figure displays the spectral distributions measured on each of the twin-beams, at $\theta_{s,1} = 1.35°$ (dotted red curve) and $\theta_{s,2} = -0.22°$ (dashed blue curve), as well as on the total output (black solid curve), at $\lambda_p = 805$ nm. Despite the off-axis pumping (i.e. $\theta_p \neq 0°$), which breaks the symmetry in Eqs. (5.1) and (5.2), all three experimental curves exhibit the same spectral gain distribution, which could not be the case if the QPM resonances of Eqs. (5.1) and (5.2) were uncoupled. On the contrary, the spectral locking of the two signal outputs is the signature of a coupling between the two QPM resonances of the lattice achieved through a common idler, $\mathbf{k}_{i,1} = \mathbf{k}_{i,2}$, as illustrated in Fig. 5.2. The common idler enables a coherent cross-seeding path resulting in a mutual enhancement of the two QPM processes, thus lowering the OPG threshold, and can justify the frequency-degenerate signal response consistently observed in the experiments. Theoretical calculations performed with Eqs. (5.1) and (5.2) and the constraint of a shared idler wave $\mathbf{k}_{i,1} = \mathbf{k}_{i,2}$, yield parametric gain distributions as seen in the experiments. (A full description of the numerical method used to predict the coupled OPG is given in section 5.2.2.) For the specific example of Fig. 5.3 the calculations indeed predict a narrow OPG peak at $\lambda_s = 1030$ nm and a broader bulge centred around $\lambda_s = 1240$ nm. The broadness is due to the retracing behaviour of the QPM curves of $LiTaO_3$ in this spectral region, see section 4.1.1 and Ref. [96].

Upon ascertaining the spectral degeneracy of the twin-beam signals, the response of the NPC as function of pump wavelength was systematically recorded. The

entire parametric output was coupled to the OSA, thus the spectral properties of both OPG signal waves were examined. The results are displayed in Fig. 5.4a as a contour plot of the recorded signal powers, as function of pump and signal wavelengths. Overlaid onto the contour plot in Fig. 5.4a are the QPM predictions (black curve) of Eqs. (5.1) and (5.2) with the shared idler constraint, calculated using the Sellmeier equations from Ref. [21]. The experiments match the predictions well, with the exception of a shift to longer wavelengths.

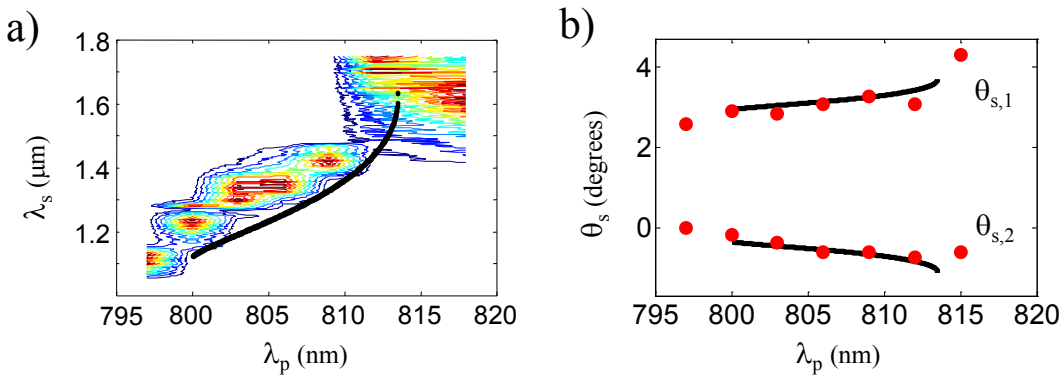

Fig. 5.4 a) Contour plots of recorded signal powers, as function of pump λ_p and signal λ_s wavelengths, generated in hexagonal NPCs of period 22.8 μm at θ_p~0.6° pump angle. b) Signal external angles θ_s as function of pump wavelength λ_p for the same conversion processes. The experimentally measured propagation angles for the signal beams are shown as red dots, QPM predictions as black curves. N.b. The angles of the experimental results are defined by the propagation directions outside the crystal (in contrast to Fig. 5.2).

The angular behaviour of the generated twin-beam signals for different pump wavelengths was measured by projecting the OPG signal output on a screen at a distance of 21 cm after the NPC. The measured signal angle values are displayed in Fig. 5.4b. Note that for all experimental measurements in this chapter the external angles are presented. The twin-beams could be clearly distinguished by using the IR detection card, as mentioned above. The pump beam could be detected with the same setup and was used as a reference for all angle measurements. Fig. 5.4b also shows the QPM predictions (black curves), calculated with Eqs. (5.1) and (5.2) and including the shared idler constraint.

In summary, this investigation constitutes the first experimental demonstration of coupled OPG in NPCs. The shared idler beam of the two simultaneous OPG processes mediates a coherent coupling, unique to 2D lattices. In particular, it also results in twin-beam signal generation, where the spectral contents of the signal waves of the two OPG processes are identical.

5.2 Full angular exploration of coupled OPG

In addition to the pump wavelength, the pump incidence angle presents a second possibility to control the spectral and angular properties of the coupled OPG response in NPCs. Having investigated coupled OPG through a shared idler in the previous section, it was investigated whether the complementary situation, shared signal coupled OPG (SS-OPG), would be possible to achieve. By varying the pump input angle the occurrences of SS-OPG and SI-OPG were investigated both experimentally and numerically.

I conducted a systematic, experimental study for various pump angles, presented in section 5.2.1. The signal wavelengths and propagation angles were recorded simultaneously to be able to distinguish coupled OPG from conventional non-coupled OPG, as well as to identify contributions originating from shared signal and shared idler coupling. In this section I will show how one can change between situations of strong SS-OPG and situations where SI-OPG is also present.

I developed a numerical framework that can model the rich, and significantly different, optical responses of coupled OPG at various pump incidence angles. The numerical model predicts both SS-OPG and SI-OPG as continuous functions of pump angle and is described in section 5.2.2.

Besides the spectral-angular analysis, I also investigated the dependence of generated signal intensity on the pump angle, in view of comparing coupled OPG and non-coupled OPG processes. The experimental results are presented and discussed in section 5.2.3.

5.2.1 Angular tuning experiments of coupled OPG

To investigate the possibility of sustaining both SI-OPG and SS-OPG, the incidence angle of the pump driving the coupled OPG was varied, while monitoring the output signal wavelengths and propagation angles. The signal intensities were chosen to be examined because of the flexibility and ease of detection provided by the OSA. The angles of the twin-beam signals of SI-OPG and the shared signal beam of SS-OPG provide a means, along with spectral comparisons, to identify the SS-OPG and SI-OPG contributions.

The angular tuning investigations (treated in article IV) were performed at $\lambda_p = 806$ nm, using $1 - 1.5$ ps pulses with peak intensities in the range of $6 - 20$ GW/cm^2, provided by the Ti:sapphire system described in chapter 4. The spectral and angular properties of the OPG signals were recorded for several pump angles in an interval of $-0.3° < \theta_p < 2.6°$.

The focusing conditions of the pump beam were chosen to illuminate as much of the width (along y) of the QPM lattice as possible, with beam radii of 2.0 mm ($1/e^2$) at the entrance and 2.1 mm at the exit of the lattice, while focusing strongly in the vertical direction (along z), to a minimum beam radius of 80 μm. The reason for the large lateral width of the pump was in part to sustain a spatial overlap with the non-collinear OPG waves, but also to suppress any possible transverse interference

effects [97]. The focusing along the z dimension was optimised to increase collection efficiency while maintaining a Rayleigh length that was comparable to the NPC length. At the output of the NPC device the pump was attenuated by a dichroic mirror blocking radiation from 770 to 1050 nm, as mentioned in section 5.1.1. The OPG signal output was recorded using the same fibre-coupled OSA as described in that same section.

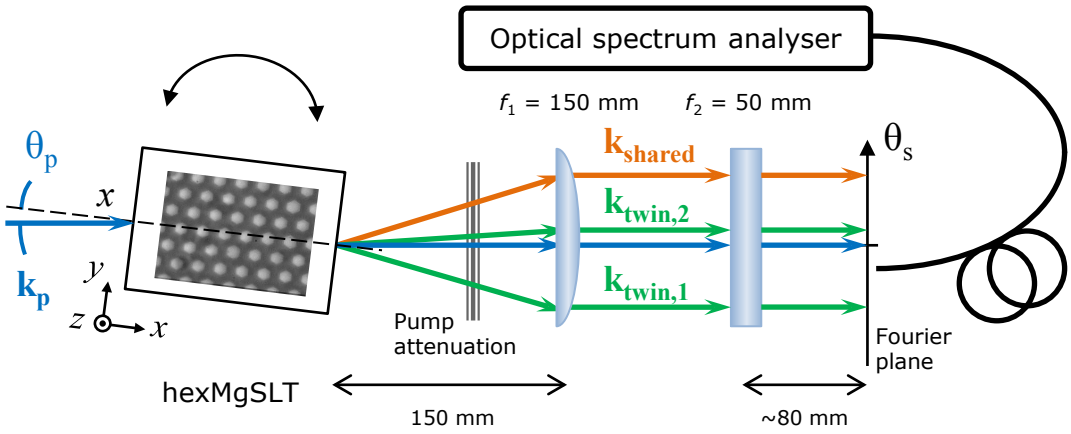

Fig. 5.5 Sketch of the Fourier plane detection setup used for the angular tuning experiments with 2D QPM lattices of 22.8 µm period, hexMgSLT = hexagonally poled MgSLT. The pump source (omitted in the sketch) was a Ti:sapphire amplified laser system delivering Gaussian µJ-pulses of picosecond durations at 1 kHz. The input beam was focused to radii of 80 µm in the vertical (z) dimension and of 2 mm in the lateral (y) dimension in order illuminate the entire QPM lattice of the crystal, which was kept constant at 85°C. The pump was attenuated by a dichroic mirror and the parametric output was imaged onto a Fourier plane along which the input fibre of an OSA could be translated.

The optical coupling to the OSA was further refined as compared to the wavelength tuning experiments discussed in section 5.1.1. The OSA was positioned at the Fourier plane of an imaging system consisting of two orthogonal cylindrical lenses of focal lengths 150 mm and 50 mm as described in Fig. 5.5. The former lens was positioned at focal distance from the crystal exit, thus defining the Fourier plane, while the latter focused the optical output to a line along which the fibre of the OSA could be translated. In this manner the spectral content of the NPC output at each propagation direction could be recorded, since each lateral position of the fibre corresponded to a propagation angle. The signal content of the NPC output at each angle θ_s, measured with respect to the pump, was systematically explored for various values of the pump input angle ($-0.3° < \theta_p < 2.6°$). The pump angle was selected by an in-plane (x-y) rotation of the NPC, with a precision of $\Delta\theta_p \sim 0.2°$. Spectral-angular maps of the signal output were obtained for $-4° \leq \theta_s \leq 4°$ and 1 µm $\leq \lambda_s \leq$ 1.75 µm. In addition, the outputs from higher order QPM upconversions to the visible, subsequent to the coupled OPG, were also recorded for a subset of pump input angles.

An investigation of possible SS-OPG at symmetric pumping, i.e. $\theta_p \sim 0°$, was performed. The interaction geometry and the QPM vector diagram for the possible SS-OPG interactions are illustrated in Fig. 5.6a. The result of the spectral-angular

mapping, i.e. signal powers recorded with the OSA over the angular interval mentioned above, is displayed in normalised logarithmic scale in Fig. 5.6b. The resolution of the spectral-angular mapping was 10 nm in the spectral λ_s dimension and 0.2° in the angular θ_s dimension. The pump beam propagation direction was used as reference for the output angles of the generated beams. However, due to the broad lateral extent of the pump beam there exists an uncertainty of ~0.2° in the measured output angles. The 2D colour map shows the recorded signal powers as function of their output angle, overlaid with QPM predictions (white curves) of potential OPG signals as described by Eqs. (5.1) and (5.2), calculated with the Sellmeier equations of Ref. [21].

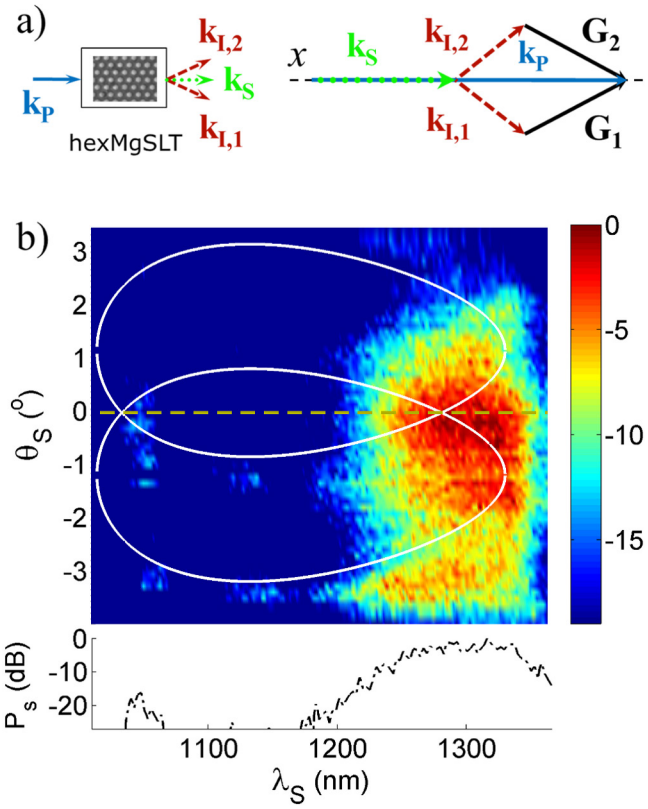

Fig. 5.6 a) Interaction geometry and QPM vector diagram of coupled OPG through a shared signal, pumped with λ_p = 806 nm at propagation angle θ_p~0° to the lattice symmetry axis x. $\mathbf{G}_1$ and $\mathbf{G}_2$ are the two RLVs used for QPM and $\mathbf{k}_j$ are the wave vectors of the interacting beams (where j = "p", "s", "i,1" and "i,2"). b) 2D colour map of the measured powers of the OPG signal, in normalised logarithmic scale, as function of wavelength (λ_s) and angle (θ_s) generated at θ_p~0° with a pump peak intensity of 19 GW/cm^2. The white curves are predictions of OPG signals according to Eqs. (5.1) and (5.2). Lower graph: signal spectrum at $\theta_s = 0$.

An artefact of the detection system, owing to the lateral translation of the fibre not being fully parallel to crystal's lateral plane, resulted in decreasing collection efficiency for increasing values of the signal angle. For this reason the distribution of the recorded signal powers P_s as function of the signal output angle θ_s is skewed towards $\theta_s < 0$, as seen in the 2D colour map of Fig. 5.6b. Nevertheless, the recorded signal powers still display a maximum at $\theta_s = 0$. This agrees well with the theoretical calcu-

lations, which predict a spectral and spatial degeneracy of the signals of the OPG processes, i.e. SS-OPG, phase matched by the base RLVs $\mathbf{G}_1$ and $\mathbf{G}_2$, at $\theta_s = 0$. The predictions of SS-OPG are indicated by the crossing points of the QPM trajectories, white curves in Fig. 5.6b. The theoretical calculations predict two spectral locations for SS-OPG, $\lambda_s = 1280$ and 1030 nm, due to the retracing behaviour of the QPM curves of $LiTaO_3$ in this spectral region [96]. (The model used for the predictions is further explained in section 5.2.2.) The predicted spectral locations match well the positions of the two local maxima observed in the experimental data recorded at $\theta_s = 0$, displayed in the graph showed in lower inset of Fig. 5.6b. The local signal maximum at $\sim$1030 nm is strongly attenuated by the dichroic mirror, since its 3 dB thresholds was situated at 1050 nm. Despite the attenuation, one can discern recorded signal powers in the 2D colour map and in the lower graph of Fig. 5.6b. Accordingly, the experimental results indicate that for $\theta_p \sim 0°$ SS-OPG was the dominating process in the conversion.

The comparison between the QPM curves and the experimental results indicates also slight shifts in predicted wavelengths and angles. This could possibly be attributed to discrepancies between the Sellmeier equations of Ref. [21] and the actual dispersion of our Mg-doped $LiTaO_3$ substrates in this wavelength range. The shift is consistent with the one recorded in the investigations of the broadband generation in 1D PPMgSLT (cf. chapter 4).

As mentioned above, the complementary situation to SS-OPG can also occur, in which the idlers of two OPG processes are spectrally and spatially degenerate, i.e. SI-OPG. One can control the coupled OPG output of the NPC device through the pump input angle. Specifically, moving away from the symmetric pumping can cause the response of the very same device to switch to a regime where SI-OPG is observable, in addition to SS-OPG. Fig. 5.7 exemplifies the case of SI-OPG at $\theta_p \sim 0.5°$, with the corresponding QPM configuration illustrated in Fig. 5.7a. Fig. 5.7b shows experimental and theoretical results obtained in a similar way as for Fig. 5.6b, this time for $\theta_p \sim 0.5°$.

Similar to the spectral-angular map in Fig. 5.6b, Fig. 5.7b is skewed towards $\theta_s < 0$ due to the artefact of the detection system pointed out earlier. Despite the lower detection efficiency for $\theta_s > 0$, one can distinguish local maxima, at $\lambda_s = 1300$ and $\sim$1050 nm, in the OPG response at $\theta_s \sim 2.5°$. The power at $\theta_s \sim 2.5°$ is also distinctly observable on an IR detection card (Thorlabs VRC2, sensitivity range: 800 – 1700 nm) as a separate beam. Comparing with the QPM curves calculated using Eqs. (5.1) and (5.2) (white curves in Fig. 5.7b), no SS-OPG is possible at that output angle.

The local maxima must instead originate from the two (due to retracing) twin-beam signals of SI-OPG, whose shared idlers are predicted at $\lambda_i = 2.1$ µm, $\theta_i = -0.9°$[4] and at $\lambda_i = 3.8$ µm, $\theta_i = -2.0°$. (Further details of the predictions are given in section 5.2.2.) The twin-beam signals of that SI-OPG working point are expected at $\lambda_s = 1300$ nm with $\theta_s = 2.4°$ and $\theta_s = -1.3°$, marked by dashed white ellipses in Fig. 5.7b. Indeed the experimental data show significant signal powers in these angular-spectral regions. By comparing the spectral content at $\theta_s = 2.4°$, where the exper-

[4] Note the printing error of article IV in that the minus sign of the idler angle is missing.

imental local maximum can be clearly distinguished, and at $\theta_s = -1°$, both displayed in the lower graph of Fig. 5.7b, one notes the spectral degeneracy, which implies a coherent coupling of the signals and consequently SI-OPG.

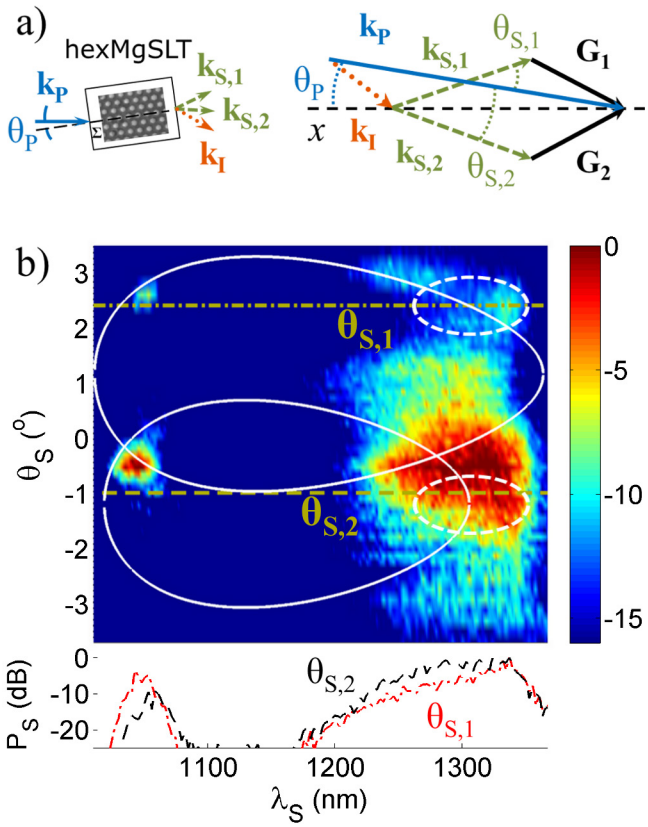

Fig. 5.7 a) Interaction geometry and QPM vector diagram of coupled OPG through a shared idler, pumped with λ_p = 806 nm at propagation angle θ_p~0.5°, labelled as in Fig. 5.6a. (b) Spectral-angular mapping of the signal powers, in normalised logarithmic scale, at θ_p~0.5°; all other conditions as in Fig. 5.6b. The angles for twin-beam signal generation are highlighted by the yellow dashed horizontal lines, labelled $\theta_{s,1}$ and $\theta_{s,2}$, whose intersections with the QPM predictions (white curves) give the locations for the twin-beam signals. The lower graph shows the corresponding spectra recorded for the twin-beam signals.

On the other hand, the twin-beam signal at $\theta_s \sim -1°$ arising from SI-OPG is not so neatly distinguishable as the one at $\theta_s = 2.4°$ in the 2D map of Fig. 5.7. This is due to both the proximity of a SS-OPG resonance, indicated by the crossing point of the QPM predictions (white curves) at $\lambda_s = 1280$ nm, and to the broadness of the involved resonances, both spectrally and angularly. The broadness is a result of both the spectral bandwidth $\Delta\lambda_p$~2 nm of the pump source and of the low group velocity dispersion in this spectral region (cf. section 4.1.1), giving rise to retracing behaviours of the QPM curves. Accordingly, the broad emission observed for $-1.7° < \theta_s < 0.3°$ in Fig. 5.7b is attributed to the merging of the above mentioned SS-OPG and the twin-beam signal of the SI-OPG resonance.

As a consequence, the strongest indicators of the presence of SI-OPG in the data of Fig. 5.7 are the local maxima in signal power around θ_s~2.5°. The non-collinear signal beams, clearly distinguishable on an IR detection card, at the numeri-

cally predicted locations of a SI-OPG process (see section 5.2.2) implies the presence of coupled OPG.

Due to retracing of the QPM curves, SS-OPG and twin-beams from SI-OPG are also predicted at 1030 and 1020 nm (details given in section 5.2.2), respectively, in analogy with the case of Fig. 5.6. Signal powers have been recorded in this spectral range, however, the 3 dB edge of the dichroic mirror used to block the pump is situated at 1050 nm. Thus the powers seen in Fig. 5.7b are probably only the flanks of the SS-OPG shared beam and SI-OPG twin-beams preventing any more detailed comparisons.

5.2.2 Tracking of coupled OPG

To properly analyse and explain the experimental data of the angular tuning investigations, a theoretical framework for modelling coupled OPG was developed. The model predicts the pump incidence angle dependence of coupled OPG, both for shared signal and for shared idler. It should be pointed out that even though hexagonal geometry is treated here, the model can be modified to predict coupled OPG in other lattice geometries,. In principle, the model affords predictions for any pump wavelength, but $\lambda_p = 806$ nm is chosen here to be able to describe the experimental results discussed above.

As mentioned at the beginning of section 5.1, given the two RLVs $\mathbf{G}_1$ and $\mathbf{G}_2$ of the 2D QPM lattice, the working points for which coupled OPG can be phase matched are described by the solutions of Eqs. (5.1) and (5.2) that satisfy either of the constraints $\mathbf{k}_{s,1} = \mathbf{k}_{s,2}$ or $\mathbf{k}_{i,1} = \mathbf{k}_{i,2}$. The former constraint corresponds to SS-OPG and the latter to SI-OPG. By combining the equations and a coupled OPG constraint one obtains a new set of equations for momentum and energy conservation. The new equations are rewritten using the indices *shared* and *twin* (with 1 or 2 added, to distinguish between $\mathbf{G}_1$ or $\mathbf{G}_2$ supporting the OPG) to denote the shared beam and the twin-beams, respectively. This is to describe the possibility for coupled OPG either through a shared signal or a shared idler beam. The new equations thus become

$$\begin{aligned} \mathbf{k}_p - \mathbf{G}_1 &= \mathbf{k}_{shared} + \mathbf{k}_{twin,1} \\ \mathbf{k}_p - \mathbf{G}_2 &= \mathbf{k}_{shared} + \mathbf{k}_{twin,2} \end{aligned} \tag{5.3}$$

and

$$\frac{1}{\lambda_p} = \frac{1}{\lambda_{shared}} + \frac{1}{\lambda_{twin}}. \tag{5.4}$$

By fixing the pump input angle the system is no longer underdetermined and a finite number of solutions can be found, representing possible coupled OPG process that the 2D lattice can phase match. The system of Eqs. (5.3) and (5.4) was solved for a range of different QPM periods and pump wavelengths.

To begin with, the case of SS-OPG is considered. The system of equations allows two different such solutions for a given pump angle. As mentioned briefly in section 5.2.1, this is due to the retracing of the QPM curves of $LiTaO_3$ in this spectral

region [96]. The concept of the retracing is illustrated by the QPM curves shown in Fig. 2.7. The red curve in Fig. 2.7b gives an example of how several local maxima of the generated intensity can arise. For the very same reason, two SS-OPG resonances, at different wavelengths, arise for each pump input angle. To the possible SS-OPG is added the possibility of phase matching SI-OPG, which results in a total of four possible coupled OPG solutions. In summary, for a fixed pump angle two SS-OPG resonances and two SI-OPG resonances can be phase matched by the NPC.

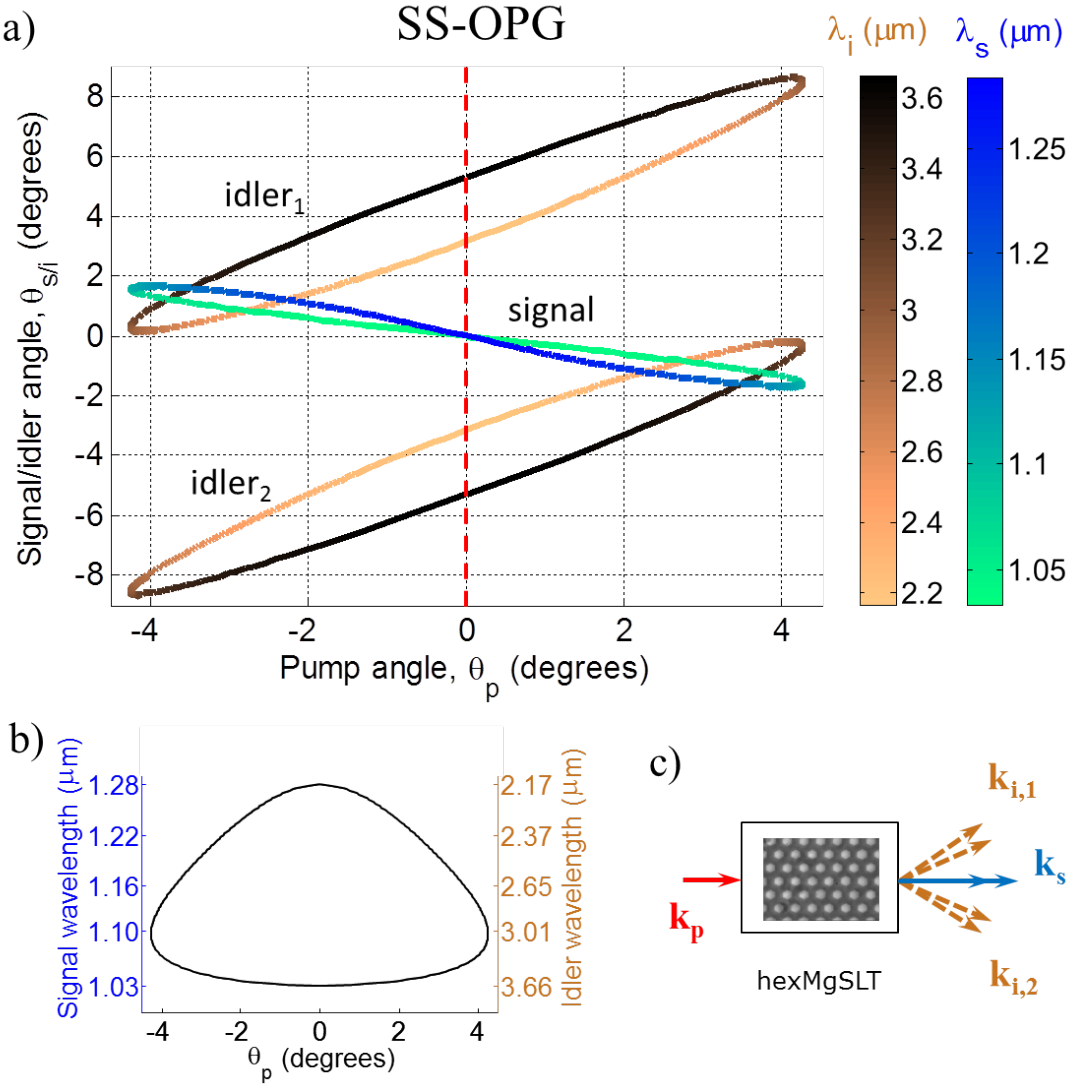

Fig. 5.8 Numerical predictions of shared signal coupled OPG for 22.8 μm QPM period and λ_p = 806 nm pump wavelength, obtained by solving the system of Eqs. (5.3) and (5.4). a) The blue-green curve describes the shared signal output angles θ_s and the orange-black the output angles of the twin-beam idlers θ_i, as functions of pump angle θ_p. The colours of the curves vary with the phase matched wavelengths, according to the respective colour bars. b) Signal and idler wavelengths (λ_s and λ_i) as functions of pump angle. c) Sketch of beam propagation directions of the beams involved in the two SS-OPG processes at $\theta_p = 0°$.

For a fixed pair of QPM period and pump wavelength, one set of simulations is made by letting the pump input angle assume every value for which phase matching of coupled OPG was possible, which included pumping parallel to the symmetry axis of the lattice x, $\theta_p = 0°$.

The simulations for 22.8 μm QPM period and λ_p = 806 nm pump wavelength, performed using the Sellmeier equations of Ref. [21], are given in Fig. 5.8 and Fig. 5.9. For practical reasons the simulation results are divided into the two cases of SS-OPG (Fig. 5.8) and SI-OPG (Fig. 5.9).

In Fig. 5.8a, presenting the predictions for SS-OPG, the green-blue curve represents the output angles θ_s of the shared signal beam as function of the pump input angle θ_p. The colouring of the curve corresponds to the wavelengths of the signal beam λ_s, according to the colour bar on the right. The orange-black curves describe the twin-beam idler output angles θ_i as function of the pump input angle θ_p. Analogously, the colouring of the curves corresponds to the wavelengths of the idler beams λ_i, according to the left colour bar. The signal and idler wavelengths are illustrated more quantitatively by Fig. 5.8b, where the black curve gives the two (due to retracing) pairs of signal and idler wavelength for each pump input angle θ_p.

The prediction for the working point of the experiments of Fig. 5.6, $\theta_p = 0°$, is marked in Fig. 5.8a by the dashed red line. The sketch in Fig. 5.8c illustrates the two triplets of signal and idler beams, i.e. the two different solutions that the system of Eqs. of (5.3) and (5.4) allows for a given pump angle. The theoretical predictions mentioned in the discussion of Fig. 5.6 can be recognised: $\theta_s = 0°$ and $\lambda_s = 1280$ and 1030 nm. The corresponding wavelengths and output angles for the two pairs of twin-beam idler beams of the two SS-OPG processes are: $\lambda_i = 2.2$ and 3.7 μm; $\theta_i = \pm 3.1$ and $\pm 5.3°$, respectively.

Fig. 5.9a shows the predictions for SI-OPG. The orange-black curve shows the output angles θ_i of the shared idler beam and the green-blue curves the angles θ_s of the twin-beam signals, as functions of the pump input angle θ_p. The idler and signal wavelengths, λ_i and λ_s respectively, are described by the colouring of the curves and by the graph of Fig. 5.9b, in the same way as in Fig. 5.8. The sketch in Fig. 5.9c illustrates the two triplets of signal and idler beams.

All wavelength and angle predictions for the beams involved in the SI-OPG configuration of Fig. 5.7b can be found at $\theta_p = 0.5°$ in Fig. 5.9a, marked by the dashed red line. The loci of the twin-beam signals, that were marked by dashed ellipses in Fig. 5.7b, are given by the crossing points of the dashed red line and the blue parts of the signal curves in Fig. 5.9a: $\lambda_s = 1300$ nm with $\theta_s = 2.4°$ and $\theta_s = -1.3°$. The crossing point of the dashed red line and orange part of the idler curve gives the wavelength and angle of the corresponding shared idler beam: $\lambda_i = 2.1$ μm and $\theta_i = -0.9°$. Furthermore, the dashed red line at $\theta_p = 0.5°$ reveals the second SI-OPG resonance, at $\lambda_i = 3.8$ μm and $\theta_i = -2.0°$, with its twin-beams signals at $\lambda_s = 1020$ nm and $\theta_s = 2.0°$ and $\theta_s = -1.0°$. As was described in section 5.2.1, also SS-OPG is obtained in the same experimental configuration. The theoretical predictions for the SS-OPG are given by a similar vertical slice at $\theta_p = 0.5°$ in Fig. 5.8a. The loci

of the two shared signals, originating from the two SS-OPG processes, are found to be at: $\theta_s = -0.3°$, $\lambda_s = 1280$ nm and $\theta_s = -0.2°$, $\lambda_s = 1030$ nm.

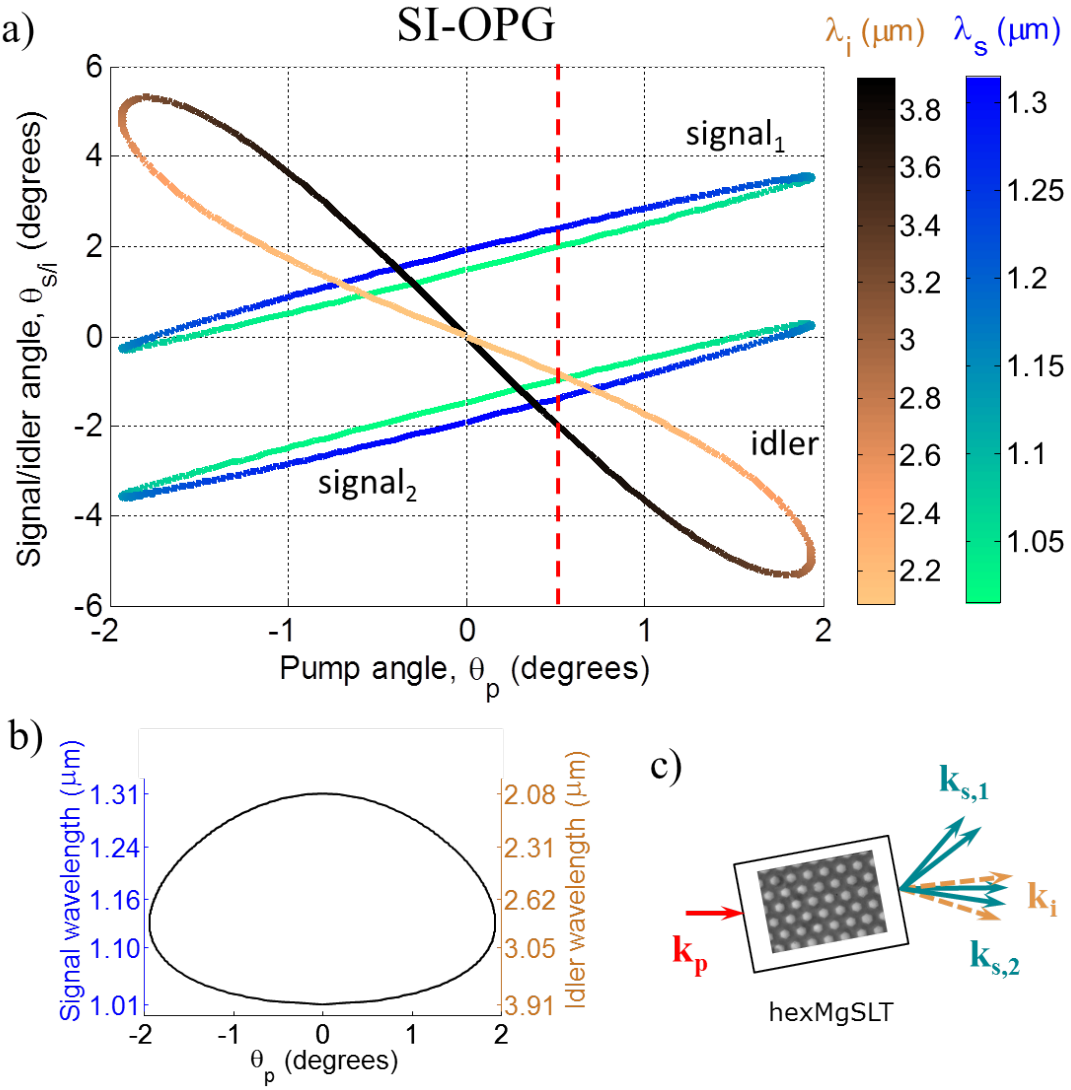

Fig. 5.9 Numerical predictions of shared idler coupled OPG for 22.8 μm QPM period and λ_p = 806 nm pump wavelength, obtained by solving the system of Eqs. (5.3) and (5.4). The orange-black curve describes the shared idler output angles θ_i and the blue-green the output angles of the twin-beam signals θ_s, as functions of pump angle θ_p. The colours of the curves vary with the phase matched wavelengths, according to the respective colour bars. b) Signal and idler wavelengths (λ_s and λ_i) as functions of pump angle. c) Sketch of beam propagation directions of the beams involved in the two SI-OPG processes at $\theta_p = 0.5°$.

5.2.3 Signal intensity dependence on pump angle

It has been suggested that the coherent coupling of multiple RLVs should lead to enhanced OPG gain [98]. The coupling of several downconversion processes, contrib-

uting to the same signal wave, can be expected to increase the gain. However, so far no experimental demonstration of this gain enhancement has been made.

To achieve a high gain one needs to minimise any non-collinear propagation angles, which can be done by minimising the angle between the pump propagation direction and the RLVs exploited for the QPM. Using a hexagonal lattice this angle becomes 30°, however when using a rectangular it instead becomes 45° [98]. For this reason it is favourable to employ a hexagonal lattice geometry and it is consequently the geometry used in our experiments.

In the experiments of coupled OPG presented in Fig. 5.6 and Fig. 5.7, the fact that there is appreciable signal intensity only at the locations corresponding to the coupled OPG processes, provides already a good indication for the gain of the latter to be higher than that of the competing non-coupled OPG processes. An investigation that could bring clarity to the issue would be to compare, in a working point such as those described in Fig. 5.6 or Fig. 5.7, phase-matching points of coupled OPG and of non-coupled OPG. Unfortunately, the spectral and angular broadness of the resonances makes this approach very difficult.

Instead, to gain further insights, the overall OPG signal generation as function of the pump propagation angle θ_p was investigated. The entire parametric output, i.e. integrated over all propagation angles, was focused onto a germanium photodetector (Newport 918D-IR-OD3, 850 – 1750 nm sensitivity range).

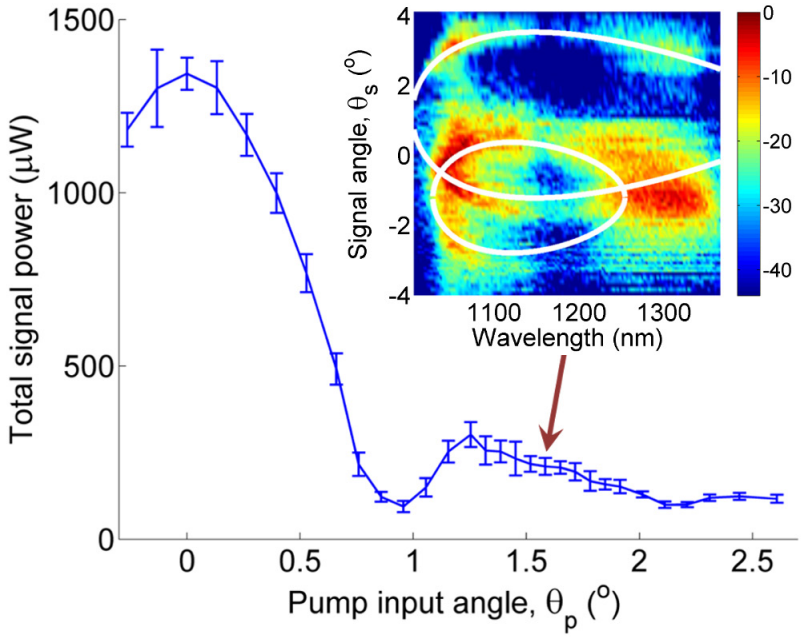

Fig. 5.10 Recorded total OPG average signal powers P_s as function of the pump input angle θ_p, generated with a pump peak intensity of 19 GW/cm^2 (corresponding to 96 mW average power). All other experimental parameters were kept constant at the values used for the investigations mapping the optical response in angular tuning, cf. Fig. 5.5. Error bars denote ±1 standard deviation. The OPG peak signal intensity corresponding to P_s at $\theta_p \sim 0°$ was 0.3 GW/cm^2. The inset shows the spectral-angular variation of the recorded signal powers (in normalised logarithmic scale) and the corresponding QPM predictions (white curves), for $\theta_p = 1.6°$ (cf. Fig. 5.6 or Fig. 5.7 for details).

With this detection system, the generated average signal powers P_s, integrated over all signal wavelengths, were recorded. Measurements were performed over a wide interval of pump propagation angles, as shown in the main graph of Fig. 5.10. Using spectral-angular maps, such as those of Fig. 5.6b and Fig. 5.7b, recorded for different pump angles θ_p the underlying OPG resonances could be identified for each θ_p of the curve of Fig. 5.10. As previously discussed, for $\theta_p \sim 0°$ OPG was mainly ascribed to SS-OPG (Fig. 5.6), while for $\theta_p \sim 0.5°$, in addition to SS-OPG, an increasing contribution from SI-OPG was apparent (Fig. 5.7). In contrast, for $\theta_p > 1°$ (i.e., on the low-efficiency sidelobe of the angular tuning curve of Fig. 5.10), coherently coupled processes were no longer dominating the OPG response. This is illustrated by the inset of Fig. 5.10, which shows the spectral-angular mapping recorded for $\theta_p \sim 1.6°$ alongside the theoretical predictions of Eqs. (5.1) and (5.2) (white curves). There are stronger components in the measured OPG output coming at spectral-angular locations that correspond to non-coupled OPG processes, i.e. following the curves. The local intensity maxima, recorded at the spectral-angular loci of SS-OPG, are also less well-confined (spectrally and angularly) than in Fig. 5.6b and Fig. 5.7b. These features, typical also for the other data points at $\theta_p > 1°$, indicate that shared wave OPG was no longer dominating over non-coupled OPG.

In other words, compared to the interval of pump angles where coupled processes dominate the OPG signal output a significantly lower total OPG signal power was recorded at pump angles $\theta_p > 1°$, where coupled OPG was no longer dominating over non-coupled OPG. A potential reason for the lower power could be the increasing output angles for the shared beam for increasing pump angles, seen in the numerical predictions, cf. Fig. 5.8 and Fig. 5.9. The larger output angles result in reduced spatial overlap between the shared beam and the pump beam, which could promote collinear, but non-coupled, OPG processes.

5.3 Cascaded upconversion and coupled OPG

The arrays of higher order RLVs in a NPC offer a wealth of possibilities to support parametric conversion processes. Consequently, cascaded conversion processes, i.e. frequency conversions driven by one or more waves generated in a previous parametric process in the same lattice, are more likely to be phase matched in 2D QPM lattices than in 1D QPM lattices. There exist experimental demonstrations of 2D NPCs supporting cascaded upconversion processes, both combinations of SHG and SFG [25, 99] as well as SHG following OPO [95].

This section describes the demonstration, correlated with theoretical predictions, of cascaded upconversion following a primary conversion that involves coherently coupled parametric processes. In particular, in the frame of this thesis I investigated cascaded SFG following coupled OPG, where multiple SFG processes were driven by the pump wave and either a signal or idler wave originating from the coupled OPG. The multiple SFG processes were thus supported by several different higher-order RLVs of the same hexagonal 2D lattice, whose base RLVs phase matched the

coupled OPG. The combination of SFG and coupled OPG reveals how NPCs can provide even further wavelength flexibility and possibilities of multi-beam generation.

5.3.1 Experimental demonstration of SFG following coupled OPG in MgSLT NPCs

In the experiments of coupled OPG the parametric output was accompanied by a rich, spectrally and angularly, output in the visible, resulting from multi-beam SFG following OPG. Photographs illustrating typical responses of the NPCs in the visible are displayed in Fig. 5.11.

The photographs were taken at two different pump angles, $\theta_p \sim 0.6°$ (Fig. 5.11a) and $\theta_p \sim 1.2°$ (Fig. 5.11b), at a pump wavelength of $\lambda_p = 806$ nm. The pump pulses were of 1.5 ps duration and their peak intensity 2.7 GW/cm^2. The pump was loosely focused in the crystal to an elliptical cross-section, with 1/e^2-radii of 810 μm and 220 μm in the lateral (y) and vertical (z) directions, respectively. The parametric output was projected on a white screen positioned 21 cm after the NPC. The rest of the experimental parameters were as described in section 5.2.1.

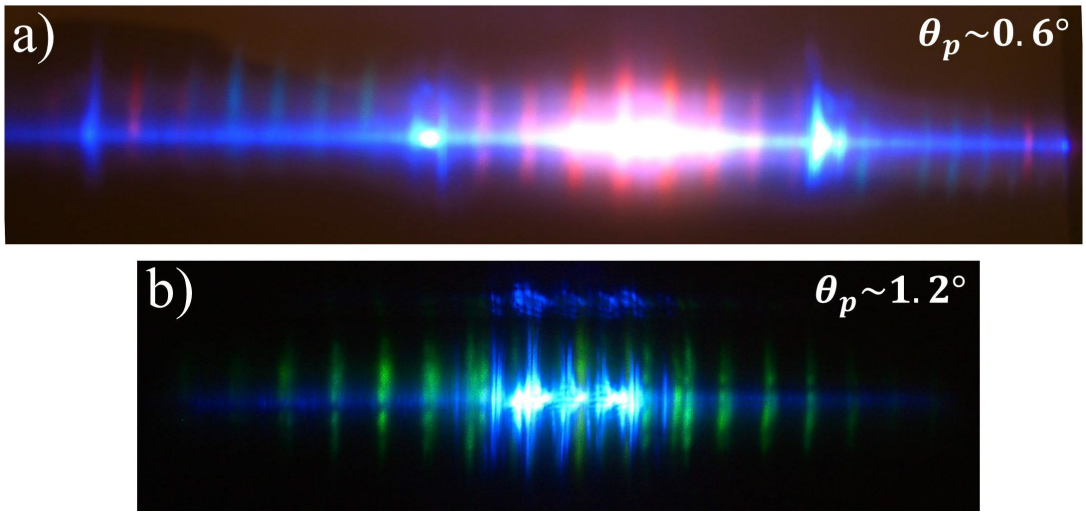

Fig. 5.11 Photographs of the far field output of NPCs of 22.8 μm period when pumped at $\lambda_p = 806$ nm, showing multi-beam, multi-wavelength generation by up-conversion via higher order RLVs of the 2D lattice. The pump input angle was a) $\theta_p \sim 0.6°$ and b) $\theta_p \sim 1.2°$.

The colours in the photographs are as follows. Blue is the SHG of the pump wave, at $\lambda_{SH} = 403$ nm. The SHG output consisted of distinct lobes of twin-beam SHG resonances, as explained in Refs. [23, 60], and a weaker horizontal line. The latter was generated over a continuum of output angles, none of which were phase matched by the lattice. However, due to the high intensity of the pump wave and the high nonlinear coefficient of MgSLT the SHG still reached appreciable output powers.

The green, seen as clear vertical lines in Fig. 5.11b and as faint lines at output angles slightly larger than the SHG lobes in Fig. 5.11a, was due to SFG at $\lambda_{SF} = 515\ \text{nm}$. The SFG was generated by the pump wave and a signal wave at $\lambda_s = 1.43\ \mu\text{m}$.

The red-pink, seen as vertical lines in Fig. 5.11a, were in reality yellow-orange (the CCD camera that was used distorted the colouring). These lines originated from another cascaded SFG at $\lambda_{SF} = 575\ \text{nm}$, driven by the pump wave and an idler wave at $\lambda_i = 2.01\ \mu\text{m}$.

One can control the parametric output of the NPC device through the pump input angle. Changing the pump propagation angle by merely 0.6° completely altered which SF wavelengths that were generated and at which angles the SF lines appeared.

For each generated SF wavelength one notes several vertical lines of (approximately) the same wavelength. Each line corresponds to one SFG process, phase matched by a given RLV of the 2D QPM lattice, as described in section 3.2.2. Each line corresponds to a SF beam at a specific propagation angle, generated by QPM via a specific RLV. To explain more in detail of this multi-resonance behaviour of the NPC, the generation of a particular SF wavelength $\lambda_{SF} = 575\ \text{nm}$ is treated below.

The photographs of Fig. 5.11 only describe the experimental results of the cascaded SFG qualitatively. For quantitative measurements the Fourier plane detection system of Fig. 5.5 was instead employed. A recorded spectral-angular map of the SF wavelengths in the vicinity of 575 nm is displayed in Fig. 5.12a, powers given in normalised logarithmic scale. The pump wavelength was $\lambda_p = 806\ \text{nm}$ and the pump beam was input at $\theta_p \sim 0.6°$. The resolution in the spectral λ_{SF} and angular Φ_{SF} dimensions were increased to 1 nm and 0.1°, respectively, as compared to the coupled OPG measurements described in section 5.2.1. In Fig. 5.12a, one can distinguish four local maxima of the SF intensities at $\Phi_{SF} \sim 3°$, $1.5°$, $-0.3°$ and $-2°$. The output angles correspond to those of the four central red-pink lines, i.e. the SF beams, in Fig. 5.11a.

Assuming that the pump is one of the two waves driving the SFG, the (approximate) wavelength of the other can be calculated from the experimental value of the SFG wavelength of 575 nm. This gives the wavelength of $\lambda_i = 2.01\ \mu\text{m}$, i.e. an idler wave was driving the SFG together with the pump wave. The presence of this idler wavelength was verified, using the near to mid-IR scanning monochromator described in section 4.1.1. Knowing the idler and pump wavelengths and the pump input angle, the idler propagation angle can be calculated using the numerical model presented in section 5.2.2.

Using these four parameters, a Ewald sphere construction is employed to find out which RLVs that could possibly phase match the four SFG processes, corresponding to each of the four SF beam. The momentum conservation equation describing a phase-matched SFG process is

$$\mathbf{G}_{l,m} + \mathbf{k}_i + \mathbf{k}_p = \mathbf{k}_{SF}. \tag{5.5}$$

$\mathbf{G}_{l,m}$ is the RLV that phase matches the particular SFG process in question and $\mathbf{k}_\text{i}$, $\mathbf{k}_\text{p}$, and $\mathbf{k}_\text{SF}$ are the wave vectors involved in the conversion.

The Ewald sphere construction is presented in Fig. 5.12b, as a plot in the reciprocal space made in the same manner as Fig. 3.4. The grid points describe the reciprocal lattice of the NPC. The resulting vector of $\mathbf{k}_i + \mathbf{k}_p$ is positioned so that it has its end point on a grid point marked in red. From this reciprocal lattice point the coordinate numbering in the ($\mathbf{G}_1 \equiv \mathbf{G}_{10}$, $\mathbf{G}_2 \equiv \mathbf{G}_{01}$) base emanates. The Ewald sphere is drawn with its centre on the opposite end point of the vector $\mathbf{k}_i + \mathbf{k}_p$ (not shown in Fig. 5.12b because the vector is too long). The Ewald sphere of the 575 nm SFG (purple curve) is close to intersecting four grid points in the reciprocal space, meaning that SFG in the vicinity of this wavelength can potentially be phase matched by the RLVs corresponding to the four grid points. The four RLVs suggested by this single-wavelength modelling are inserted, one by one, into Eq. (5.5). The equation is solved numerically for each RLV, to give the exact SF wavelength and propagation angle for the SF beam that is supported by the RLV in question.

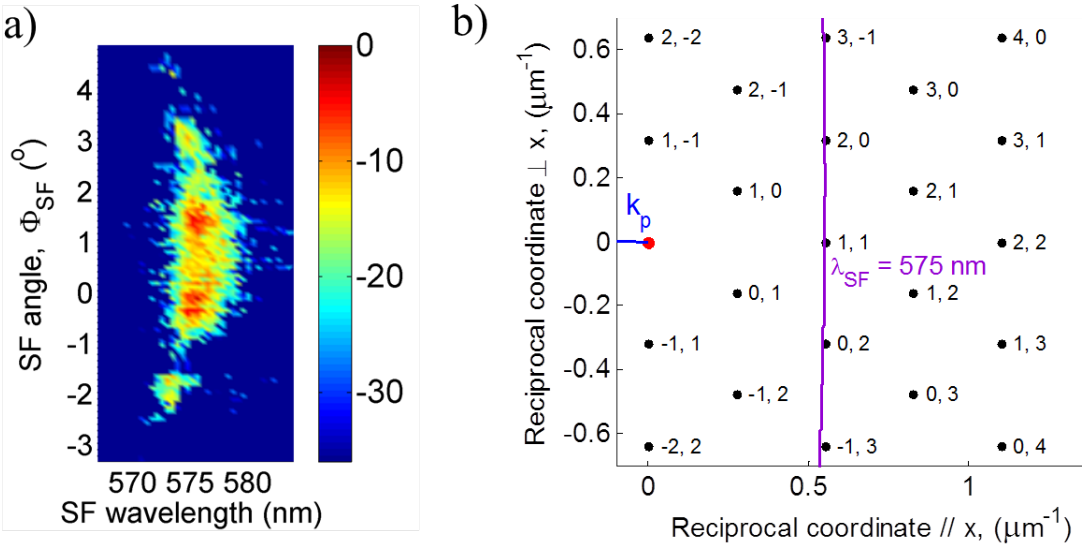

Fig. 5.12 a) 2D colour map of the recorded powers of the cascaded SFG, in MgSLT NPCs of 22.8 μm QPM period, driven by a pump wave at λ_p = 806 nm and an idler wave at $\lambda_i \approx$ 2.01 μm originating from coupled OPG. The pump input angle was $\theta_p \sim 0.6°$. The SF powers are displayed in normalised logarithmic scale, as function of wavelength (λ_{SF}) and output angle (Φ_{SF}). b) Numerical results from Ewald sphere predictions. The tip of the pump wave vector (blue) and the Ewald sphere of a λ_{SF} = 575 nm SF wave vector (purple) are shown, cf. Fig. 3.4. The number pairs denote the lattice coordinates in the ($\mathbf{G}_1 \equiv \mathbf{G}_{10}$, $\mathbf{G}_2 \equiv \mathbf{G}_{01}$) base. The lattice coordinates can be translated into reciprocal coordinates, i.e. μm^{-1} units, using Eqs. (3.32) and Λ = 22.8 μm.

The predicted propagation angles and the wavelengths of the four SF beams are: $\Phi_{SF} = 3.0°,\ 1.4°,\ -0.3°,\ -2.0°$ and $\lambda_{SF} = 573.6\ \text{nm},\ 574.7\ \text{nm},\ 574.6\ \text{nm},\ 573.4\ \text{nm}$. The predicted output angle values for the SF beams match well the experimentally recorded values. By examining Fig. 5.12a more closely, one can note that the tendency for SF beams at larger propagation angles to display shorter wavelength is found also in the experimental results. In other words, both the predicted wavelength and angle values are consistent with experiments.

To summarize this section, it has been showed that coupled OPG in 2D lattices, in cascade with SFG, grants access to a broad spectral range in which waves can be generated, from the IR to the blue edge of the visible spectrum. This spectral flexibility, in combination with the possibility to generate numerous discrete beams, demonstrates that by properly designing the 2D lattice complex sources of coherent light can be created. In addition, it has been shown by the examples in Fig. 5.11 that by simply changing the pump propagation direction, the spatial and spectral properties of the parametric output can be altered.

Chapter 6

Conclusions and outlook

6.1 Broadband optical parametric generation

Ultra-broadband parametric gain has been demonstrated in periodically poled MgSLT (PPMgSLT), pumped with picosecond pulses through downconversion to the vicinity of the zero GVD point of the material, as described in section 4.1. OPG bandwidths as broad as 185 THz (at 10 dB), spanning the full spectrum from 1.1 to 3.7 μm, were achieved with a pump at 860 nm in PPMgSLT with 25 μm QPM lattice period. This is so far the broadest band generated in parametric downconversion in the near to mid-IR spectral range. There are two previously demonstrated cases of broadband parametric gain of comparable width centred at 650 nm and 990 nm [36, 90], but none in the spectral region of the results reported here. Comparing the results in PPMgSLT to previous demonstrations of broadband band gain in the same spectral region, using PPLN or PPKTP, the OPG in PPMgSLT displayed a more spectrally flat response.

A natural development of this work would be to use the ultra-broadband gain for coherent amplification of ultrashort pulses. Using a coherent seed source of broad bandwidth, e.g. the self-phase modulation when focusing an ultrashort pulse into a sapphire crystal [100], ultra-broadband amplification and subsequent compression can be achieved. In the investigated case of broadband generation in PPMgSLT the gain band can theoretically support transform-limited pulses down to 2.4 fs duration, if exploiting both signal and idler wavelengths.

A second application that could be envisioned involves the creation of a source that can generate selected wavelength(s) from the entire super-octave-spanning interval of the OPG process. The PPMgSLT crystal would then be used as an OPG device after which a system for spectral selection is placed. A further improvement of

the source could be to use a second PPMgSLT crystal as a parametric amplifier, seeded by the output from the spectral selection system.

The OPG experiments were performed with a Ti:sapphire system as pump source, since its wide tunability permitted a large interval of pump wavelengths to be investigated. Having identified the optimal pump wavelengths for ultra-broadband gain, around 860 nm, a different pump source can be selected from e.g. a power perspective. For instance one could instead choose a Cr^{3+}:$LiSrAlF_6$ laser [101], which would improve pump efficiency, something that both of the above applications could benefit from.

In general MgSLT is a promising material with respect to increasing the generated powers, through pump power upscaling. The material has displayed good power-handling capabilities at high pump powers [73] and its low coercive field offers the possibility to pole thicker crystals thus creating periodically poled devices with larger apertures.

Moreover, the range of wavelengths that can be generated could be afforded through super-structured QPM lattice designs [102], albeit at the cost of a reduction in efficiency and an increase in fabrication complexity.

6.2 Quadratic cascading in broadband parametric generation

Experimental investigations and numerical simulations have shown it possible to reverse the energy flow of SFG processes, subsequent to broadband OPG, by reducing the pump pulse duration, as described in section 4.2. In so doing the temporal walk-off initiates downconversion of the SF wave back to the OPG band, turning the gain dips, typically observed in broadband OPG using QPM materials, into peaks.

Having identified the link between pump pulse duration and the shape of the SFG resonances in the spectral profile of the broadband OPG, it is possible to find an optimal pump pulse duration to minimise the impact of the parasitic SFG resonances. This is particularly interesting for systems that focus on delivering tunable optical power over a broad spectral range, since in that context it is important to supply a constant output power across all wavelengths.

The reduction of the impact of the parasitic SFG resonances is also appealing for ultrashort pulse amplification systems. A flat gain spectrum is desirable to balance the contribution from the different spectral components when amplifying ultrashort pulses, in order to sustain a temporal profile that is as close as possible to transform limited.

The proof-of-principle demonstration of the cascading control of the SFG resonances has been performed in a uniform QPM lattice. To complement such optical tuning capabilities, one could exploit also QPM engineering to suppress parasitic upconversion processes. Nevertheless, this would still be a permanent feature altering the device response, not adjustable after fabrication, but it could well be used in conjunction with the adaptable method of reducing the impact of SFG through pump

pulse duration. In this way the finer modifications to the SFG features could be optically controlled through the pump beam properties. Such optical control of conversion processes, offered by NPCs, is of great appeal since it provides flexibility and the possibly of fast manipulation of the conversion.

6.3 Coupled optical parametric generation in 2D QPM lattices

Coherent cross-seeding between two OPG processes in a nonlinear photonic crystal (NPC) has been experimentally demonstrated, as described in sections 5.1 and 5.2. The OPG response has been investigated as function of the pump wavelength and input angle, by mapping the spectral and angular characteristics of the generated signals and coupling it with a theoretical framework. It has been shown that the OPG waves exhibit spectral and angular qualities lacking counterpart in 1D QPM geometries. The spectral locking of the waves involved in the two OPG processes, owing to the shared beam, exemplify the engineering capabilities offered by 2D NPCs in frequency downconversion and holds promise for novel applications.

The identical spectral contents of the simultaneously generated twin-beams could, for instance, be exploited to copy the information carried by a seed beam by creating a replica in the form of a second beam. The NPC could then serve as a compact device for e.g. routing optical signals [103, 104], with the added advantage compared to the compact devices in e.g. Ref. [105] of providing amplification for both the seed wave and its copy. Cascading several NPCs could extend the idea to multiport parametric devices.

Both shared signal and shared idler coupled OPG configurations have been examined. By adjusting the pump input angle it is possible to alter significantly the spectral and angular properties of the output, as seen in section 5.2. For instance, the twin-beam generation can be achieved either in the mid-IR or near IR spectral regions. The spectral and angular properties of the shared beam and twin-beams can also be finely tuned, as predicted by the developed theoretical framework.

Further prospects are the realisation of dual-frequency optical parametric oscillators and investigating sources based on the multi-photon entanglement of the coupled OPG. Very recently, sources of two-photon entanglement have been proposed and demonstrated for degenerate downconversion based on the same coupled OPG interaction scheme presented in this thesis, with a translation to a spectral range more convenient for single-photon experiments [106, 107]. The reports were rapidly followed by a comprehensive experimental demonstration of sources of single-photon and two-photon entangled states in hexagonally poled $LiTaO_3$ crystals [108], also based on the coupled OPG interaction scheme. This proves the potential of coupled OPG in NPCs to develop compact sources for pioneering quantum mechanical investigations based on multi-mode entangled states [108].

The current interest in 2D NPCs is substantiated by other groups investigating coupled downconversion processes, in both $LiNbO_3$ and $LiTaO_3$. Two reports have

been published where several minor coupled downconversion processes were observed as a side-effect to the demonstration of compact Q-switched intracavity conversion devices which was the key result of the reports [109, 110]. Only higher order RLVs phase matched the SS-OPG and SI-OPG processes, consequently limiting intrinsically the maximum possible conversion efficiency. A third report focusing solely on SI-OPG in rectangular lattices has been published very recently [111], reproducing the experiments in the symmetric pumping configuration described in Fig. 5.6.

A broad range of wavelengths, from the mid-IR to the blue edge of the visible spectrum, was demonstrated through the combination of coupled OPG and cascaded SFG in the same lattice, as described in section 5.3. The wealth of higher order reciprocal lattice vectors of the NPC offers many possibilities to phase match multiple processes, which can generate multiple coherent beams at multiple wavelengths in a single compact device.

Lastly, SFG is intrinsically dependent on the coherence of the involved light waves. Thanks to this, the SFG could provide a means to investigate the coherence properties of the waves generated by the coherently coupled downconversion processes [112]. However, the complexity of such a method would plausibly render it less appealing than investigating directly the waves of the coupled downconversion by other means.

References

[1] Maiman, T.H., *Stimulated Optical Radiation in Ruby,* Nature **187** (4736) 493-494 (1960).

[2] Fejer, M.M., *Nonlinear Optical Frequency Conversion,* Physics Today **47** (5) 25 (1994).

[3] Franken, P.A., A.E. Hill, C.W. Peters, and G. Weinreich, *Generation of Optical Harmonics,* Physical Review Letters **7** (4) 118-119 (1961).

[4] Bass, M., P.A. Franken, A.E. Hill, C.W. Peters, and G. Weinreich, *Optical Mixing,* Physical Review Letters **8** (1) 18-18 (1962).

[5] DiDomenico, M., R.H. Pantell, O. Svelto, and J.N. Weaver, *Optical frequency mixing in bulk semiconductors,* Applied Physics Letters **1** (4) 77-79 (1962).

[6] Harris, S.E., M.K. Oshman, and R.L. Byer, *Observation of Tunable Optical Parametric Fluorescence,* Physical Review Letters **18** (18) 732-734 (1967).

[7] Armstrong, J.A., N. Bloembergen, J. Ducuing, and P.S. Pershan, *Interactions between Light Waves in a Nonlinear Dielectric,* Physical Review **127** (6) 1918-1939 (1962).

[8] Yamada, M., N. Nada, M. Saitoh, and K. Watanabe, *First-order quasi-phase matched $LiNbO_3$ waveguide periodically poled by applying an external field for efficient blue second-harmonic generation,* Applied Physics Letters **62** (5) 435-436 (1993).

[9] Eyres, L.A., P.J. Tourreau, T.J. Pinguet, C.B. Ebert, J.S. Harris, M.M. Fejer, L. Becouarn, B. Gerard, and E. Lallier, *All-epitaxial fabrication of thick, orientation-patterned GaAs films for nonlinear optical frequency conversion,* Applied Physics Letters **79** (7) 904-906 (2001).

[10] Giordmaine, J.A., *Mixing of Light Beams in Crystals,* Physical Review Letters **8** (1) 19-20 (1962).

[11] Maker, P.D., R.W. Terhune, M. Nisenoff, and C.M. Savage, *Effects of Dispersion and Focusing on the Production of Optical Harmonics,* Physical Review Letters **8** (1) 21-22 (1962).

[12] Cerullo, G. and S. De Silvestri, *Ultrafast optical parametric amplifiers,* Review of Scientific Instruments **74** (1) 1-18 (2003).

[13] Cerullo, G., D. Polli, G. Lanzani, S. De Silvestri, H. Hashimoto, and R.J. Cogdell, *Photosynthetic light harvesting by carotenoids: detection of an intermediate excited state,* Science **298** (5602) 2395-8 (2002).

[14] Brabec, T. and F. Krausz, *Intense few-cycle laser fields: Frontiers of nonlinear optics,* Reviews of Modern Physics **72** (2) 545-591 (2000).

[15] Gattass, R.R. and E. Mazur, *Femtosecond laser micromachining in transparent materials,* Nat Photon **2** (4) 219-225 (2008).

[16] Tittel, F.K., D. Richter, and A. Fried, *Mid-Infrared Laser Applications in Spectroscopy*, in *Solid-State Mid-Infrared Laser Sources*, I.T. Sorokina and K.L. Vodopyanov, editors. Springer Berlin Heidelberg. 458-529 (2003).

[17] Schliesser, A., N. Picque, and T.W. Hansch, *Mid-infrared frequency combs,* Nat Photon **6** (7) 440-449 (2012).

[18] Langrock, C., S. Kumar, J.E. McGeehan, A.E. Willner, and M.M. Fejer, *All-Optical Signal Processing Using $\chi^{(2)}$ Nonlinearities in Guided-Wave Devices,* Journal of Lightwave Technology **24** (7) 2579 (2006).

[19] Lim, H.C., A. Yoshizawa, H. Tsuchida, and K. Kikuchi, *Wavelength-multiplexed entanglement distribution,* Optical Fiber Technology **16** (4) 225-235 (2010).

[20] Nakamura, M., S. Takekawa, K. Terabe, K. Kitamura, T. Usami, K. Nakamura, H. Ito, and Y. Furukawa, *Near-Stoichiometric $LiTaO_3$ for Bulk Quasi-Phase-Matched Devices,* Ferroelectrics **273** (1) 199-204 (2002).

[21] Kolev, V.Z., M.W. Duering, and B. Luther-Davies, *Corrections to refractive index data of stoichiometric lithium tantalate in the 5-6 μm range,* Opt. Lett. **31** (13) 2033-2035 (2006).

[22] Berger, V., *Nonlinear Photonic Crystals,* Physical Review Letters **81** (19) 4136-4139 (1998).

[23] Broderick, N.G.R., G.W. Ross, H.L. Offerhaus, D.J. Richardson, and D.C. Hanna, *Hexagonally Poled Lithium Niobate: A Two-Dimensional Nonlinear Photonic Crystal,* Physical Review Letters **84** (19) 4345-4348 (2000).

[24] Ellenbogen, T., N. Voloch-Bloch, A. Ganany-Padowicz, and A. Arie, *Nonlinear generation and manipulation of Airy beams,* Nat Photon **3** (7) 395-398 (2009).

[25] Broderick, N.G.R., R.T. Bratfalean, T.M. Monro, D.J. Richardson, and C.M. de Sterke, *Temperature and wavelength tuning of second-, third-, and fourth-harmonic generation in a two-dimensional hexagonally poled nonlinear crystal,* Journal of the Optical Society of America B **19** (9) 2263-2272 (2002).

[26] Gallo, K., C.B.E. Gawith, and P.G.R. Smith, *Bidimensional Hexagonal Poling of $LiNbO_3$ for Nonlinear Photonic Crystals and Quasi-Crystals,* Ferroelectrics **340** (1) 69-74 (2006).

[27] Yariv, A. and P. Yeh, *Photonics: Optical electronics in modern communications*. 6th ed. New York: Oxford University Press (2007).

[28] Byer, R.L. and R.L. Herbst, *Parametric oscillation and mixing*, in *Nonlinear Infrared Generation*, Y.R. Shen, editor. Springer Berlin Heidelberg. 81-137 (1977).

[29] Boyd, G.D. and C.K.N. Patel, *Enhancement of optical second harmonic generation (SHG) by reflection phase matching in ZnS and GaAs,* Applied Physics Letters **8** (12) 313-315 (1966).

[30] Thompson, D.E., J.D. McMullen, and D.B. Anderson, *Second-harmonic generation in GaAs "stack of plates" using high-power CO_2 laser radiation,* Applied Physics Letters **29** (2) 113-115 (1976).

[31] Piltch, M.S., C.D. Cantrell, and R.C. Sze, *Infrared second-harmonic generation in nonbirefringent cadmium telluride,* Journal of Applied Physics **47** (8) 3514-3517 (1976).

[32] Pasiskevicius, V. and F. Laurell, *Optical parametric generators and amplifiers*, in *Mid-Infrared Coherent Sources, NATO Science Series*, M. Ebrahimzadeh and I. Sorokina, editors. Springer (2008).

[33] Carrasco, S., M.B. Nasr, A.V. Sergienko, B.E. Saleh, M.C. Teich, J.P. Torres, and L. Torner, *Broadband light generation by noncollinear parametric downconversion,* Opt. Lett. **31** (2) 253-255 (2006).

[34] Driscoll, T.J., G.M. Gale, and F. Hache, *Ti:sapphire second-harmonic-pumped visible range femtosecond optical parametric oscillator,* Optics Communications **110** (5–6) 638-644 (1994).

[35] Gale, G.M., M. Cavallari, T.J. Driscoll, and F. Hache, *Sub-20-fs tunable pulses in the visible from an 82-MHz optical parametric oscillator,* Opt. Lett. **20** (14) 1562-1564 (1995).

[36] Adachi, S., P. Kumbhakar*, and T. Kobayashi, *Quasi-monocyclic near-infrared pulses with a stabilized carrier-envelope phase characterized by noncollinear cross-correlation frequency-resolved optical gating,* Opt. Lett. **29** (10) 1150-1152 (2004).

[37] Brida, D., C. Manzoni, G. Cirmi, M. Marangoni, S. Bonora, P. Villoresi, S. De Silvestri, and G. Cerullo, *Few-optical-cycle pulses tunable from the visible to the mid-infrared by optical parametric amplifiers,* Journal of Optics **12** (1) 013001 (2010).

[38] Trapani, P.D., A. Andreoni, C. Solcia, P. Foggi, R. Danielius, A. Dubietis, and A. Piskarskas, *Matching of group velocities in three-wave parametric interaction with femtosecond pulses and application to traveling-wave generators,* J. Opt. Soc. Am. B **12** (11) 2237-2244 (1995).

[39] Danielius, R., A. Piskarskas, A. Stabinis, G.P. Banfi, P. Di Trapani, and R. Righini, *Traveling-wave parametric generation of widely tunable, highly coherent femtosecond light pulses,* J. Opt. Soc. Am. B **10** (11) 2222-2232 (1993).

[40] Kuo, P.S., K.L. Vodopyanov, M.M. Fejer, D.M. Simanovskii, X. Yu, J.S. Harris, D. Bliss, and D. Weyburne, *Optical parametric generation of a mid-infrared continuum in orientation-patterned GaAs,* Opt. Lett. **31** (1) 71-73 (2006).

[41] Tiihonen, M., V. Pasiskevicius, A. Fragemann, C. Canalias, and F. Laurell, *Ultrabroad gain in an optical parametric generator with periodically poled $KTiOPO_4$,* Applied Physics B: Lasers and Optics **85** (1) 73-77 (2006).

[42] Gaydardzhiev, A., I. Nikolov, I. Buchvarov, V. Petrov, and F. Noack, *Ultrabroadband operation of a femtosecond optical parametric generator based on BiB_3O_6 in the near-IR,* Opt. Express **16** (4) 2363-2373 (2008).

[43] Prakash, O., H.H. Lim, B.J. Kim, K. Pandiyan, M. Cha, and B. Rhee, *Collinear broadband optical parametric generation in periodically poled lithium niobate crystals by group velocity matching,* Applied Physics B: Lasers and Optics **92** (4) 535-541 (2008).

[44] Charbonneau-Lefort, M., M.M. Fejer, and B. Afeyan, *Tandem chirped quasi-phase-matching grating optical parametric amplifier design for simultaneous group delay and gain control,* Opt. Lett. **30** (6) 634-636 (2005).

[45] Charbonneau-Lefort, M., B. Afeyan, and M.M. Fejer, *Optical parametric amplifiers using chirped quasi-phase-matching gratings I: practical design formulas,* J. Opt. Soc. Am. B **25** (4) 463-480 (2008).

[46] Charbonneau-Lefort, M., B. Afeyan, and M.M. Fejer, *Optical parametric amplifiers using nonuniform quasi-phase-matched gratings. II. Space-time evolution of light pulses,* J. Opt. Soc. Am. B **25** (4) 683-700 (2008).

[47] Ostrovskii, L.A., *Self-action of light in crystals,* JETP Lett. **5** 272-5 (1967).

[48] Belashenkov, N.R., S.V. Gagarskii, and M.V. Inochkin, *Nonlinear refraction of light on second-harmonic generation,* Opt. Spectrosc. **66** 806-8 (1989).

[49] DeSalvo, R., D.J. Hagan, M. Sheik-Bahae, G. Stegeman, E.W. Van Stryland, and H. Vanherzeele, *Self-focusing and self-defocusing by cascaded second-order effects in KTP,* Opt. Lett. **17** (1) 28-30 (1992).

[50] Belostotsky, A.L., A.S. Leonov, and A.V. Meleshko, *Nonlinear phase change in type II second-harmonic generation under exact phase-matched conditions,* Opt. Lett. **19** (12) 856-858 (1994).

[51] Stegeman, G.I., *$\chi^{(2)}$ cascading: nonlinear phase shifts,* Quantum and Semiclassical Optics: Journal of the European Optical Society Part B **9** (2) 139 (1997).

[52] Gordon, L., G.L. Woods, R.C. Eckardt, R.R. Route, R.S. Feigelson, M.M. Fejer, and R. Byer, *Diffusion-bonded stacked GaAs for quasiphase-matched second-harmonic generation of a carbon dioxide laser,* Electronics Letters **29** (22) 1942-1944 (1993).

[53] Lallier, E., M. Brevignon, and J. Lehoux, *Efficient second-harmonic generation of a CO2 laser with a quasi-phase-matched GaAs crystal,* Opt. Lett. **23** (19) 1511-1513 (1998).

[54] Feng, D., N.-B. Ming, J.-F. Hong, Y.-S. Yang, J.-S. Zhu, Z. Yang, and Y.-N. Wang, *Enhancement of second-harmonic generation in $LiNbO_3$ crystals with periodic laminar ferroelectric domains,* Applied Physics Letters **37** (7) 607-609 (1980).

[55] Ebert, C.B., L.A. Eyres, M.M. Fejer, and J.S. Harris Jr, *MBE growth of antiphase GaAs films using GaAs/Ge/GaAs heteroepitaxy,* Journal of Crystal Growth **201–202** (0) 187-193 (1999).

[56] Koh, S., T. Kondo, M. Ebihara, T. Ishiwada, H. Sawada, H. Ichinose, I. Shoji, and R. Ito, *GaAs/Ge/GaAs Sublattice Reversal Epitaxy on GaAs (100) and (111) Substrates for Nonlinear Optical Devices,* Japanese Journal of Applied Physics **38** (2) L508-L511 (1999).

[57] Webjorn, J., V. Pruneri, P.S.J. Russell, J.R.M. Barr, and D.C. Hanna, *Quasi-phase-matched blue light generation in bulk lithium niobate, electrically poled via periodic liquid electrodes,* Electronics Letters **30** (11) 894-895 (1994).

[58] Burns, W.K., W. McElhanon, and L. Goldberg, *Second harmonic generation in field poled, quasi-phase-matched, bulk $LiNbO_3$,* Photonics Technology Letters, IEEE **6** (2) 252-254 (1994).

[59] Fejer, M.M., G.A. Magel, D.H. Jundt, and R.L. Byer, *Quasi-phase-matched second harmonic generation: tuning and tolerances,* Quantum Electronics, IEEE Journal of **28** (11) 2631-2654 (1992).

[60] Gallo, K., C. Codemard, C.B. Gawith, J. Nilsson, P.G.R. Smith, N.G.R. Broderick, and D.J. Richardson, *Guided-wave second-harmonic generation in a $LiNbO_3$ nonlinear photonic crystal,* Opt. Lett. **31** (9) 1232-1234 (2006).

[61] Imeshev, G., M. Proctor, and M.M. Fejer, *Lateral patterning of nonlinear frequency conversion with transversely varying quasi-phase-matching gratings,* Opt. Lett. **23** (9) 673-675 (1998).

[62] Saltiel, S., W. Krolikowski, D. Neshev, and Y.S. Kivshar, *Generation of Bessel beams by parametric frequency doubling in annular nonlinear periodic structures,* Optics Express **15** (7) 4132-4138 (2007).

[63] Peng, L.-H., C.-C. Hsu, and A.H. Kung, *Broad multiwavelength second-harmonic generation from two-dimensional $\chi^{(2)}$ nonlinear photonic crystals of tetragonal lattice structure,* IEEE Journal of Selected Topics in Quantum Electronics **10** (5) 1142-1148 (2004).

[64] Arie, A., N. Habshoosh, and A. Bahabad, *Quasi phase matching in two-dimensional nonlinear photonic crystals,* Optical and Quantum Electronics **39** (4-6) 361-375 (2007).

[65] Giacovazzo, C., H.L. Monaco, G. Artioli, D. Viterbo, G. Ferraris, G. Gilli, G. Zanotti, and M. Catti, *Fundamentals of crystallography*, ed. C. Giacovazzo. Oxford: University Press (2002).

[66] Arie, A., A. Bahabad, and N. Habshoosh, *Nonlinear Interactions in Periodic and Quasi-Periodic Nonlinear Photonic Crystals*, in *Ferroelectric Crystals for Photonic Applications*, P. Ferraro, S. Grilli, and P. Natale, editors. Springer Berlin Heidelberg. 259-284 (2009).

[67] Zukauskas, A., N. Thilmann, V. Pasiskevicius, F. Laurell, and C. Canalias, *5 mm thick periodically poled Rb-doped KTP for high energy optical parametric frequency conversion,* Opt. Mater. Express **1** (2) 201-206 (2011).

[68] Ishizuki, H. and T. Taira, *Half-joule output optical-parametric oscillation by using 10-mm-thick periodically poled Mg-doped congruent $LiNbO_3$,* Opt. Express **20** (18) 20002-20010 (2012).

[69] Shur, V.Y., *Correlated nucleation and self-organized kinetics of ferroelectric domains*, in *Nucleation Theory and Applications*, J.W.P. Schmelzer, editor. Wiley-VCH: Weinheim. 178-214 (2005).

[70] Ashkin, A., G.D. Boyd, J.M. Dziedzic, R.G. Smith, A.A. Ballman, J.J. Levinstein, and K. Nassau, *Optically-induced refractive index inhomogeneities in $LiNbO_3$ and $LiTaO_3$,* Applied Physics Letters **9** (1) 72-74 (1966).

[71] Furukawa, Y., K. Kitamura, A. Alexandrovski, R.K. Route, M.M. Fejer, and G. Foulon, *Green-induced infrared absorption in MgO doped $LiNbO_3$,* Applied Physics Letters **78** (14) 1970-1972 (2001).

[72] Hirohashi, J., V. Pasiskevicius, S. Wang, and F. Laurell, *Picosecond blue-light-induced infrared absorption in single-domain and periodically poled ferroelectrics,* Journal of Applied Physics **101** (3) 033105 (2007).

[73] Tovstonog, S.V., S. Kurimura, and K. Kitamura, *High power continuous-wave green light generation by quasiphase matching in Mg stoichiometric lithium tantalate,* Applied Physics Letters **90** (5) 051115-3 (2007).

[74] Yu, N.E., S. Kurimura, Y. Nomura, M. Nakamura, K. Kitamura, Y. Takada, J. Sakuma, and T. Sumiyoshi, *Efficient optical parametric oscillation based on periodically poled 1.0 mol % MgO-doped stoichiometric $LiTaO_3$,* Applied Physics Letters **85** (22) 5134-5136 (2004).

[75] Shoji, I., T. Kondo, A. Kitamoto, M. Shirane, and R. Ito, *Absolute scale of second-order nonlinear-optical coefficients,* J. Opt. Soc. Am. B **14** (9) 2268-2294 (1997).

[76] Yu, N.E., S. Kurimura, Y. Nomura, and K. Kitamura, *Stable High-Power Green Light Generation with Thermally Conductive Periodically Poled Stoichiometric Lithium Tantalate,* Jpn. J. Appl. Phys. **43** (10A) L1265-L1267 (2004).

[77] Schunemann, P.G., *Crystal Growth and Properties of Nonlinear Optical Materials,* AIP Conference Proceedings **916** (1) 541-559 (2007).

[78] Gopalan, V., N.A. Sanford, J.A. Aust, K. Kitamura, and Y. Furukawa, *Chapter 2 - Crystal growth, characterization, and domain studies in lithium niobate and lithium tantalate ferroelectrics*, in *Handbook of Advanced Electronic and Photonic Materials and Devices - Volume 4: Ferroelectrics and Dielectrics*, N. Hari Singh, M.Sc, and M.S.P.D. Ph.D.A2 - Hari Singh Nalwa, editors. Academic Press: Burlington. 62 (2001).

[79] Ishizuki, H. and T. Taira, *Mg-doped congruent $LiTaO_3$ crystal for large-aperture quasi-phase matching device,* Opt. Express **16** (21) 16963-16970 (2008).

[80] Zewail, A.H., *Femtochemistry: Atomic-Scale Dynamics of the Chemical Bond†,* The Journal of Physical Chemistry A **104** (24) 5660-5694 (2000).

[81] Goulielmakis, E., M. Schultze, M. Hofstetter, V.S. Yakovlev, J. Gagnon, M. Uiberacker, A.L. Aquila, E.M. Gullikson, D.T. Attwood, R. Kienberger, F.

Krausz, and U. Kleineberg, *Single-Cycle Nonlinear Optics,* Science **320** (5883) 1614-1617 (2008).

[82] Fuji, T., N. Ishii, T. Metzger, C.Y. Teisset, L. Turi, A. Baltuška, N. Forget, D. Kaplan, A. Galvanauskas, and F. Krausz, *Infrared Optical Parametric Chirped Pulse Amplifier for High Harmonic Generation*, in *Ultrafast Optics V*, S. Watanabe and K. Midorikawa, editors. Springer New York. 513-519 (2007).

[83] Cirmi, G., C.-J. Lai, E. Granados, S.-W. Huang, A. Sell, K.-H. Hong, J. Moses, P. Keathley, and F.X. Kärtner, *Cut-off scaling of high-harmonic generation driven by a femtosecond visible optical parametric amplifier,* Journal of Physics B: Atomic, Molecular and Optical Physics **45** (20) 205601 (2012).

[84] Liu, X., D. Du, and G. Mourou, *Laser ablation and micromachining with ultrashort laser pulses,* Quantum Electronics, IEEE Journal of **33** (10) 1706-1716 (1997).

[85] Shirk, M.D. and P.A. Molian, *A review of ultrashort pulsed laser ablation of materials,* Journal of Laser Applications **10** (1) 18-28 (1998).

[86] Butkus, R., R. Danielius, A. Dubietis, A. Piskarskas, and A. Stabinis, *Progress in chirped pulse optical parametric amplifiers,* Applied Physics B: Lasers and Optics **79** (6) 693-700 (2004).

[87] Sorokin, E., S. Naumov, and I.T. Sorokina, *Ultrabroadband infrared solid-state lasers,* Selected Topics in Quantum Electronics, IEEE Journal of **11** (3) 690-712 (2005).

[88] Sorokina, I.T., *Broadband Mid-Infrared Solid-State Lasers*, in *Mid-Infrared Coherent Sources and Applications*, M. Ebrahim-Zadeh and I.T. Sorokina, editors. Springer Netherlands. 225-260 (2008).

[89] Dudley, J.M., G. Genty, and S. Coen, *Supercontinuum generation in photonic crystal fiber,* Reviews of Modern Physics **78** (4) 1135 (2006).

[90] Cerullo, G., M. Nisoli, S. Stagira, and S. De Silvestri, *Sub-8-fs pulses from an ultrabroadband optical parametric amplifier in the visible,* Opt. Lett. **23** (16) 1283-1285 (1998).

[91] Eckardt, R. and J. Reintjes, *Phase matching limitations of high efficiency second harmonic generation,* Quantum Electronics, IEEE Journal of **20** (10) 1178-1187 (1984).

[92] Conforti, M., F. Baronio, and C. De Angelis, *Nonlinear envelope equation for broadband optical pulses in quadratic media,* Physical Review A **81** (5) 053841 (2010).

[93] Brabec, T. and F. Krausz, *Nonlinear Optical Pulse Propagation in the Single-Cycle Regime,* Physical Review Letters **78** (17) 3282-3285 (1997).

[94] Tiihonen, M. and V. Pasiskevicius, *Two-dimensional quasi-phase-matched multiple-cascaded four-wave mixing in periodically poled $KTiOPO_4$,* Opt. Lett. **31** (22) 3324-3326 (2006).

[95] Xu, P., J.F. Wang, C. Li, Z.D. Xie, X.J. Lv, H.Y. Leng, J.S. Zhao, and S.N. Zhu, *Simultaneous optical parametric oscillation andintracavity second-harmonic generation basedon a hexagonally poled lithium tantalate,* Opt. Express **17** (6) 4289-4294 (2009).

[96] Marcus, G., A. Zigler, D. Eger, A. Bruner, and A. Englander, *Generation of a high-energy ultrawideband chirped source in periodically poled $LiTaO_3$,* J. Opt. Soc. Am. B **22** (3) 620-622 (2005).

[97] Lai, C.-J., L.H. Peng, and A.H. Kung, *Optical interference in nonlinear photonic crystals,* Optics Letters **32** (21) 3200-3202 (2007).

[98] Liu, H.-C. and A.H. Kung, *Substantial gain enhancement for optical parametric amplification and oscillation in two-dimensional $\chi^{(2)}$ nonlinear photonic crystals,* Opt. Express **16** (13) 9714-9725 (2008).

[99] de Sterke, M., S.M. Saltiel, and Y.S. Kivshar, *Efficient collinear fourth-harmonic generation by two-channel multistep cascading in a single two-dimensional nonlinear photonic crystal,* Optics Letters **26** (8) 539-541 (2001).

[100] Reed, M.K., M.K. Steiner-Shepard, and D.K. Negus, *Widely tunable femtosecond optical parametric amplifier at 250 kHz with a Ti:sapphire regenerative amplifier,* Opt. Lett. **19** (22) 1855-1857 (1994).

[101] Payne, S.A., L.L. Chase, L.K. Smith, W.L. Kway, and H.W. Newkirk, *Laser performance of $LiSrAlF_6:Cr^{3+}$,* Journal of Applied Physics **66** (3) 1051-1056 (1989).

[102] Heese, C., C.R. Phillips, L. Gallmann, M.M. Fejer, and U. Keller, *Ultrabroadband, highly flexible amplifier for ultrashort midinfrared laser pulses based on aperiodically poled $Mg:LiNbO_3$,* Opt. Lett. **35** (14) 2340-2342 (2010).

[103] Saltiel, S.M. and Y.S. Kivshar, *All-optical deflection and splitting by second-order cascading,* Opt. Lett. **27** (11) 921-923 (2002).

[104] Ellenbogen, T., A. Ganany-Padowicz, and A. Arie, *Nonlinear photonic structures for all-optical deflection,* Optics Express **16** (5) 3077-3082 (2008).

[105] Chowdhury, A., S.C. Hagness, and L. McCaughan, *Simultaneous optical wavelength interchange with a two-dimensional second-order nonlinear photonic crystal,* Opt. Lett. **25** (11) 832-834 (2000).

[106] Gong, Y.X., P. Xu, J. Shi, L. Chen, X.Q. Yu, P. Xue, and S.N. Zhu, *Generation of polarization-entangled photon pairs via concurrent spontaneous parametric downconversions in a single $\chi^{(2)}$ nonlinear photonic crystal,* Opt. Lett. **37** (21) 4374-4376 (2012).

[107] Megidish, E., A. Halevy, H.S. Eisenberg, A. Ganany-Padowicz, N. Habshoosh, and A. Arie, *Compact 2D nonlinear photonic crystal source of beamlike path entangled photons,* Opt. Express **21** (6) 6689-6696 (2013).

[108] Jin, H., P. Xu, X.W. Luo, H.Y. Leng, Y.X. Gong, W.J. Yu, M.L. Zhong, G. Zhao, and S.N. Zhu, *Compact Engineering of Path-Entangled Sources from a Monolithic Quadratic Nonlinear Photonic Crystal,* Physical Review Letters **111** (2) 023603 (2013).

[109] Chang, W.K., Y.H. Chen, H.H. Chang, J.W. Chang, C.Y. Chen, Y.Y. Lin, Y.C. Huang, and S.T. Lin, *Two-dimensional PPLN for simultaneous laser Q-switching and optical parametric oscillation in a $Nd:YVO_4$ laser,* Opt. Express **19** (24) 23643-23651 (2011).

[110] Chen, Y.H., W.K. Chang, N. Hsu, C.Y. Chen, and J.W. Chang, *Internal Q-switching and self-optical parametric oscillation in a two-dimensional periodically poled Nd:MgO:$LiNbO_3$ laser,* Optics Letters **37** (14) 2814-2816 (2012).

[111] Lazoul, M., A. Boudrioua, L.M. Simohamed, A. Fischer, and L.-H. Peng, *Experimental study of multiwavelength parametric generation in a two-dimensional periodically poled lithium tantalate crystal,* Optics Letters **38** (19) 3892-3894 (2013).

[112] Pe'er, A., Y. Bromberg, B. Dayan, Y. Silberberg, and A.A. Friesem, *Broadband sum-frequency generation as an efficient two-photon detector for optical tomography,* Optics Express **15** (14) 8760-8769 (2007).